University of Huddersfield Repository

Giusca, Claudiu Laurentiu

Development of a traceability route for areal surface texture measurements

Original Citation

Giusca, Claudiu Laurentiu (2014) Development of a traceability route for areal surface texture measurements. Doctoral thesis, University of Huddersfield.

This version is available at http://eprints.hud.ac.uk/23390/

University of
HUDDERSFIELD
Inspiring tomorrow's professionals

Development of a traceability route for areal surface texture measurements

Claudiu L Giusca

A thesis submitted to the University of Huddersfield
in partial fulfilment of the requirements for
the degree of Doctor of Philosophy

The University of Huddersfield in collaboration with the
National Physical Laboratory

March 2014

Abstract

Modern manufacturing industry is beginning to benefit from the ability to control the three dimensional, or areal, structure of a surface. To underpin areal surface manufacturing, a traceable measurement infrastructure is necessary. In this thesis a practical realisation of areal surface traceability is presented, which includes the development of: a primary instrument, methodologies for using the primary instrument to calibrate material measurement standards used as standard transfer artefacts, and the process of transferring this traceability to industrial users of stylus and optical instruments.

The design of the primary instrument and its complex measurement uncertainty model are described, including detailed analysis of the input parameters of the uncertainty model and their effect on the co-ordinate measurements of the instrument.

The development of the process of transferring the areal traceability to industrial users lead to a set of metrological characteristics applicable to all areal surface topography measuring instruments. The set of metrological characteristics, now included into international standards, comprise of: measurement noise, flatness deviation, amplification, linearity and squareness, and resolution. Despite the differences in operation of the various types of instrument, the idea behind this set of metrological characteristics is based on the fact that these instruments produce three dimensional data sets of points, which is a new approach in the field. Metrological characteristics are quantities that can be measured directly, generally using calibrated material measures. The development of standard methodologies for calibrating the metrological characteristics, and the explicit relationship between the metrological characteristics and the measurement uncertainty associated with the co-ordinate measurements provided by the instrument is presented. Many of the techniques described in this thesis are now being discussed for inclusion into international standards.

Acknowledgements

First and foremost I would like to thank my supervisors, Professor Xiang Jiang (University of Huddersfield) and Professor Richard K Leach (National Physical Laboratory) for their continuing support and guidance throughout the course of my PhD.

All the collaborators are gratefully acknowledged for the support they have generously provided in manufacturing material measures and loaning of instruments. In no particular order: Dr Markus Fabrich and Dr Akihiro Fujii (Olympus), Prof Kazuhisa Yanagi (Nagaoka University of Technology), Dr Kai Rickens and Dr Oltmann Riemer (University of Bremen), Dr Markus Guttmann and Dr Peter-Jürgen Jakobs (Karlsruhe Institute of Technology), Mr Paul Rubert (Rubert & Co) and Dr David Cox (University of Surrey).

I am extremely grateful to NPL internal collaborators: Professor Alistair Forbes for his help in developing computational models for various aspects concerning the NPL Areal Instrument, Mr David Flack and Dr Peter Harris for their useful comments regarding the review of several documents that were generated during this study and Dr Christopher Jones for maintaining the driving software of the NPL Areal Instrument.

I am grateful to the ISO/TC213 Working Group 16 –Optical Group led by Dr Ted Vorburger (NIST) for the useful discussions that helped in developing the consistent framework around the metrological characteristics.

I must thank a number of individuals who once worked with me at NPL as part of internship or secondment schemes, starting with Dr Kazuia Naoi (NMIJ), Mr Frank Helery (ENSAME France), Mr Tadas Gutauskas (Imperial College London), Mr Abishek Raj (India), Mr Baptiste Blanchon (ENSAM, France), Dr Yushu Shi (NIM).

The work was funded by the UK NMO Engineering & Flow Metrology Programme.

This thesis is dedicated to my loving wife and dear son.

Declaration

The majority of the work presented in this thesis is the work of the author alone. The contributions of others to the reported work are noted below.

This thesis concerns critical contributions for the continuing long-term development of a traceability route for areal surface topography measurements in the UK. As such, it inevitably both builds on the earlier contributions of several colleagues and benefits from their present work in related areas. The thesis presented is the work solely of the author except where explicitly stated otherwise and cited in the main text.

Contributions of others are as follows:

The computational model presented in chapter 2 for various aspects concerning the NPL Areal Instrument was developed with Professor Alistair Forbes (Giusca et al. 2011b).

Detailed testing was undertaken by a number of individuals who are currently employed at NPL or once worked at NPL as part of internship or secondment schemes, as well as MSc students under the direct supervision of the author. Specifically, Dr Kazuia Naoi (Leach et al. 2009) contributed to chapter 2; Frank Helery and Tadas Gutauskas (Giusca et al. 2012a,b) contributed to chapters 5 and 6; Lakshmi Nimishakavi (Giusca et al. 2012b) contributed to chapter 5.

List of common acronyms and notations

S-filter – surface filters which remove small scale lateral components

L-filter – surface filters which remove large scale lateral components

F-operator – operators which removes form

$\alpha x, \alpha y, \alpha z$ – amplification coefficient of the instrument scales

lx, ly, lz – linearity of the instrument scales

FLT-Z – flatness deviation

Nm – measurement noise

Dlim – lateral period limit

PER – perpendicularity of the axis

u – combined standard uncertainty

CSI – coherence scanning interferometer

ICM – imaging confocal microscope

Sq – root mean square (RMS) value of the scale limited surface,

Sz – maximum height of the scale limited surface,

u_{NF} – measurement noise and flatness deviation on the z axis measurement standard uncertainty

$u_{T\text{-}x}$, $u_{T\text{-}y}$ $u_{T\text{-}z}$ – combined effect of the measurement errors, traceability, repeatability and/or reproducibility on the co-ordinate measurement standard uncertainty

u_{Res} – lateral resolution contribution to the measurement uncertainty,

Table of content

List of tables

List of figures

1 Introduction

Over the past three decades there has been an increased need to relate surface texture to surface function, which allows the manufacturer to predict how a surface interacts with its surroundings. With such knowledge, optical, tribological, biological, fluidic and many other properties can be altered (Evans and Bryan 1999, Bruzzone *et al.* 2008). To control the manufacture of such products, traditional single line profile measurements are inadequate and an areal characterisation of surface texture is essential (Jiang *et al.* 2007b). A single line profile measurement gives rise to enough information to control production, but is often limited to looking for process change. Areal measurements offer more statistical significance and a better visual representation of the overall structure of the surface, thus providing a more realistic representation of the whole surface (Blunt and Jiang 2003).

1.1 Historical overview

Broadly speaking, the development of surface texture characterisation followed two strands: development of instrumentation (see chapter 4) and development of analysis tools, both of which evolved at the same time. The first analysis tool was the Abbot-Firestone curve (Abbott and Firestone 1933) and soon after that several researchers made the field of surface texture the formal discipline that it is today (Jiang *et al.* 2007a and references there-in, Schlesinger 1942, Reason *et al.* 1944, Perthen 1949, Page 1948, Schorsch 1958). Three main surface components were identified: form, waviness and roughness (see figure 1.1). It was found that the most difficult task was to separate waviness from roughness. To solve the latter issue, two methods were proposed: one designed around a mean line system, or M-system (Reason 1961), and one based on an envelope system, or E-system (von Weingraber 1956). Neither of the two systems was practical until the electrical filtering theory (Whitehouse and Reason 1963) and, subsequently, the theory behind phase correct filters (Whitehouse 1967/1968) allowed the M-system to prevail.

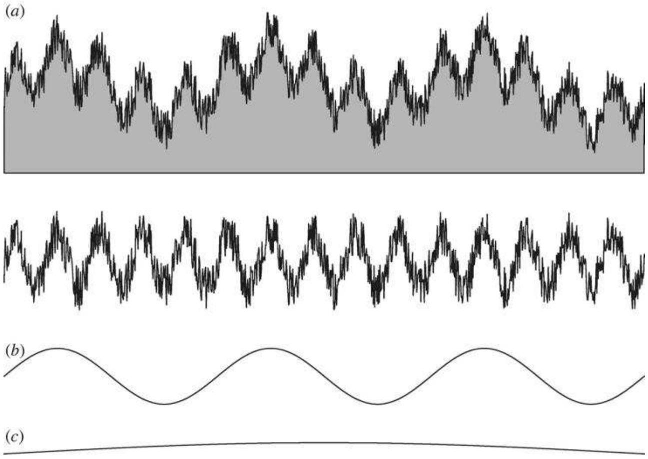

Figure 1.1 Geometric components of a surface profile: (a) roughness, (b) waviness, and (c) form (Jiang *et al.* 2007)

Today, the profile standard filters are designed with an arbitrary spatial frequency cut-off which gives 50 % amplitude transmission (see figure 1.2 where λs – is the filter cut-off which defines the intersection between the roughness and the even shorter wave components present in the surface, λc – defines the intersection between the roughness and waviness and λf – between waviness and even longer wave components) making the roughness and waviness cut-off symmetrical and complementary (Jiang *et al.* 2007a).

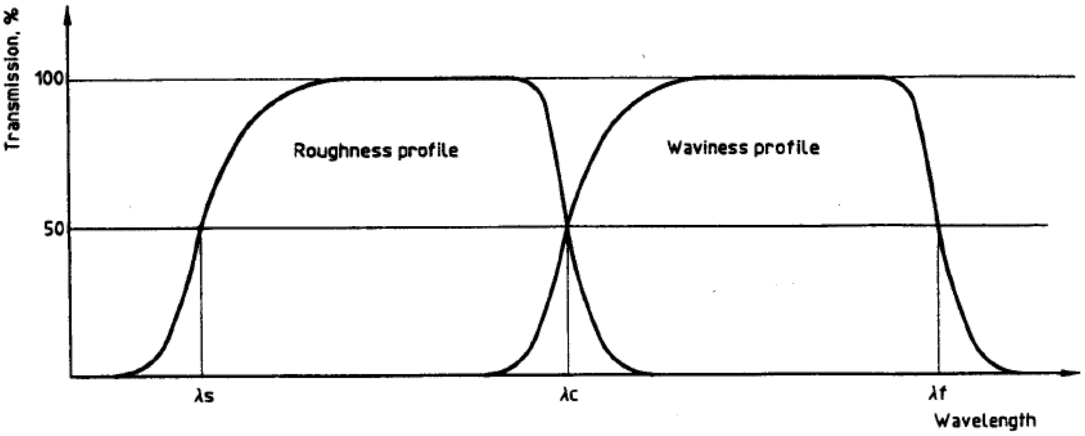

Figure 1.2 Transmission characteristics of roughness and waviness profiles (ISO 4287: 1997)

The digital era had a major impact, especially in the proliferation of the profile parameters that were used to assess surfaces quantitatively (Whitehouse 1982). For the first time, computers also allowed surface visualisation to be at the fingertip of the operator. Advances made in digital filtration (in addition to increased z range and calibration procedures for stylus instruments) meant that the same instrument could measure profile, waviness and form. Surface texture measuring instrumentation took full advantage of the analogue to digital transformation and became more versatile.

As in the profile case, the development of areal surface texture characterisation followed closely the advances made in areal instrumentation, which is presented in more detail in chapter 4. Initial research (see for example Nayak (1971) and Sayles and Thomas (1977), Whitehouse and Philips (1982) and Whitehouse (1994)) highlighted the problems linked to specification and characterisation of areal features, and the effect of the measurement conditions on areal parameters (Jiang *et al.* 2007b). A coherent framework that allowed the establishment of areal surface texture characterisation was supported by the European Community in the 1990s, which funded two major projects. The first project enabled an integrated method for the measurement and characterisation of engineered surfaces (Stout *et al.* 1993), developing the first coherent set of areal parameters also known as 'Birmingham 14' (Dong *et al.* 1994a, b). The second project, called 'SurfStand' (Blunt and Jiang 2003), was aimed towards the standardisation framework for three dimensional (3D) or 'areal' surface roughness, leading to the set-up of a working group (WG16) in ISO/TC 213 in 2002. Current standardisation effort in the ISO/TC 213-WG16 in the field of areal surface texture measurement includes the development of a suite of documents, under the generic title of ISO 25178, which includes definitions of terms and parameters, file formats, nominal characteristics of, and calibration methods for, areal surface topography measuring instruments.

1.2 Areal measurement

There is a wide variety of areal measurement methods dedicated to surface texture measurement that could be categorised into two main classes: areal topography and area-integrating (ISO 25178–6 2010); however, only the traceability of areal topography methods is the main subject of this thesis. The difference between the two classes is that the area integrating methods produce a numerical result that depends on the area-integrating properties of the surface, while the areal topography methods produce a 3D map of the surface that can be represented mathematically as a height function $z(x, y)$ (Leach 2011). Areal topography measuring instruments are effectively co-ordinate measuring machines (CMMs) and their performance depends on a complex interaction between a number of influence factors, such as the squareness of pairs of axes, alignment and imperfect motion (Cox *et al.* 1999). Whilst the effects of these interactions are usually compensated through calibration, the assessment of measurement uncertainty remains an issue.

In reality the areal topography methods are a 2½D type of investigation, not 3D, and, as a result, undercuts and steep side walls are not measured, although some instruments can provide more information than others depending on the design of the measuring probe. The areal map contains information about surface texture but, at the same time, it carries information about the form of the component that is measured. For example, in figure 1.3 a camshaft (see figure 1.3 top left) is measured using an areal topography method. The measurement result contains both form and surface texture (see figure 1.3 top right), from which a cylinder is removed to obtain just the surface texture (see figure 1.3 bottom). Quantitative estimation of surface texture is given by the surface texture parameters (ISO 25178-2 2012), which are calculated after filtering the surface texture data appropriately (ISO 25178-3 2012).

Surface texture parameters are affected by the size of the primary extracted surface and the sampling distance (ISO 25178-2 2012), *i.e.* the spatial measurement bandwidth. Setting the measurement bandwidth is application-dependent and often requires *a priori* knowledge about the surface to be measured. There are situations in which the surface to be measured is well understood, such as with a milled or turned surface, so the measurement bandwidth can be relatively simple to set.

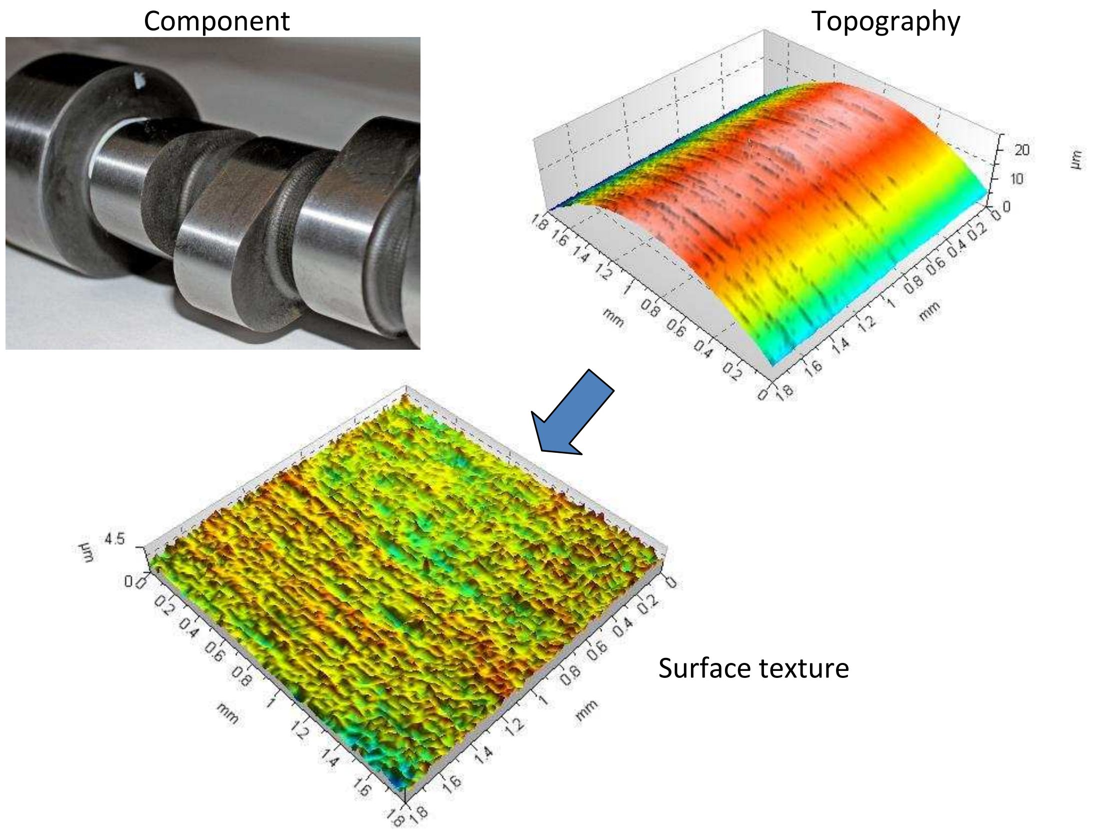

Figure 1.3 Example of surface texture measurement on a camshaft using an areal topography measuring instrument

However, there are applications in which the surface, or its functionality, is not known well. In this situation the measurement bandwidth is selected according to *a priori* theoretical knowledge about the nature of the surface, from prior experimental work, or a combination of both. Unless specified, the spatial measurement bandwidth can be established in accordance to ISO 25178-3 (2012), which recommends some basic rules on how to set the size of the primary surface and the sampling distance. These options are mainly based on the choice of S-filters (surface filters which remove small scale lateral components) and L-filters (surface filters which remove large scale lateral components)/F-operators (operators which removes form), each having a range of pre-set values, called nesting indexes, that are presented in table 1.1 (see Leach 2013, Muralikrishnan and Raja 2010 for descriptions of areal filtering).

Table 1.1 Relationships between nesting index value F-operator/L-filter, S-filter nesting index, and bandwidth ratio. *n* is a positive or negative integer

Nesting index value (F-operator/L-filter) /10^n mm	S-filter nesting index /10^n µm	Bandwidth ratio between F-operator/L-filter and S-filter nesting index
1	10	100:1
	5	200:1
	2	500:1
	1	1000:1
2	20	100:1
	10	200:1
	5	4001
	2	1000:1
2.5	25	100:1
	8	300:1
	2.5	1000:1
5	50	100:1
	20	250:1
	10	500:1
	5	1000:1
8	80	100:1
	25	300:1
	8	1000:1

The S-filter nesting index determines, or is determined, by the maximum sampling distance and the L-filter or the F-operator determines the size of primary surface (figure 1.4 presents the spatial relationship between the areal filters). The sampling distance should be chosen after the S-filter nesting index is set; however, that is not always possible because there are instruments on which the sampling distance cannot be changed. The nesting index is an extension of the cut-off wavelength from profile analysis that allows the use of the Gaussian filter and other types of filters, such as a morphological filter.

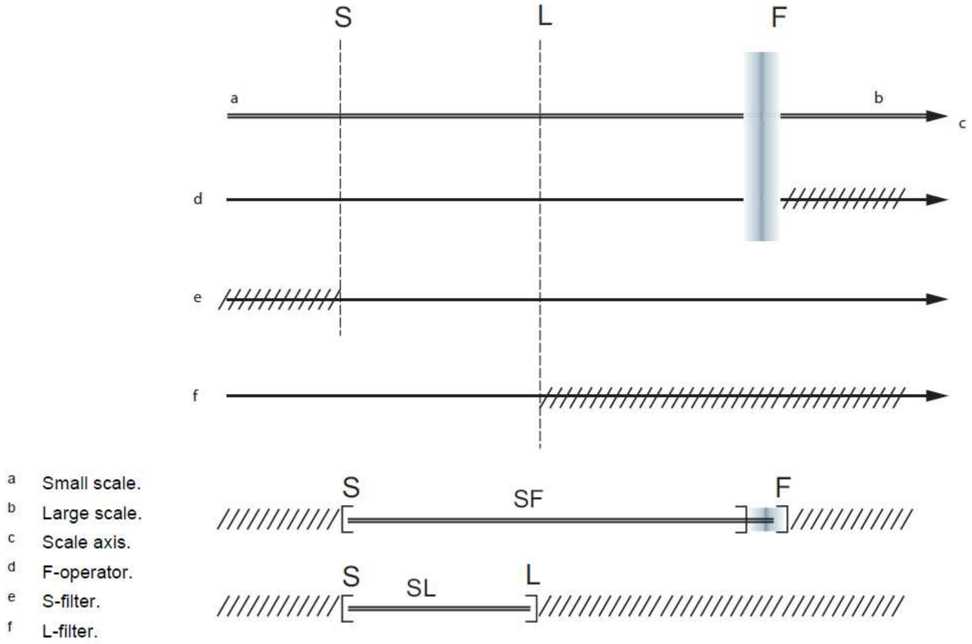

Figure 1.4 Relationships between the S-filter, L-filter, F-operator and S-F and S-L surfaces (ISO 25178:2 2012)

The S-L and S-F surfaces conceptually separate areal from profile characterisation. Unlike the profile concept (ISO 4287 1997), where the surface features, in terms of lateral scale, are separated in roughness, waviness and form having different coordinate systems (see figure 1.5) based on either lay direction (roughness) or parallel with the datum of the surface (form), areal characterisation can be integrated in a uniform coordinate system in which roughness and form are two scale components of the same surface (Jiang 2007b, ISO 25178-3 2012).

Also areal characterisation does not require a separate term for waviness but the correspondence still exists (Jiang 2007b):

- Primary profile – SF-surface (λs equivalent to S-filter and nominal form removed by F-operator);
- Roughness profile – SL-surface (λs equivalent to S-filter and λc equivalent to L-filter);

- Waviness profile - SF-surface (λc equivalent to S-filter and nominal form removed by F-operator).

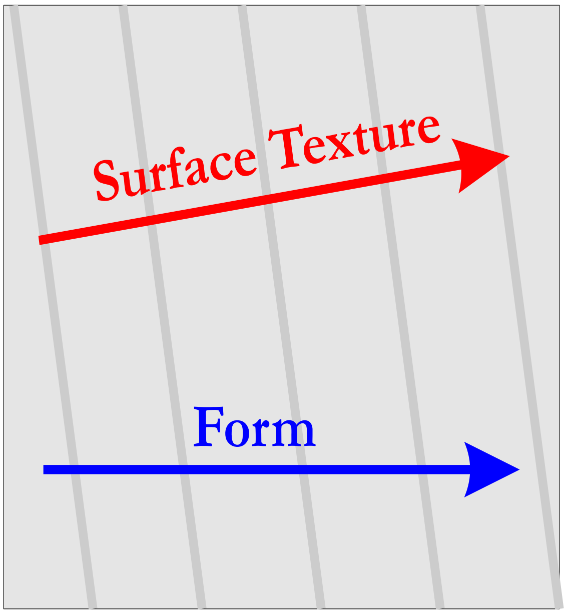

Figure 1.5 Two different coordinate systems for form and roughness

1.3 Traceability

The potential value of areal surface topography measuring instruments will only be fully realised if the instruments provide traceable measurement results, a condition currently only met in a few limited cases. By definition, traceability is *the property of a measurement result whereby the result can be related to a reference through a documented unbroken chain of calibrations, each contributing to the measurement uncertainty* (BIPM 2008c).

Areal surface topography measuring instruments require traceability to the standard of the metre that by definition is *the length of the path travelled by light in vacuum during a time interval of 1/299 792 458 of a second*, and is practically realised by an iodine-stabilised laser (Petley 1983, Felder 2005).

For example, in the case of profile traceability, the unbroken chain of calibrations includes calibration of physical measurement standards (see chapter 3) using primary surface topography measuring instruments that are equipped with laser interferometers of which the source is calibrated against an iodine-stabilised laser (Leach 2000); or interferometry (Teague 1978) and a contact stylus instrument; or an interference microscope (Brand 1995, Wilkening and Koenders 2005) and a contact stylus instrument. Figure 1.6 presents an example of a possible traceability structure for surface topography measurement.

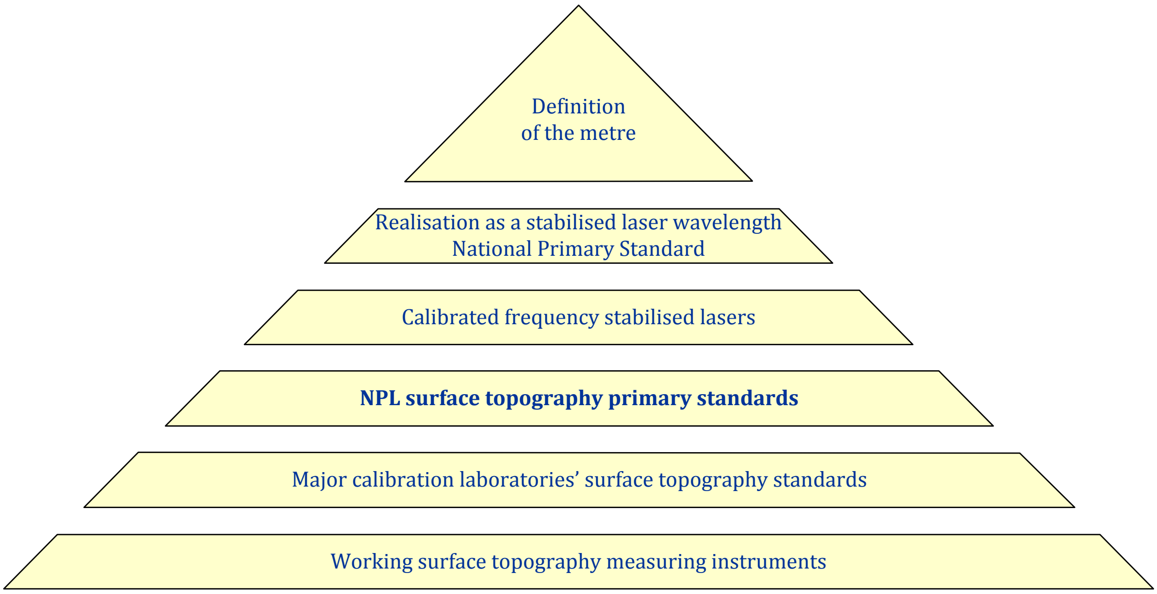

Figure 1.6 Traceability of surface topography measurements

The term calibration is often misused, which has led to confusion in understanding the meaning of the calibration process. The frequent misuse of the term calibration is when it is used instead of adjustment:

VIM 2.39 Note 1 – "Calibration should not be confused with adjustment of a measuring system, often mistakenly called "self-calibration", nor with verification of calibration."

The adjustment process physically changes some parameters of a metrological tool (it can be a mechanical adjustment or it could be the result of changing the value of a software constant) to provide an indication that is closer to a known value. The adjustment process does not provide information about the measurement uncertainty. Similar results could be obtained by correcting the measurement result using the results from a calibration certificate.

A meaningful measurement result can be presented without adjustment, but it has to have an associated uncertainty.

The definition of calibration, which is “operation that, under specified conditions, in a first step, establishes a relation between the quantity values with measurement uncertainties provided by measurement standards and corresponding indications with associated measurement uncertainties and, in a second step, uses this information to establish a relation for obtaining a measurement result from an indication”, is a two stage process (BIPM 2008c (2012)). The first stage consists of instrument calibration and the second stage involves finding the relationship between the instrument calibration results and the measurement results. The aim of the calibration process is to have a measurement result with an associated measurement uncertainty.

1.4 Areal traceability

The work in this thesis will contribute to the provision of a traceable infrastructure to allow modern manufacturing industry to be able to benefit from the ability to control surfaces in three dimensions.

The main theme of the project is the practical realisation of measurement traceability through the development of an areal primary instrument, and through surface characterisation using this instrument. This work will contribute to a more complete understanding of areal surface texture.

The project delivers methodologies for using the primary instrument to calibrate areal material measurement standards used as standard transfer artefacts. Moreover, the project establishes the process of transferring this traceability to industrial users of stylus and optical instruments according to the guidelines of the relevant ISO documents. The output of the project will improve the understanding of surface characterisation that is required by manufacturing industry when measuring areal surface texture.

Currently, areal traceability is partially inferred from the measurement of standard material measures that are generally calibrated by profile measuring instruments. Whilst profile traceability may be adequate in some circumstances, a complete traceability route for areal surface texture measurements requires the following elements:

- Material measures for calibrating areal surface texture measuring instruments.
- A primary areal surface texture measuring instrument that can measure a surface (within a pre-determined spatial bandwidth) with traceability of its axes to the definition of the metre.
- Software measurement standards for calculating areal surface texture parameters.
- Methods for calculating uncertainties associated with areal surface texture measuring instruments and surface texture parameters.
- International comparisons of areal surface texture measurements.
- Good practice guides for calibrating areal surface texture measuring instruments.

Note that not long after the development of profile reference software (Bui *et al.* 2004, Jung *et al.* 2004, Blunt *et al.* 2008), areal reference software was made available for testing the calculation algorithms of the areal surface texture parameters used in commercial applications (Harris *et al*. 2012a). Bui and Vorburger (2007) also developed independent software for the calculation of areal surface texture parameters. The results of a comparison with a few commercially available software packages were encouraging, as the majority of the software packages seem to agree, at least on amplitude parameters (Harris *et al*. 2012b).

The elements required for a complete traceability route for areal surface texture measurements and their relationships are presented in figure 1.7.

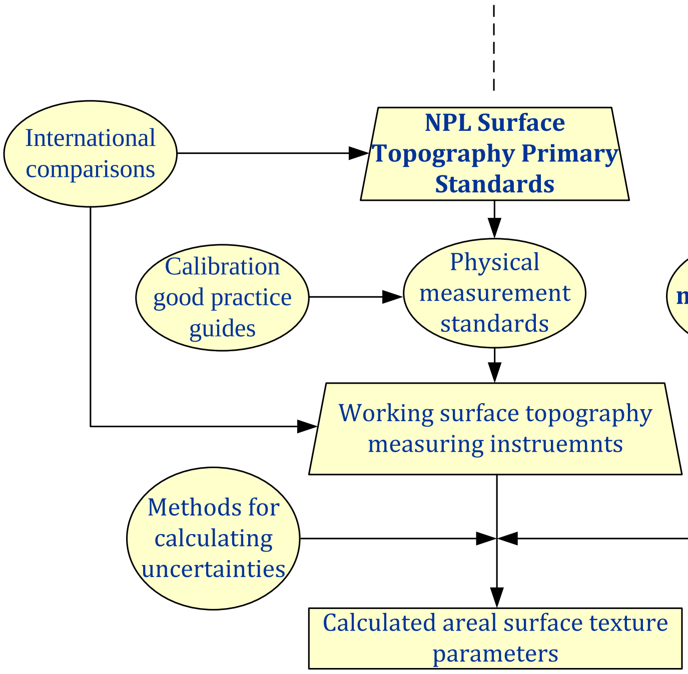

Figure 1.7 Traceability route for areal surface texture measuring instruments

1.5 Aims of the thesis

To address the first requirement in the above list, the National Physical Laboratory (NPL) has developed a primary areal surface texture measuring instrument. The NPL Areal Instrument is a contact stylus instrument that measures the motion of a stylus tip using laser interferometers. The interferometers are mounted on three mutually orthogonal axes monitoring the position of the stylus tip relative to the sample surface, providing areal measurements traceable to the definition of the metre.

i The first aim of this thesis is to demonstrate that the NPL Areal Instrument has the attributes of a traceable surface texture measuring instrument, which requires the development of a model of the measurement system that faithfully represents the behaviour of instrument.

Although the design and build of the NPL Areal Instrument were not part of this thesis, the work on the instrument characterisation and on the measurement model led to adjustments of the design of the instrument. At the start of the project, the design of the *z* metrology of the instrument employed an interferometer mounted in an arrangement that required deflections of the measurement and reference beams. Due to the design of the probe (see section 2.2) the deflection of the beams did not allow optimal strength of the optical interferometric signal. The mounting of the *z* interferometer had to be changed from the initial horizontal position to a vertical position as shown in figure 2.2. As a result, with the NPL Areal Instrument adequate measurement results were obtained. A detailed description of the instrument in the final design and its uncertainty model are presented in chapter 2.

ii The second aim of the thesis was to establish the process of transferring areal traceability to industrial users of stylus and optical instruments according to the guidelines of the relevant ISO documents. Basic instrument traceability is achieved by calibrating the axes of operation of the instrument or the instrument scales. According to ISO 25178 part 601 (2010), the instrument scales of an areal topography measuring instrument should be aligned to the axes of a right handed Cartesian co-ordinate system (note that part 601 is for stylus instruments, but the co-ordinate system will be the same for optical instruments). Practically the scales are realised by various components that are part of the metrological loop of the instrument such that the areal map of a surface is made up of a set of points measured along the three orthogonal axes.

Some of the instrument components provide a reference surface with respect to which the instrument measures surface topography and other components provide the vertical axis of the instrument. So the quality and the mutual position of these components influence the quality of areal topography measurements. Areal measurements are also affected by other factors (quantities) such as ambient temperature, mechanical and electrical noise, the quality and type of the components of the instrument, the mathematical algorithms that are used to process the height information and so on. All these factors are known as influence factors (ISO/FDIS 25178- 603 2012). Hence, to estimate the effect of the influence factors on the measurement uncertainty, a meaningful measurement model that links the influence factors to the length measurements along the instrument scales is required.

At the outset of the project it was identified that the traceability to the industrial users had to be a simple process organised as a sequence of easy to follow, and a limited number, of steps. The latter requirement was set in contrast to the development of ISO standards, which for each type of instrument list a long number of influence parameters. It is very difficult, and at the same time unnecessary, to construct a mathematical model that isolates the effect of each influence factor. The influence factors approach serves well instrument developers that are required to improve their systems, and it can be used in places such as national measurement institutes and similar organisations to build complex measurement uncertainty budgets, but it is not easy to implement on the shop floor. Hence, a major task that had to be undertaken was to convince relevant ISO committee that the benefits of the influence factor approach is only good for in depth understanding of the measuring instrumentation; however when constructing an uncertainty budget there is an easier alternative that can be used in practice.

Instead of a measurement model based on the influence factors, a simple input–output measurement model that is based on a limited number of measurable input quantities can be used. The input quantities are called metrological characteristics and they have been introduced to the ISO TC 213 WG 16. As a result, metrological characteristics are now included in ISO/CD 25178-600 (2012) and are listed in table 1.2.

Table 1.2 Metrological characteristics

Metrological characteristics	Symbol	Error along
Amplification coefficient	αx, αy, αz	x, y, z
Linearity	lx, ly, lz	x, y, z
Flatness deviation	FLT-Z	z
Measurement noise	Nm	z
Lateral period limit	Dlim	z
Perpendicularity	PER	x, y, z

The metrological characteristics incorporate the effect of the influence factors and, more importantly, they can be measured, usually with the aid of material measures.

With the metrological characteristics in place, calibration of the instrument scales consists of measuring the metrological characteristics of the instrument. Some of the metrological characteristics can be affected by the size of the primary extracted surface and the sampling distance, *i.e.* the spatial measurement bandwidth. Along with the measurement bandwidth, all other calibration conditions should be set in such a manner that all measurement conditions are replicated (as near as possible), including the environmental conditions. Sometimes, the full instrument calibration could be a very time-consuming task because it is difficult to cover all the measurement conditions in which the instrument could be used. The situation is further complicated due to the number of software settings that are available on commercial instruments. Fortunately, the often short measuring time of the optical instruments and a careful design of the experiments can partially compensate for the number of measurements required.

It is important to underline that the scope of this project was to find the simplest way to achieve traceable areal surface topography measurements, which means to establish simple procedures for testing the metrological characteristics. Hence, the method shown in this thesis of calibrating the areal instruments is not the only route to traceability, but it was found to be relatively simple to apply in practice.

1.6 Thesis layout

As mentioned in the previous section, the design and the measurement uncertainty model of the NPL Areal Instrument is described in chapter 2.

ISO/DIS 25178-70 (2012) defines several material measurement standards that can be used to calibrate areal surface texture measuring instruments. Chapter 3 reviews these material measurement standards and also presents the NPL past and present research, and development work aimed at producing a commercially-viable set of artefacts that can be used to calibrate areal surface topography measuring instruments.

Methods for calculating uncertainties associated with areal surface texture measuring instruments and surface texture parameters were developed for three instruments, a contact stylus and two optical instruments, which are described in detail in chapter 4. The calibration on the instruments in based on the measurement of their metrological characteristics: tests for measurement noise and residual flatness are presented in chapter 5; amplification, linearity and squareness of the axis are treated in chapter 6; and lateral resolution is discussed in chapter 7. Also, example methods for calculating areal texture parameters are presented in chapter 8. Chapter 9 presents the thesis conclusions and aspects of future work.

2 The NPL Areal Instrument

Profile traceability is readily available at national metrology institutes (NMIs) either in the form of a stylus instrument that has laser interferometers mounted on the axis of operation (Leach 2000) in the NPL case, as a combination of interferometry and a modified Taylor Hobson Talystep 1 at NIST-USA (Teague 1978), or a combination of interference microscopy and Taylor Hobson Nanostep 2 instrument (Garratt and Bottomley 1990) at PTB-Germany (Brand 1995). Although these instruments can achieve low measuring uncertainties, they cannot be used successfully to calibrate areal surface topography measuring instruments. Therefore, NMIs have developed primary areal surface topography measuring instruments: NPL in the form of the NPL Areal Instrument (described in this chapter - see figure 2.1, Leach 2007); the LUPO at PTB (Thomsen-Schmidt 2011, Thomsen-Schmidt and Krüger-Sehm 2008) with a working range of 50 mm × 50 mm× 100 µm and an associated measurement uncertainty of 10 nm ($k = 2$) in the z direction; and a ultra high precision coordinate measuring machine at LNE (Lahousse *et al.* 2005) with a working range of 300 mm × 300 mm × 50 µm and an associated measurement uncertainty of 2 nm in the z direction.

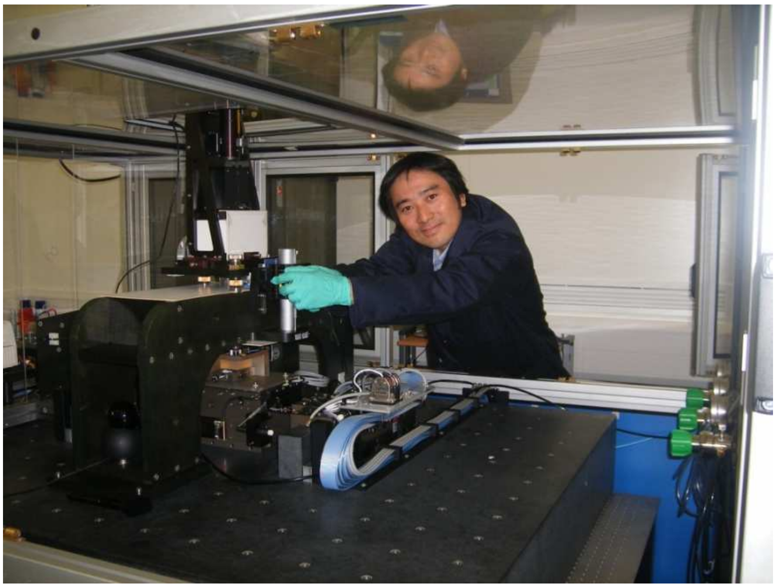

Figure 2.1 The NPL Areal Instrument

In the next section of this chapter the overall design of the NPL Areal Instrument is described. Sections 2.2 and 2.3 depict the *xy* translation stage and the probing system, respectively, followed by a detailed description of the *xy* metrology in section 2.4 and of the *z* metrology in section 2.5. The development of the measurement model is presented in section 2.6 and the uncertainty associated with the co-ordinate measurement of the instrument is calculated in section 2.7. The conclusions of this chapter are presented in section 2.8.

2.1 Overall design

The NPL Areal Instrument is designed to perform traceable 3D measurement of surface texture using a contact stylus, the position of which is monitored by laser interferometry. The instrument monitors the relative movement of a vertically mounted stylus that is in direct contact with the surface of a sample. A translation stage moves the sample in a nominally horizontal plane. As the stage moves at constant speed, three linear, and two angular laser interferometers measure the stage and stylus position in three mutually orthogonal axes. A schema of the NPL Areal Instrument is presented in figure 2.2.

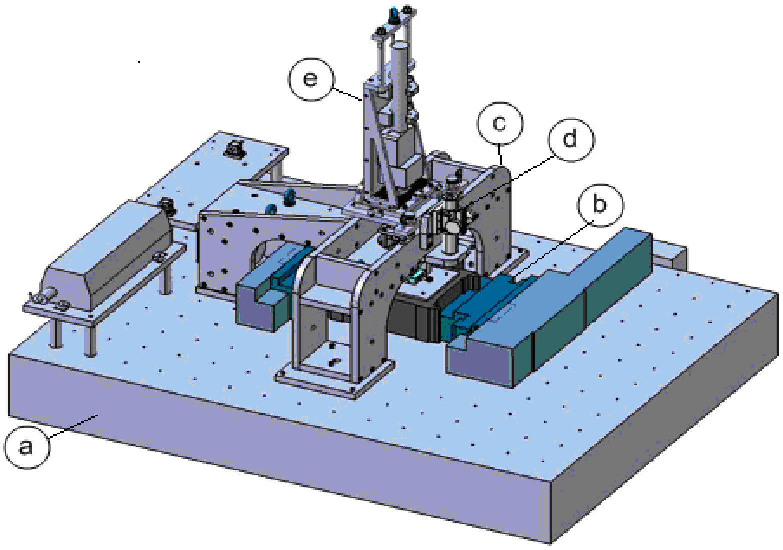

Figure 2.2 CAD model of the NPL Areal Instrument

The instrument comprises a large granite base (figure 2.2-a) that supports the structure of the instrument, a coplanar air-bearing translation stage (figure 2.2-b), a steel structural frame (figure 2.2-c), and ancillary equipment for automation and environmental monitoring. The granite base is mounted on a passive vibration isolation table, which is in turn mounted on four pneumatic legs. The structural frame is bolted onto the granite table above the coplanar translation stage that itself is rigidly attached to the granite base.

The coplanar translation stage supports a sample holder and a Zerodur mirror block in the form of a rectangular parallelepiped. The sample holder is height adjustable and is made of Zerodur spacers having different thicknesses, allowing for coarse adjustment of the sample height. The spacers are placed on an Invar height translation stage providing finer height increments. The Zerodur mirror block provides the reference surface for the z axis interferometer (see figure 2.2-e) and the measurement surfaces for the x and y axis interferometers. The mirror block thus establishes the squareness of the co-ordinate system. The Zerodur block is hollow with two sides removed (figure 2.3). The sample, height translation stage and Zerodur spacers are mounted inside the Zerodur block. The outward facing sides of the Zerodur block are polished and aluminised.

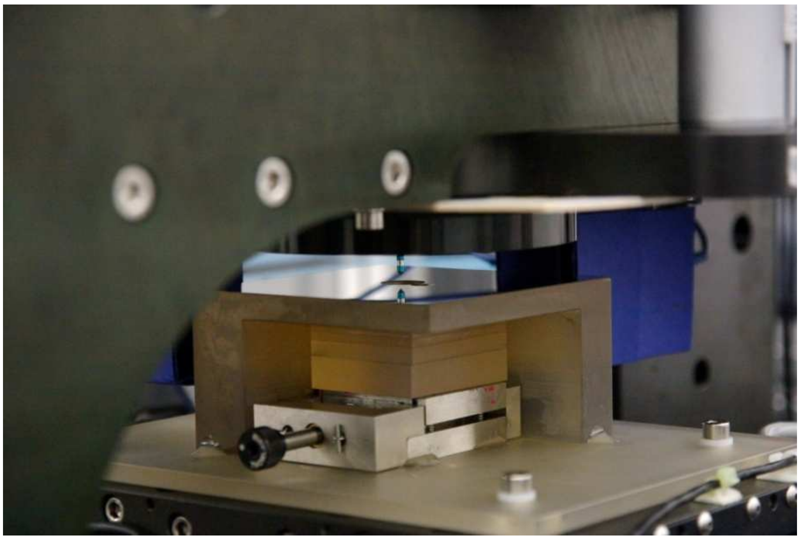

Figure 2.3 The Zerodur mirror block

The squareness of the Zerodur block was measured using a Moore 1440 precision index and a traceable autocollimator. The mirrors were measured to be at right angles to each other to within 0.2 seconds of arc. The expanded uncertainty associated with the angle measurements did not exceed 0.1 seconds of arc ($k = 2$).

The probing system (figure 2.2-d) is kinematically mounted on to the steel structural frame and can be retracted when a sample is mounted (figure 2.4).

The z axis interferometer is mounted on top of the structural frame, above the probing system, and the x and y axis interferometers (each interferometer block is column referenced, and contains a linear and an angular measuring system) are bolted on to the underside of the structural frame (figure 2.5). The z axis interferometer reference is obtained from the top of the Zerodur mirror block. Since the sample is situated below the z axis reference mirror, the probe access to the sample is through a hole in the z axis reference mirror, which limits the movement in the x and y directions to approximately 8 mm by 8 mm.

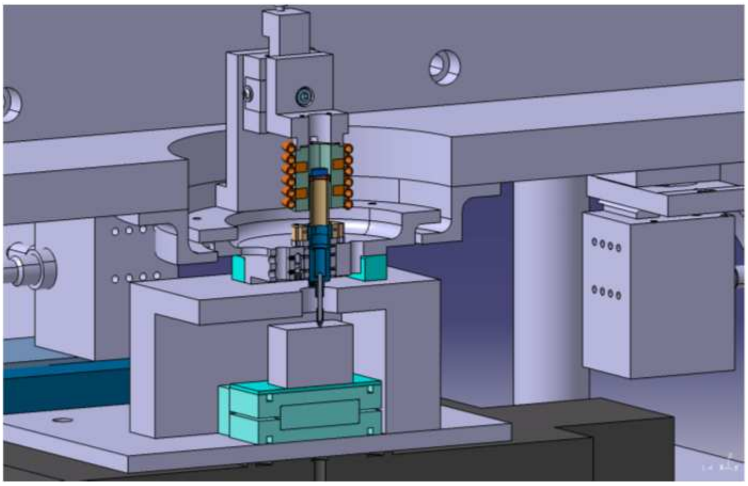

Figure 2.4 Cross-sectional representation of the probing system and its mounting

The x and y axis interferometers are referenced from two further mirrors orthogonal to each other and mounted on to the nominally stationary probing system body. Monitoring the position of the stylus tip and translation stage using laser interferometers provides the measurement traceability in each axis *via* the stabilised wavelength of the source laser.

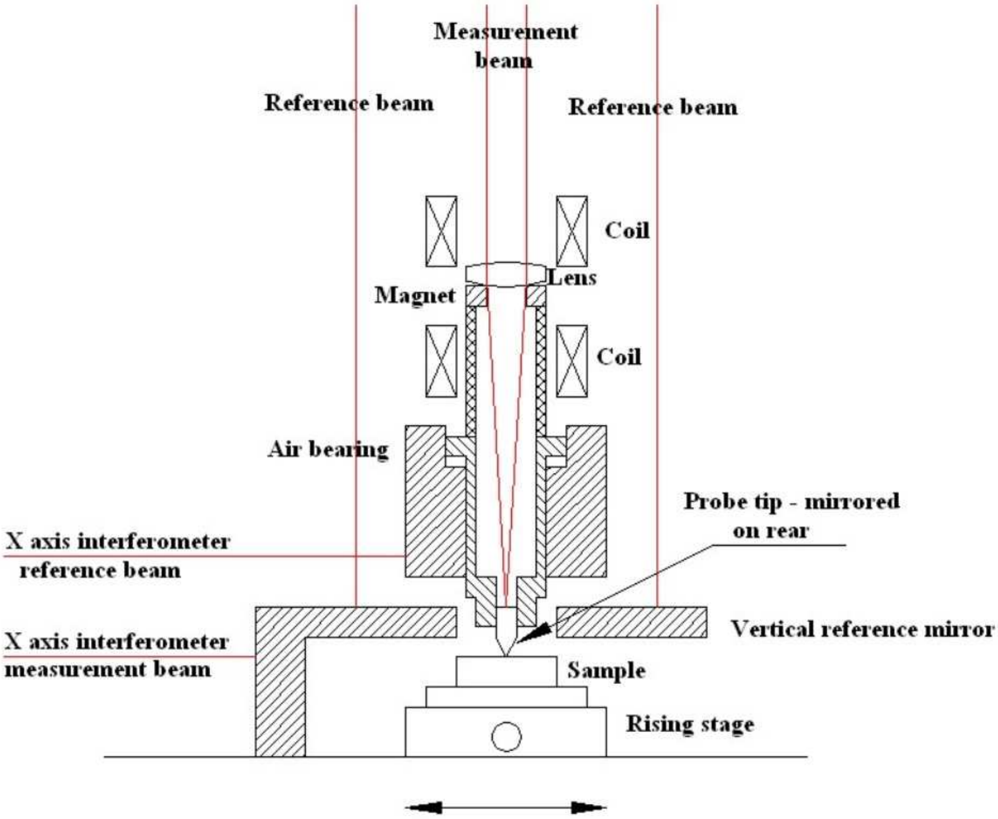

Figure 2.5 Schematic of the setup of the interferometers and sample the mount

2.2 *xy translation stage*

The coplanar air-bearing translation stage (ABL9000) was designed and manufactured for this application by Aerotech. The stage comprises two nominally orthogonal linear positioning stages. The first linear stage is aligned to travel in a horizontal plane along the system's *y* direction and the second linear stage moves in a horizontal plane along the *x* direction.

The working area of the *xy* stage is approximately 100 mm by 100 mm and the stage has speeds ranging from 0.1 mm s^{-1} up to 25 mm s^{-1}. The specified stage positioning resolution is 1 nm. The load is floated using an air supply pressure of approximately 410 kPa and the stage is vacuum preloaded. The *xy* stage is positioned by a closed-loop servo-control system that uses linear encoders.

Figure 2.6 A typical Aerotech air bearing translation stage model ABL9000

Ideally, the *xy* metrology system should record points on a perfect rectangular grid, translating one stage (say the *x* axis stage) from a start position to an end position in one continuous movement (a perfect grid simply makes the data analysis easier). The *y* axis stage is then stepped by a fixed amount and a further *x* axis scan is taken, thus building up an area map in a raster fashion. Using external interferometers for metrology, the positional repeatability is not important, but it is preferable as it reduces the number of subsequent movements to reach a desired position and permits for error compensation (Forbes and Leach 2005). The straightness, *xty* (the deviation from the true line of travel perpendicular to the direction of travel in the horizontal plane) and flatness, *xtz* (vertical straightness) were found to be better than 0.2 µm over the stage working range, which represents a tenth of a standard stylus radius of 2 µm. More importantly, the stage straightness and flatness repeatability were found to be less than 10 nm. These errors do not affect the Areal Instrument point coordinate measurement. The straightness and flatness errors generate unequal spacing between the grid's points that could create problems in the calculation of the surface texture parameters.

The errors in roll and pitch angles (rotations around the *x* and *y* axes) were found to be better than 0.2 seconds of arc over the stage working range (0.01 nm error for 8 mm of travel). Although the constraints imposed on the yaw angle were not so tight, the system does not rotate by more than 1 second of arc around its *z* axis (0.3 nm error for 8 mm of travel).

The measurement results of the straightness, flatness, roll, pitch and yaw errors of the air bearing stage provided by the stage manufacturer are presented in appendix 1.

2.3 Probing system

The instrument is required to operate over a minimum vertical range of 0.1 mm and was designed to be capable of maintaining a constant contact force (of approximately 0.1 mN – optimal for surface texture measurements employing a 2 μm stylus tip radius – see section 4.2) throughout its vertical range. The instrument uses an air-bearing slideway and a magnetic device (Bayliss *et al.* 2006) for balancing the probing system static load acting on the surface, and for applying the appropriate force to maintain permanent contact between the stylus and the surface.

The fixed part of the probing system, containing the outer cylinder of the air-bearing and the electromagnetic coils, is kinematically located on top of the metrology frame. This kinematic arrangement also allows for fine adjustments of the *xy* interferometer reference mirrors. The moving element of the probing system is floated by the air-bearing that also acts as a linear guide, and by the electromagnetic device controlling the static probing force, as shown in figure 2.7.

The probe (see figure 2.7 and figure 2.8) consists of a conventional diamond stylus (figure 2.7a) attached to one end of a Zerodur rod (figure 2.7b) that is polished and aluminium coated at the opposite end (forming a mirror - figure 2.7c). The rod is coaxially mounted inside a hollow cylinder (figure 2.7d) that forms the air-bearing's piston. One end of the piston has a rectangular cross-section (figure 2.7e and see below) that acts as a stop when the probing system is lifted up and acts as an anti-twisting device. The probing system's moving piston also consists of a hollow cylinder (figure 2.7f) that acts as a spacer for a toroidal permanent magnet (figure 2.7g) that is part of the electromagnetic force control, and an aspheric lens (figure 2.7h), part of the *z* axis interferometer.

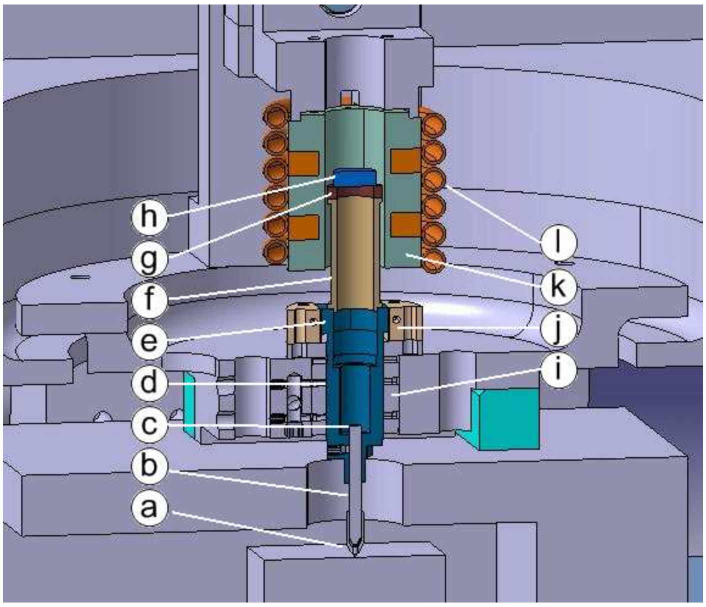

Figure 2.7 Cross-sectional representation of the probing system, where: a) conventional diamond stylus, b) Zerodur rod, c) mirror, d) air bearing piston, e) end of the air bearing piston (part of the anti-twisting device), f) spacer, g) toroidal permanent magnet, h) aspheric lens, i) air bearing, j) anti-twisting device, k) coaxial coils, and l) heat exchanger

Figure 2.8 The probe, showing a conventional diamond stylus and Zerodur rod

The air-bearing was developed by Fluid Film Devices and has two components. The first component is a piston-cylinder air-bearing (figure 2.7i) that operates at a pressure of approximately 400 kPa with a gap large enough to allow the probe to move vertically while providing enough angular stability, or stiffness, in the scanning direction (below 0.5 nm based on a stiffness of 9 × 10^3 kg/mm). The second component is an anti-twisting device (figure 2.7j) that includes two brass components mounted on top of the air-bearing cylinder, acting on two lateral parallel faces of the air-bearing piston head and preventing the probe from turning around its vertical axis. The two brass components represent the fixed parts of a planar air-bearing, so that the physical contact between the probe and the fixed component of the anti-twisting device is eliminated.

The electromagnetic device consists of two nominally identical coaxial coils (figure 2.7k) with electrical currents passing in opposite directions. When the correct distance separates the coils, they exhibit a region of constant field gradient near their mid point (see figure 2.9). The optimal separation for single turn coils is equal to the coil diameter (a Maxwell pair configuration).

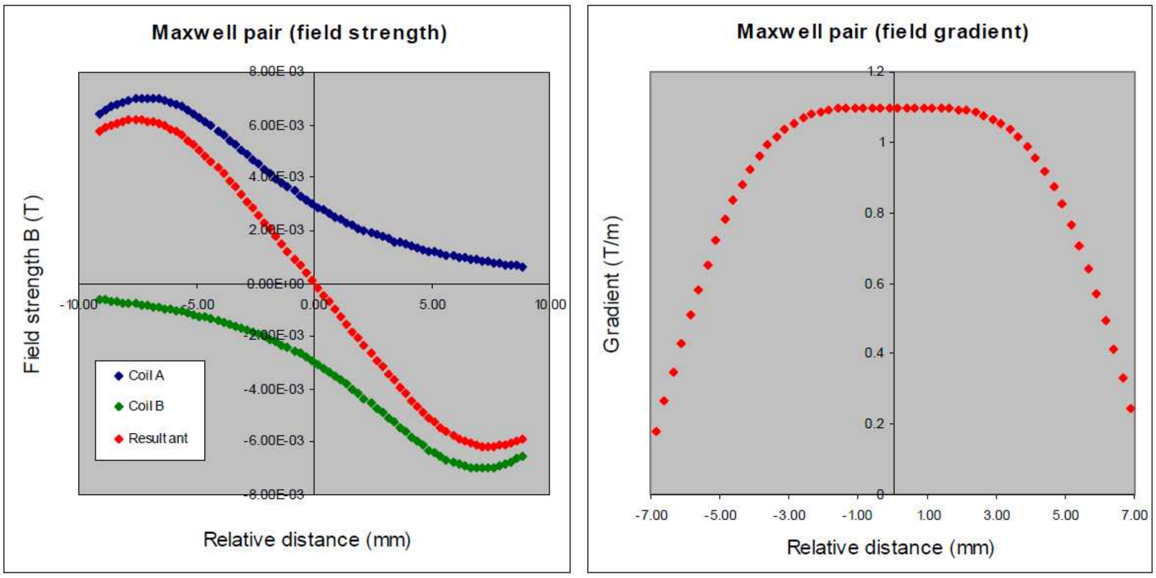

Figure 2.9 Graphs showing the theoretical field strength (left) and field gradient (right) relative to the distance between a permanent magnet and the physical centre of a Maxwellpair at optimum separation (Bayliss *et al.* 2006)

The design uses multiple turn coils (approximately 850 turns of 0.125 mm diameter enamelled copper wire) wound on a ceramic cylinder with an outer diameter of 12 mm, an inner diameter of 10 mm and a length of 4 mm. The coil assembly is capable of generating sufficient force to compensate for the mass of the probe (approximately 6 g) when a current of

0.2 A is applied and a 10.5 mm coil separation is used. This relatively high current produces a significant amount of heat that can directly affect the coil assembly dimensions. The heat is dissipated using a heat exchanger (figure 2.7l and figure 2.10) made from 4 mm diameter copper tube wrapped around the electromagnetic coil assembly. Water at ambient temperature is circulated through the coil by a pump at a rate of forty litres per hour. The coil system including the heat exchanger is mounted on the fixed part of the probing system *via* a dry bearing, allowing for fine adjustments of the coil assembly with regards to the working position of the probe, or more precisely to the position of the toroidal permanent magnet.

Figure 2.10 Cooling coil

The static probing force was measured using a Mettler electronic balance with a resolution of 0.1 mg, corresponding to a force of approximately 1 μN with the electromagnet coils energised by an NPL-designed current source (Hughes and Oldfield 2003) known to provide a very constant and precisely controllable current. The measurement of the probing force was carried out whilst the position of the toroidal magnet inside the coil system was varied by 1 mm, with the coil current and relative position initially applied to achieve a nominal probing force of 0.75 mN. The test showed that the probing force does not fluctuate more that 20 % from its nominal value over the 0.1 mm range.

The probing force is currently monitored using a similar set-up as described by Hughes and Oldfield (2003). The physical constraints of the instrument do not allow for precision mass balance use. Instead, a modified 10 g mass balance with the resolution of 0.001 g is used (see figure 2.11 left). During the probing force measurements, the modified mass balance is placed inside the Zerodur mirror block on top of the Invar vertical stage, allowing the stylus tip to contact the measuring platen (see figure 2.11 right). The Invar stage varies the probe position inside the working range of the instrument whilst the nominal probe position given by the interferometer and the corresponding probe force, measured by the mass balance, are recorded. Typical probing forces are presented in table 2.1.

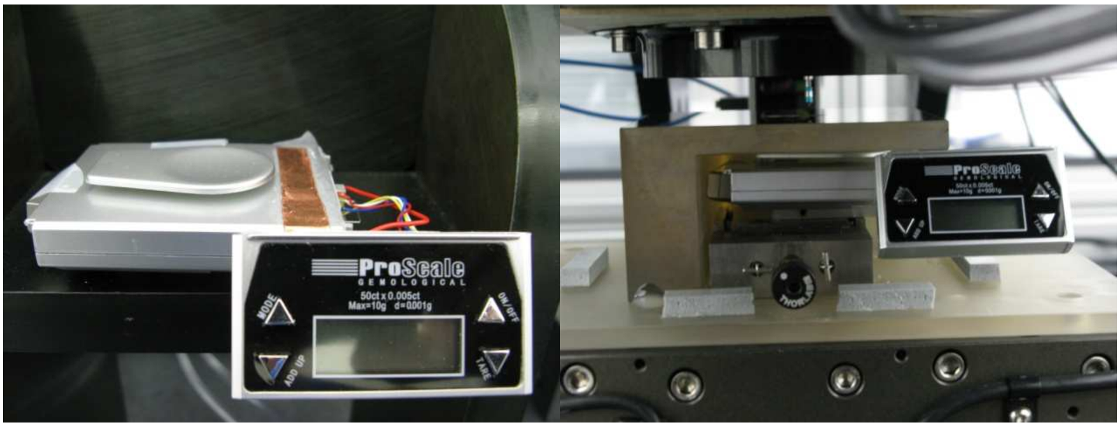

Figure 2.11 Modified mass balance used to test the probing force

2.4 *xy metrology frame*

The displacement of the mirror block in *x* and *y* directions, thus the relative position of the *xy* stage, is determined using a commercial laser interferometer system (Zygo ZMI2000 series) utilising two linear and angular column referenced interferometers attached to the metrology frame (see figure 2.12).

These two interferometers both measure the same angular (yaw) degree of freedom of the *xy* stage to allow for future correction of the geometrical errors (Forbes and Leach 2005).

Table 2.1 Typical probing force values

Probe position/ mm	Probing force / N		
	Run 1	Run 2	Run 3
0.0	0.00	0.00	0.00
0.1	1.09	1.08	1.03
0.3	0.73	0.71	0.69
0.5	0.74	0.71	0.70
0.7	0.76	0.75	0.71
0.9	0.75	0.72	0.70
1.1	0.71	0.68	0.62
0.9	0.75	0.72	0.65
0.7	0.76	0.73	0.69
0.5	0.72	0.69	0.66
0.3	0.71	0.69	0.64
0.1	1.12	1.08	0.98
0.0	0.00	-0.04	-0.07

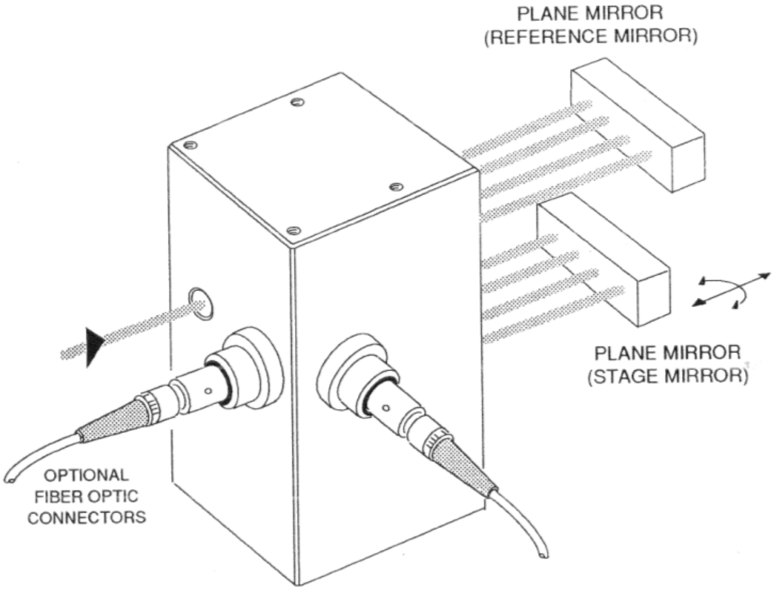

Figure 2.12 Schema of the integrated displacement/angle interferometer ZMI2000 series (Zygo 1993)

The helium-neon frequency-stabilised laser used for the *x* and *y* axis interferometers produces a beam with two components that are collinear, orthogonally polarised and with a heterodyne difference in frequencies of 20 MHz. The laser beam is split in two using a 50/50 beam-splitter. The resulting laser beams are redirected to the input apertures of the *x* and *y* axis interferometers by means of plane mirrors (see figure 2.13 for interferometers layout). The thermal effects of the interferometers' receiver electronics are eliminated because the light output is transmitted to the electronics *via* optical fibre.

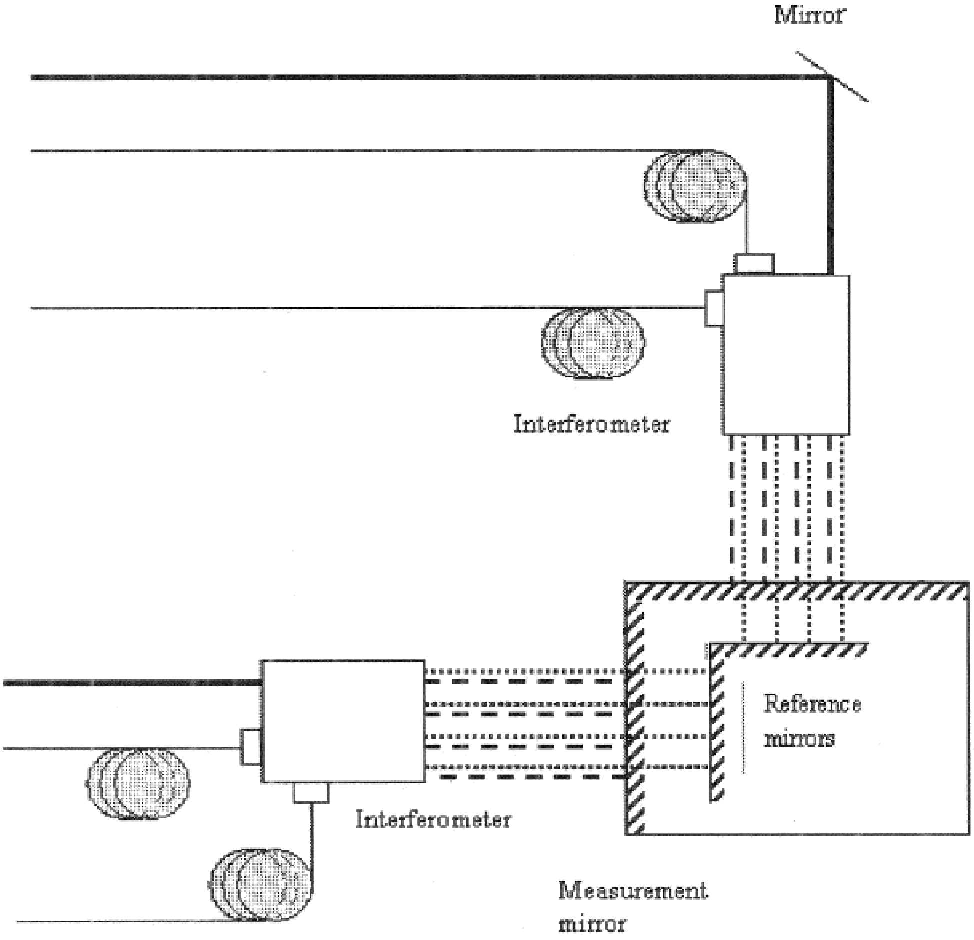

Figure 2.13 Interferometers layout (taken and modified from Forbes and Leach (2008))

The resolution of the *x* and *y* axis interferometers is 0.3 nm, while the angular measurement range is ± 150 seconds of arc (250 mm away from the interferometer), with a resolution of 0.02 seconds of arc. The design of the column referenced interferometer (see figure 2.14) allows the positioning of the reference mirror to be user-defined, which leads to reduced dead-path errors (see ω in figure 2.15), thus the magnitude of the dead-path effect on the laser measurement can be decreased. Provided the measurements are always referenced from the same initial position, the dead-path was estimated to be 25 mm ± 0.6 mm ($k = 1$).

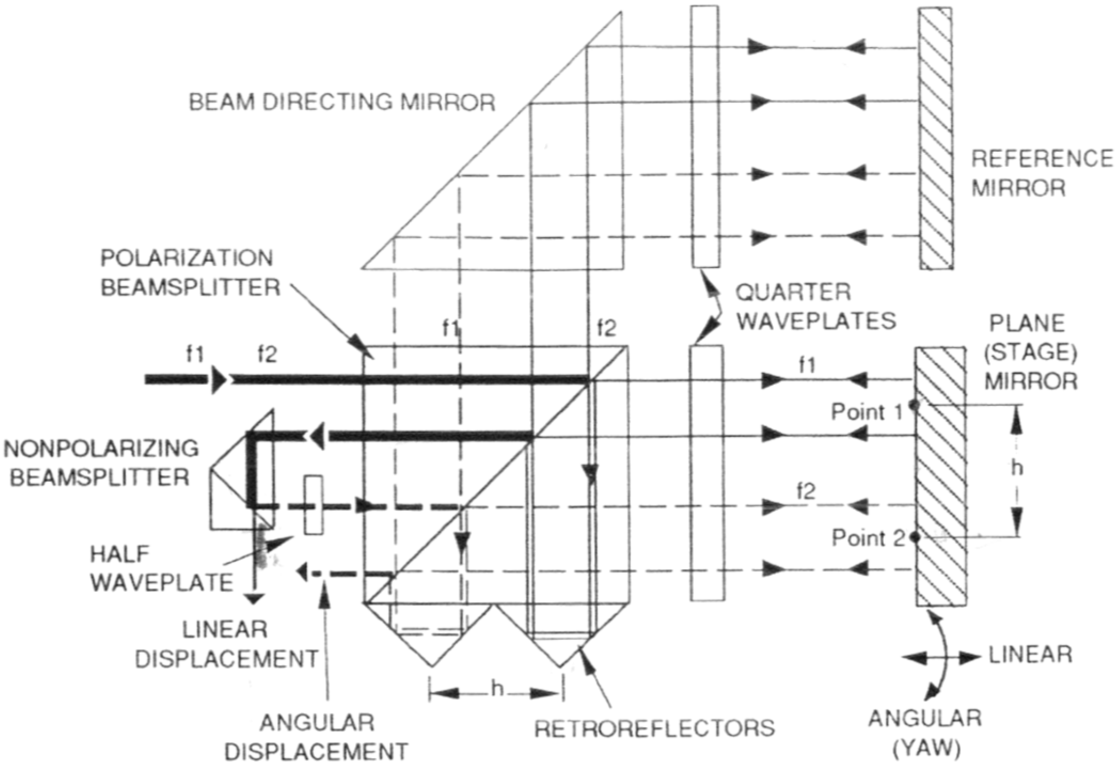

Figure 2.14 Schematic of the *x* and *y* interferometer design (Zygo 1993)

The instrument setup minimises the Abbe offsets by ensuring that the x and y axis interferometers are mounted in such a way that their displacement measuring arm is nominally collinear with the probing system. If the interferometer beams are pointed in a direction, say for instance in the x direction, the Abbe offsets in the y direction are estimated to be 1 mm ± 0.6 mm ($k = 1$), and in the z direction, 5 mm ± 0.6 mm ($k = 1$).

As the room temperature is controlled to 20 °C ± 0.1 °C, the metrology frame thermo-mechanics have only secondary effects in estimating the Abbe errors. However, the effect of the frame thermo-mechanics along the measuring direction is illustrated schematically in figure 2.15. The solid lines represent the system at a particular temperature (t_0) and the dotted lines correspond to the system at $t_0 + \Delta t$, where Δt is a small temperature variation of the system. The upper horizontal line, starting from point A, is the reference beam path and the lower horizontal line, starting from point B, is the measuring beam path. The probing system at t_0, represented by the right most solid vertical line, moves naturally to a position along the measuring direction, represented by the right most doted-vertical line, when the system changes its temperature by Δt.

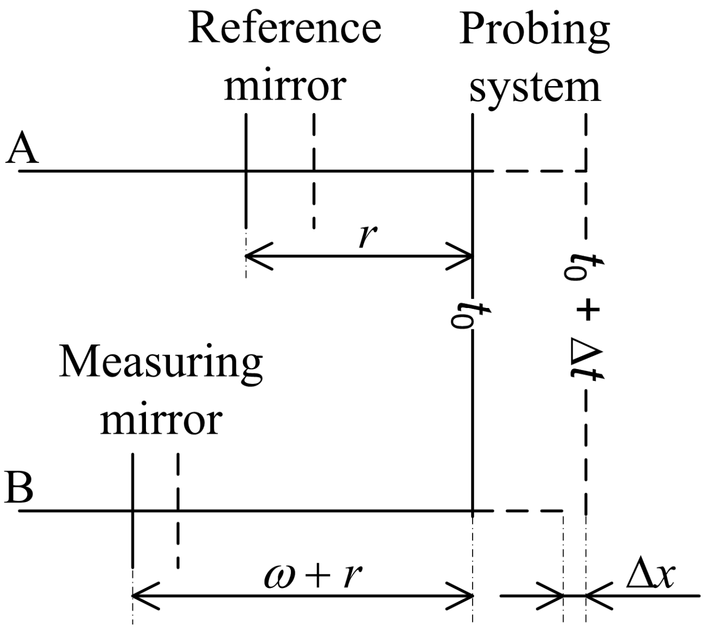

Figure 2.15 Errors caused by metrology frame thermo-mechanics

If the base of the metrology frame is not made of similar material to the upper part, the point of contact between the probe and the sample moves by Δx relative to the initial contact point. Since the interferometer will record the relative change between the measuring mirror and the reference mirror along the measuring path, $\Delta x_{\text{measured}}$, the error will be:

$$\Delta x - \Delta x_{measured} = \omega \alpha_1 \Delta t + r(\alpha_1 - \alpha_2)\Delta t, \qquad 2.1$$

where ω is the dead-path length at t_0, r is the distance between the reference mirror and the probing system at t_0, and α_1 and α_2 are the linear thermal expansion coefficients for the upper part of the metrology frame (steel) and for its lower part (granite) respectively. Considering $\omega = 25$ mm, $r = 30$ mm, $\alpha_1 = 11.5\ ^{-5}\ \mathrm{K}^{-1}$, $\alpha_2 = 4 \times 10^{-6}\ \mathrm{K}^{-1}$ (Kaye and Laby 1995) and $\Delta t = 0.05$ °C (appropriate value for a two hour scan using the NPL Areal Instrument), an error of 4 nm is found along the measuring direction.

A further geometric error is due to the laser misalignment. The interferometers have been aligned with deviations from the mirror surface normal smaller than thirty seconds of arc (manufacturer's specification). This translates to a cosine error of less than 0.11 nm for a maximum measured length of 10 mm.

The above-mentioned errors are mainly caused by the interaction between the laser interferometer and instrument geometry. The intrinsic properties of the laser interferometers generate a different set of errors. The influence quantities that generate these errors can be split into three categories, depending on which component of the laser interferometer is the error source: laser source, interferometer characteristics and detection system (Leach 1999).

Laser source influence quantities include short and long-term calibration of the laser frequency, frequency stability, intensity stability, beam characteristics and polarisation. While the contribution of the laser short and long-term stability and its frequency stability could be estimated using data provided by calibration certificates, the contribution of the remaining influence quantities is difficult to predict theoretically. The uncertainty associated with the frequency stability of the laser is estimated to be ten parts per billion of the measured length ($10^{-8} L$ where L is the measured length in metres) at $k = 1$. The intensity stability, beam characteristics and polarisation will have an effect on the instrument noise, therefore, their contribution will be determined during the instrument noise tests.

The interferometer influence quantities include the effects of collimation/obliquity, the quality of the optical components, stray beams, diffraction, air refractive index, dead-path error, air turbulence and interferometer resolution. Collimation and obliquity effects, diffraction effects and air turbulence effects will add to the instrument noise. The uncertainty associated with the quality of the optical components and the stray beams was previously calculated for a similar interferometer to be 0.23 nm ($k = 1$) (Leach 1999). The diffraction effects have sub-picometre magnitude thus they can be neglected. The uncertainty associated with the air refractive index is of the order of fifty parts per billion of the measured length ($5 \times 10^{-8} L$, $k = 1$), including contributions from the Edlén equation (Birch and Downs 1994), vacuum wavelength, pressure, temperature, humidity and levels of carbon dioxide. The dead-path contribution to the measurement uncertainty is 0.4 nm ($k = 1$). The detection system contributes to the instrument noise. The laser interferometer resolution is 0.3 nm.

The instrument noise tests (3000 points sampled at frequencies ranging from 10 Hz to 1 kHz) showed that in static mode (when the stage was kept at a particular location) the standard deviation did not exceed 5 nm, and in dynamic mode (when the stage was moved along x direction) the standard deviation was less than 8 nm. The latter noise tests include the mirror geometry.

Summarising, the uncertainty associated with the laser interferometer measurements, excluding the random effects and geometrical influence quantities, is 0.7 nm ($k = 1$) for a 10 mm displacement of the stage in one direction.

2.5 z metrology frame

The displacement in z direction of the probe in response to the surface topography is measured by a differential plane mirror interferometer (see figure 2.16) (Downs *et al.* 1995). The incident laser beam is divided into two parallel components using a Jamin beam-splitter (Raine and Downs 1978). Further polarisation optics, namely a polarising beam-splitter and a retro-reflector produce a plane mirror interferometer. The aspheric lens focuses the interferometer measuring beams onto the mirror on the upper end of the Zerodur rod. The interferometer is referenced from a plane mirror mounted on the xy stage above the sample. The beams are transmitted back to the Jamin beam-splitter after a double passage through the wave plate. The coatings applied on the Jamin beam-splitter allow the beams to recombine in such way that the two photo-detectors capture signals in phase quadrature (Raine and Downs 1978).

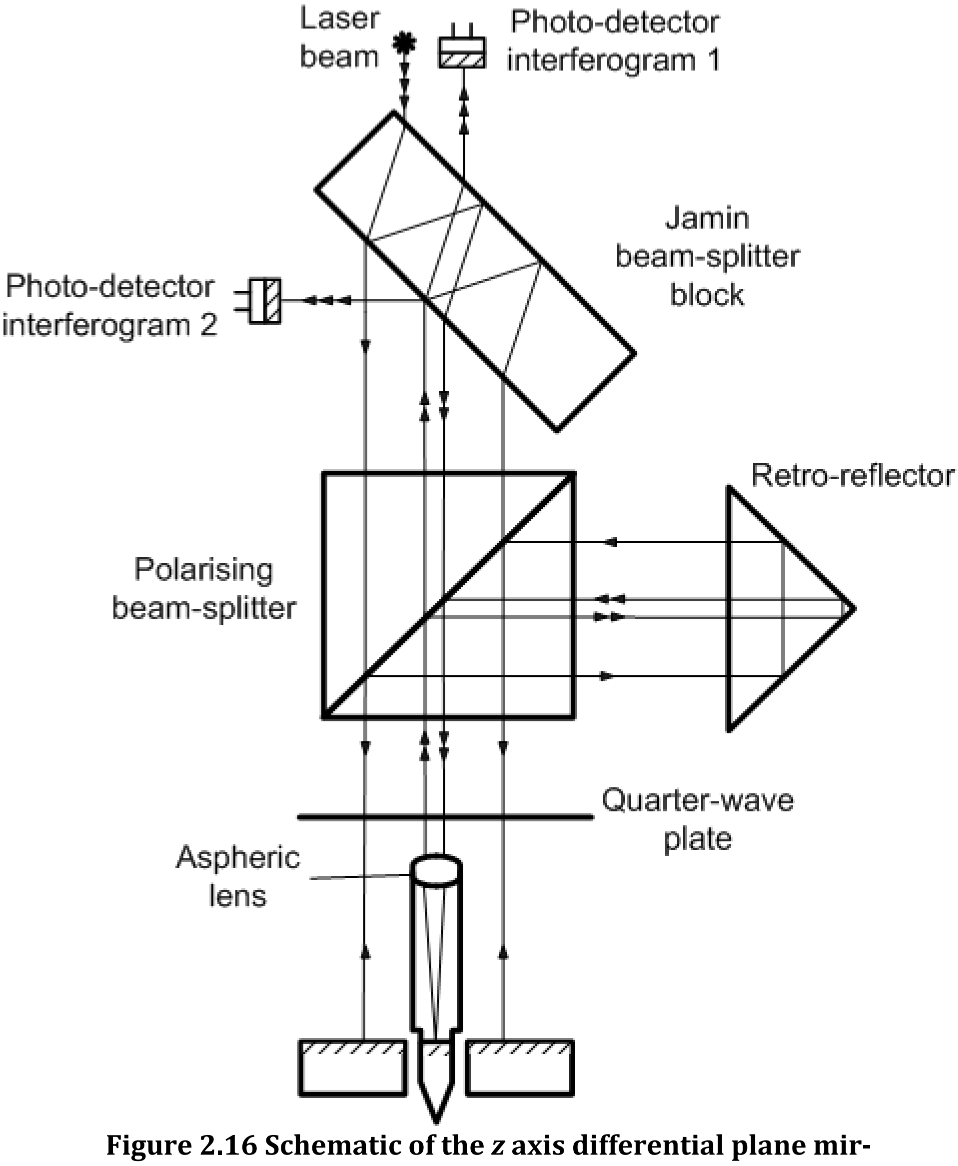

Figure 2.16 Schematic of the *z* axis differential plane mirror interferometer

The main advantage of this configuration of interferometer is that only the relative displacement between the reference and measuring mirror is recorded, so the thermal and mechanical instabilities of the metrology frame are minimised, although the effect of the spacers and rising stage is not removed. The differential plane mirror interferometer has been shown to have sub-nanometric measurement capabilities (Yacoot and Downs 2000).

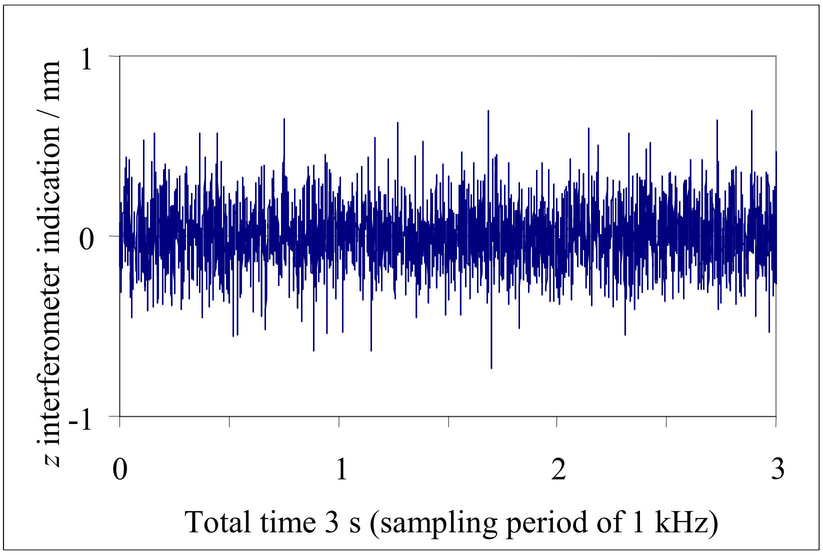

Figure 2.17 *z* axis interferometer noise test using a plane mirror

Figure 2.17 shows the level of noise of the interferometer reading when both sets of beams (measurement and reference respectively) target the same plane mirror. The standard deviation is 0.17 nm. The *z* axis interferometer noise is increased by the air-bearing flow that crosses the beam paths and by instabilities in the electromagnetic system (see figure 2.18).

The *z* axis interferometer optics, including the laser source, are bolted onto a rigid metal plate and mounted vertically on the metrology frame using a similar kinematic mount to that used for the probing system. This arrangement allows the orientation of the interferometer to be varied with respect to the reference mirror located on the translation stage. The interferometer can also translate in the horizontal plane, which allows location of the probe optics.

As the *z* axis interferometer is nominally in line with the probe axis, the Abbe errors are given by the position of the tip-sample contact point with respect to the probe vertical axis. The locus of contact points between the probe and the sample is the surface of the stylus tip, consequently the maximum Abbe error is equal to the radius of the stylus tip.

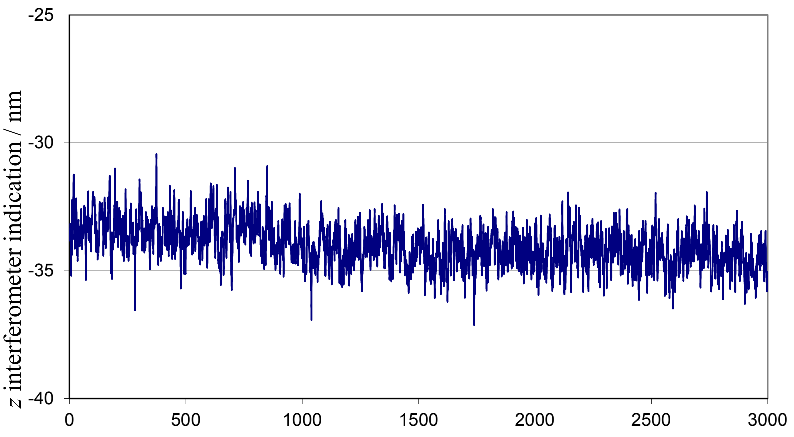

Total time 3 s (sampling period 1 kHz)

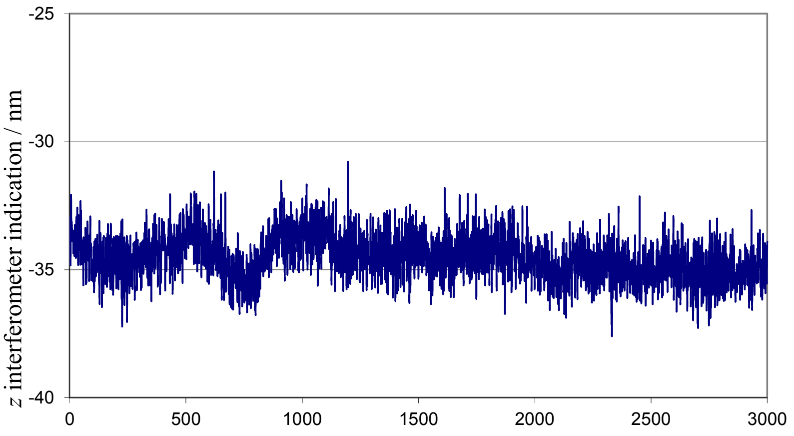

Total time 1 min (sampling period 50 Hz)

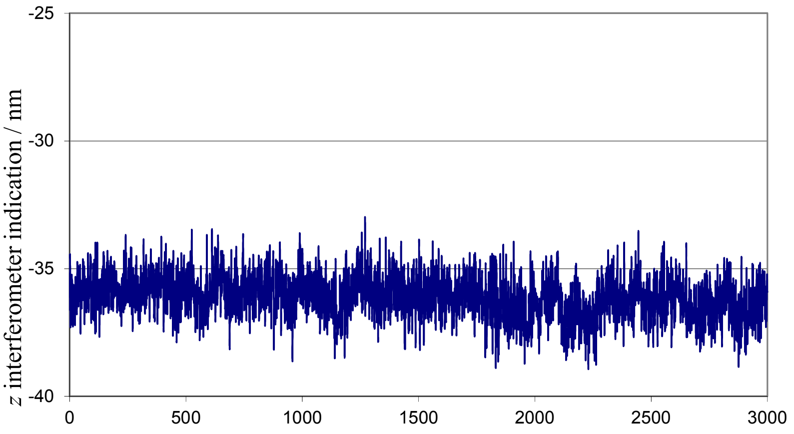

Total time 2.5 min (sampling period 20 kHz)

Figure 2.18 Static noise tests

The design of the instrument allows for the z axis interferometer measuring mirror to be positioned approximately at the same level as the z axis reference mirror plane, leading to a reduced dead-path length. The dead-path is no more than 1 mm.

Although the thermo-mechanical errors could be significant in displacement measurements, they will only affect the measured waviness of the surface. For a silicon wafer that is 1 mm thick, the thermo-mechanical error caused by a temperature variation of $\Delta t = 0.05$ °C is approximately 3 nm, whereas for a steel sample that is 20 mm thick the error is increased to approximately 11 nm. However, waviness is eliminated by the post measurement filtering process, thus this contribution to the uncertainty is not included when assessing surface roughness.

The cosine errors in the z axis are negligible because the z axis interferometer measures small distances. A deviation as large as 30 seconds of arc of the laser beams' direction from the mirror normal does not generate an error larger than 1 pm over the full z axis range.

The influence of the laser interferometer intrinsic properties on the displacement measurements discussed in this section above, are also applicable to the z axis interferometer. The only major difference between the interferometers is the choice of the laser source. The z axis laser is not frequency stabilised. The uncertainty contribution associated with laser short and long-term frequency calibration, and its frequency stability is estimated to be approximately one part per million of the measured length ($10^{-5}\,L$, for $k = 1$). Despite the relative increase of the latter contribution, its absolute value remains small, as the maximum measured length in the z direction is approximately 0.1 mm. The uncertainty associated with the z axis laser interferometer measurements is estimated to be 0.56 nm ($k = 1$) excluding the random effects, geometrical influence quantities and the dead-path contribution that is compensated for by filtering.

The standard deviation of the noise during static tests was found to be 0.8 nm, whereas the dynamic noise tests revealed that the standard deviation was no greater than 1.5 nm.

2.6 Measurement model

The formulation of the NPL Areal Instrument measurement model involves an analysis of the measurement system, *i.e.* an analysis of the interaction between the instrument's sub-systems that were presented in the previous section. A description of the instrument functionality is required to establish the correct measurement model.

With reference to figure 2.19, the *xy* stage movement from one position to another is a combination of two displacements along two nominally perpendicular directions in the horizontal plane. These two orthogonal directions are physically defined by the stage *x* and *y* axes. The stage displacement along each one of these two orthogonal directions is affected by small rotational errors (α_l).

The stage displacements in the *x* and *y* directions are measured by the two linear and angular column referenced interferometers, the *x* and *y* interferometers. The interferometers measure the distance, w_{jl} between a reference mirror and a measuring mirror. The *x* and *y* reference mirrors, positioned on the probe fixed body, are not drawn in figure 2.19. The translation axes of the *xy* stage are nominally orthogonal to the planes of their respective measuring mirrors. Since the *x* and *y* interferometers are aligned to be nominally normal to their corresponding reference and measuring mirrors, the Zerodur block establishes the perpendicularity of the measuring system.

A separate error source associated with the mirrors' geometry is the flatness (see figure 2.19 inset); any departure from the ideal plane of the mirrors reflecting surface will translate into a displacement error.

The length measurements, the estimates of w_{jl}, are also affected by other factors such as alignment errors (cosine and Abbe offsets), dead-path errors, thermo-mechanical effects and intrinsic properties of the laser interferometers.

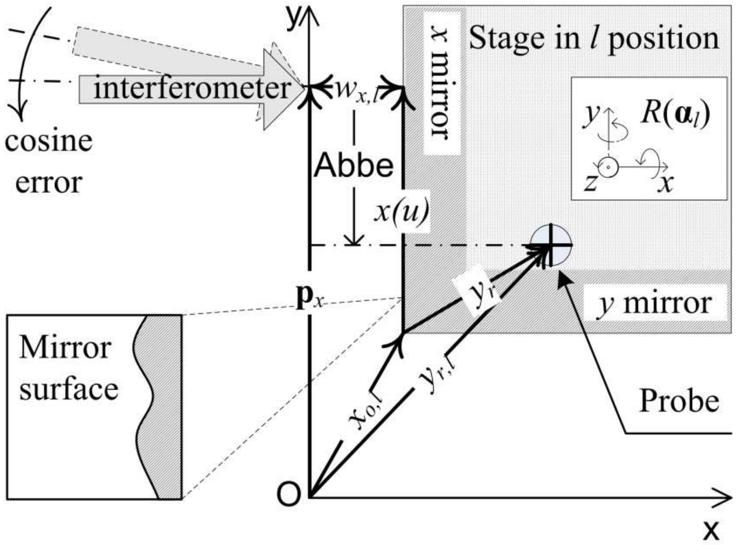

Figure 2.19 Schema of a top plan view of the NPL Areal Instrument: $\mathbf{p}_x$ is the x interferometer position vector, w_{xl} is the distance between the interferometer and mirror surface, $x_{0,l}$ is the mirror block position vector, $x(u)$ is a position vector that describes a point on the mirror, $y_{r,l}$ is the target position vector and y_r is the target position vector in the stage reference frame

According to Forbes and Leach (2005), any position (*l*) of the stage can be precisely estimated using three sets of three equations. The measurement model formulation starts with equation 2.2,

$$\boldsymbol{p}_j + w_{j,l}\boldsymbol{s}_j = \boldsymbol{x}_{0,l} + R^T(\boldsymbol{\alpha}_l)N_{0,k}^T\begin{bmatrix} u_{j,l} \\ v_{j,l} \\ h_k + g(u_{j,l}, v_{j,l}) \end{bmatrix}. \qquad 2.2$$

Each set of equations models a single interferometric measurement. The left hand side of equation 2.2 represents a point on the j^{th} interferometer laser beam ($j = x$, y or z) and the term on the right hand side of equation 2.2 describes a point on the k^{th} target mirror surface ($k = x$, y or z). $\mathbf{p}_j$ is the j^{th} interferometer position vector and $\mathbf{s}_j$ is a direction vector. $\mathbf{p}_j$ and $\mathbf{s}_j$ jointly define a line in 3D representing the j^{th} interferometric measuring beam. $\mathbf{s}_j$ is the product of a fixed rotation matrix ($S_{0,j}$), and the beam direction vector ($\mathbf{e}_z$), *i.e.*

$$\boldsymbol{s}_j = S_{0,j}^T \boldsymbol{e}_z. \tag{2.3}$$

$\mathbf{p}_j$ and $S_{0,j}$ contain information on the Abbe offset and cosine error, respectively. $w_{j,l}$ is an estimate of the distance between the j^{th} reference mirror and the j^{th} measuring mirror, with the stage in the l^{th} position. If $^*\mathbf{x}_{j,l}$ is the point of intersection of the beam with the mirror surface then the (signed) distance $D_{j,l}$ between the measuring and the reference mirror surfaces along the beam is given by

$$D_{j,l} = \left(\boldsymbol{p}_j - {}^*\boldsymbol{x}_{j,l}\right)^T \boldsymbol{s}_j = w_{j,l}. \tag{2.4}$$

The j^{th} interferometer measurement output with the xy stage in the l^{th} position is modelled by

$$d_{j,l} = D_{j,l} - \omega_j + \varepsilon_{j-r} + \varepsilon_{j-s}, \tag{2.5}$$

where ω_j is a fixed offset that accounts for the dead-path, $\varepsilon_{j\text{-}r}$ accounts for random measurement errors and $\varepsilon_{j\text{-}s}$ accounts for systematic effects generated by the interferometers' intrinsic properties.

$\mathbf{x}_{0,l}$ and $R(\boldsymbol{\alpha}_l)$ in equation 2.2 define the stage motion. $\mathbf{x}_{0,l}$ specifies the translation of the stage $(x_{0,l}, y_{0,l}, z_{0,l})^{\mathrm{T}}$ and $R(\boldsymbol{\alpha}_l)$ specifies the stage rotation. $R(\boldsymbol{\alpha}_l)$ is the product of three plane rotation matrices corresponding to the stage rotation angles $\boldsymbol{\alpha}_l$ (tilt $\alpha_{0,l}$, roll $\beta_{0,l}$ and yaw $\gamma_{0,l}$).

The last two terms of the equation 2.2, $N_{0,k}$ and $(u_{j,l}, v_{j,l}, h_k + g(u_{j,l}, v_{j,l}))^{\mathrm{T}}$ define the mirror's geometry. $N_{0,k}$ is a fixed rotation matrix that describes the mirror's perpendicularity. $(u_{j,l}, v_{j,l}, h_k + g(u_{j,l}, v_{j,l}))^{\mathrm{T}}$ describes the shape of the mirror as a function of the parameters $u_{j,l}$ and $v_{j,l}$. h_k is the nominal surface height and the function g describes the form error. It is expected that g is close to zero.

The xy stage moves to align a set of targets $\{\mathbf{y}_r\}$ $(r = 1 : n_{ri})$ with a fixed probing location O which are taken to be the origin ($y_{rl} = 0$ in figure 2.19) so that

$$\boldsymbol{x}_{0,l} + R^T(\boldsymbol{\alpha}_l)\boldsymbol{y}_l = 0. \qquad 2.6$$

Equation 2.2 can be written in terms of $\mathbf{y}_r$:

$$\boldsymbol{y}_r = N_{0,k}^T \begin{bmatrix} u_{j,l} \\ v_{j,l} \\ h_k + g(u_{j,l}, v_{j,l}) \end{bmatrix} - R(\boldsymbol{\alpha}_l)(\boldsymbol{p}_j + w_{j,l}\boldsymbol{s}_j). \qquad 2.7$$

Equation 2.7 models the measurement of a point co-ordinate, where $\mathbf{y}_r$ is the output quantity and the rest of the terms are the input quantities upon which $\mathbf{y}_r$ depends. If the mirror geometry and angular motion are taken to be ideal, equation 2.7 involves three equations in six unknowns. Taking all three axis, there are nine equations in twelve unknowns. The three interferometer measurements of $w_{j,l}$ provide another three equations that allow $\mathbf{y}_r$ to be estimated.

For areal surface texture investigations, the $\mathbf{y}_r$ co-ordinate measurements are referenced to an arbitrary point on the surface, $\mathbf{y}_i$, that is also given by equation 2.7, so that

$$\boldsymbol{y}_r = \boldsymbol{y}_r + \boldsymbol{y}_i. \qquad 2.8$$

Equations 2.7 and 2.8 represent the NPL Areal Instrument measurement model.

A full list of the input parameters and their associated probability density functions (PDFs) is given in table 2.2. The values given in table 2.2 are appropriate values for the NPL Areal Instrument.

2.7 Uncertainty estimation

The uncertainty associated with the point co-ordinate measurement was calculated using a Monte Carlo approach (BIPM 2008b). Using equations 2.7 and 2.8 for each of the three mirrors, the coordinates y_r of the target can be expressed as a function of the other parameters in the model.

Table 2.2 Input quantities and their associated probability density functions (PDFs). R(*a*, *b*) is a rectangular distribution and N(*x*, $u^2(x)$) is a Gaussian distribution.

Quantity / unit	PDF
Position and orientation of *x* interferometer	
p_{xx} / mm	R(15.999 996, 16.000 004)
p_{xy} / mm	R(4.5, 5.5)
p_{xz} / mm	R(0.5, 1.5)
α_x / mrad	R(−0.15, 0.15)
β_x / mrad	R($10^3 \times \pi/2 - 0.15$, $10^3 \times \pi/2 + 0.15$)
γ_x / mrad	R(−0.15, 0.15)
Position and orientation of *y* interferometer	
p_{yx} / mm	R(0.5, 1.5)
p_{yy} / mm	R(−16.000 004, −15.999 996)
p_{yz} / mm	R(4.5, 5.5)
α_y / mrad	R($10^3 \times \pi/2 - 0.15$, $10^3 \times \pi/2 + 0.15$)
β_y / mrad	R(−0.15, 0.15)
γ_y / mrad	R(−0.15, 0.15)
Position and orientation of *z* interferometer	
p_{zx} / mm	R(−0.002, 0.002)
p_{zy} / mm	R(−0.002, 0.002)
p_{zz} / mm	R(0.199 997, 0.200 003)
α_z / mrad	R(−0.15, 0.15)
β_z / mrad	R($10^3 \times \pi - 0.15$, $10^3 \times \pi + 0.15$)
γ_z / mrad	R(−0.15, 0.15)
xy stage rotation	
$\alpha_{0,l}$ / µrad	R(−0.97, 0.97)
$\beta_{0,l}$ / µrad	R(−0.97, 0.97)
$\gamma_{0,l}$ / µrad	R(3.8, 5.8)
Mirrors perpendicularity and flatness	
$^N\beta_{xy}$ / µrad	R($-10^6 \times \pi/2 - 0.97$, $-10^6 \times \pi/2 + 0.97$)
$^N\gamma_{xz}$ / µrad	R(−0.97, 0.97)
$^N\alpha_{yx}$ / µrad	R($10^6 \times \pi/2 - 0.97$, $10^6 \times \pi/2 + 0.97$)
h_x / mm	N(0, $0.000\,007^2$)
h_y / mm	N(0, $0.000\,007^2$)
h_z / mm	N(0, $0.000\,001\,5^2$)
Dead-path and laser contribution	
ω_x / mm	N(25, $0.000\,000\,4^2$)
ω_y / mm	N(25, $0.000\,000\,4^2$)
ω_z / mm	N(5, $0.000\,000\,1^2$)
ε_x / mm	N(0,$0.000\,000\,7^2$)
ε_y / mm	N(0,$0.000\,000\,7^2$)
ε_z / mm	N(0,$0.000\,000\,56^2$)

By assigning distributions to these parameters, the uncertainties associated with the estimates of the target co-ordinates can be evaluated. The instrument is considered to be well characterised, *i.e.* all the input parameters and random effects are well known.

The Monte Carlo approach is a sampling method for estimating the uncertainty of measurement. The method generates a random value for each input quantity according to its assigned PDF, then calculates the output quantity value for these sampled input quantity values. In this way, a sample from the output distribution is calculated from which means, standard deviations, coverage intervals, *etc.*, can be estimated.

The recommended steps for estimating the uncertainty using a Monte Carlo approach are (Cox and Harris 2006):

- Select the number of trials (n).
- Generate n input quantity vectors by sampling from their PDFs.
- Calculate the value of the output quantity corresponding to each input quantity vector.
- Obtain the mean and standard deviation of the calculated output quantity values.

In these experiments, $n = 50\ 000$ trials were found to be adequate for producing stable results. The uncertainties were evaluated for a set of target locations aligned as a 3D grid of points (parallelepipedic grid) uniformly distributed in a working volume of 8 mm by 8 mm by 0.1 mm. For simplicity a 3 × 3 × 3 grid was chosen resulting in twenty seven targets ($\mathbf{y}_r$).

2.7.1 Validation

To validate the Monte Carlo approach, the uncertainty associated with the point co-ordinate measurement was estimated using the conventional GUM approach (BIPM 2008a).

The GUM approach is an approximate, analytical method for estimating the uncertainty of measurement. Knowing the PDFs, summarized by their means and standard deviations, for the input quantities, the GUM approach aim is to derive an estimate of the mean and standard deviation for the distribution associated with the output quantity. In order to evaluate a coverage interval, the output quantity is characterized by a Gaussian distribution or a t-distribution. The GUM approach method of propagating the uncertainty consists of the following steps:

- Assign PDFs to the input quantities and evaluate their means and standard deviations.
- Evaluate the covariances of mutually dependent input quantities.
- Form the first order partial derivatives of the output quantity with respect to the input quantities.
- Calculate an estimate of the output quantity using the given values for the input quantities.
- Calculate the sensitivity coefficients by evaluating the partial derivatives for the given input quantity values.
- Calculate the output quantity standard uncertainty by combining the sensitivity coefficients and input quantity standard uncertainties and covariances.
- If required, calculate the effective degrees of freedom associated with the output quantity standard uncertainty.

For these calculations, it was considered that all input quantities were uncorrelated, and as a result no covariance terms were needed. The partial derivatives of first order were calculated numerically using the complex step method (Squire and Trapp 1998). Taylor expansion for a complex function is

$$f(x+ih) = f(x) + ihf'(x) - \frac{h^2}{2}f''(x) - i\frac{h^3}{3!}f'''(x) + \frac{h^4}{4!}f''''(x) + \cdots \quad 2.9$$

where x is real and h is real and small. The imaginary part is

$$\Im f(x+ih) = hf'(x) - \frac{h^3}{3!}f'''(x) + \frac{h^5}{5!}f'''''(x) + \cdots \qquad 2.10$$

For small h (software implementation $h = 10^{-100}$), the terms on the right hand side of the equation 2.10 that contain powers of h can be ignored, so partial derivatives of first order can be computed using equation 2.11.

$$f'(x) = \frac{\Im f(x+ih)}{h}. \qquad 2.11$$

The GUM approach results are similar to the results obtained using the Monte Carlo approach (see table 2.3). There is only a small difference between the GUM and Monte Carlo results for the uncertainties associated with the lateral coordinate measurements, x and y directions, of approximately 1 %. The agreement between these two methods is expected because the model is essentially linear and the variations associated with the influence quantities are small. The only significant source of nonlinearity is associated with the laser beam alignment that contributes a cosine error.

If the uncertainties associated with the laser alignment are increased by a factor of ten, the GUM approach does not show an increase in the value of the associated uncertainty, but the Monte Carlo uncertainties associated with the x and y coordinate estimates increase from approximately 8 nm to 35 nm. The difference between the GUM and Monte Carlo in the latter scenario is once again expected, as the sensitivity coefficients calculated in the GUM approach for the laser alignment are approximately equal to zero so that the GUM (first order) approach effectively ignores this influence quantity.

In addition, measurements of various material measures using the NPL Areal Instrument were performed. To date, the NPL Areal Instrument has been tested with type PGR step height material measures (ISO 5436-1 2000) and type ACG material measures (ISO/DIS

25178-70 2009). The type PGR material measures were manufactured on the same silicon wafer as the type ACG, as described in detail elsewhere (Haycocks *et al.* 2005).

Table 2.3 GUM and Monte Carlo results . $u(x)$, $u(y)$ and $u(z)$ are standard uncertainties

Targets			GUM results			Monte Carlo results		
x / mm	y / mm	z / mm	u(x) / nm	$u(y)$ / nm	$u(z)$ / nm	$u(x)$ / nm	$u(y)$ / nm	u(z) / nm
−4.00	4.00	0.10	8.56	8.56	3.09	8.61	8.63	3.10
−4.00	4.00	0.00	8.54	8.54	3.09	8.59	8.61	3.10
0.00	4.00	0.10	8.56	8.56	3.09	8.61	8.63	3.10
0.00	4.00	0.00	8.54	8.54	3.09	8.60	8.61	3.10
4.00	4.00	0.10	8.56	8.56	3.09	8.62	8.63	3.10
4.00	4.00	0.00	8.54	8.54	3.09	8.60	8.61	3.10
−4.00	0.00	0.10	8.56	8.56	3.09	8.61	8.63	3.10
−4.00	0.00	0.00	8.54	8.54	3.09	8.59	8.62	3.10
0.00	0.00	0.10	8.56	8.56	3.09	8.61	8.63	3.10
0.00	0.00	0.00	8.54	8.54	3.09	8.60	8.62	3.10
4.00	0.00	0.10	8.56	8.56	3.09	8.62	8.63	3.10
4.00	0.00	0.00	8.54	8.54	3.09	8.60	8.62	3.10
−4.00	−4.00	0.10	8.56	8.56	3.09	8.61	8.64	3.10
−4.00	−4.00	0.00	8.54	8.54	3.09	8.59	8.62	3.10
0.00	−4.00	0.10	8.56	8.56	3.09	8.61	8.64	3.10
0.00	−4.00	0.00	8.54	8.54	3.09	8.60	8.62	3.10
4.00	−4.00	0.10	8.56	8.56	3.09	8.62	8.64	3.10
4.00	−4.00	0.00	8.54	8.54	3.09	8.60	8.62	3.10

Each type PGR artefact has two wide grooves with flat bottoms and widths of 100 μm and 500 μm. The depths of the grooves of the type PGR material measures are nominally 100 nm and 1 µm. Figure 2.20 shows an isometric plot of the 1 µm step artefact that was obtained using the NPL Areal Instrument and a commercial software package (Digital Surf 2011).

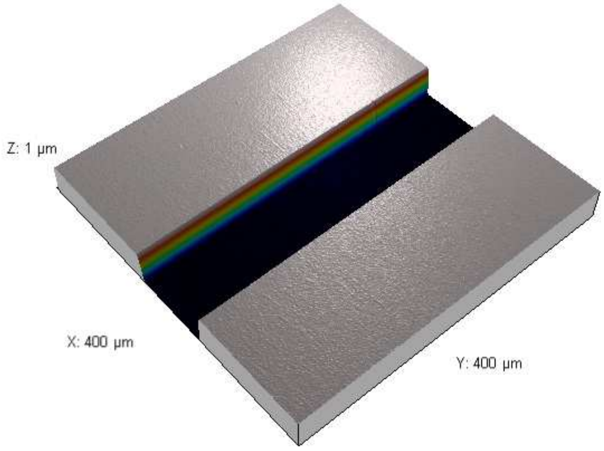

Figure 2.20 1000 nm step, 0.1 mm wide

The NPL Areal Instrument step height measurement results were compared with results obtained using NanoSurf IV (NS4), the NPL primary surface texture profile measuring instrument (Leach 2000). The NS4 measurements consisted of four sets of five profiles across the step heights and the NPL Areal Instrument measurements consisted of four scans of the step heights of 512 × 512 points. Five profiles from each scan from the NPL Areal Instrument were selected for analysis. The NS4 and the NPL Areal Instrument step measurement results, and the associated standard deviations are presented in table 2.4.

Table 2.4 Areal Instrument and NS4 step height measurements results, analysed using the method in ISO 5436-1 (2000), where σ is the sample standard deviation

Sample	Areal Instrument		NS4		Areal - NS4	$(\sigma_{\mathrm{Areal}}^2 + \sigma_{\mathrm{NS4}}^2)^{½}$
	height / nm	σ / nm	height / nm	σ / nm	/ nm	/ nm
100 broad	90.3	0.1	87.4	2.8	2.9	2.8
100 narrow	91.9	0.2	91.6	0.8	0.3	0.8
1000 broad	971.0	0.4	968.9	5.0	2.1	5.0
1000 narrow	969.1	0.9	970.7	5.0	-1.6	5.0

The NPL Areal Instrument step height measurement results agree with the NS4 results within the combined standard deviation.

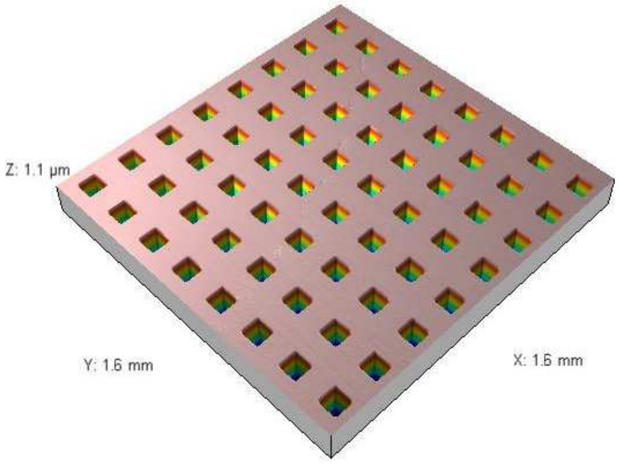

Figure 2.21 Areal image of type ACG material measures 200 µm pitch and 1 µm depth

Type ACG material measures were characterised by a coherence scanning interferometer (CSI) using a 10× magnification objective (note that this just gives confidence in the results as the CSI instrument was at the time of the theses not traceable). Both sets of data, the NPL Areal Instrument data set and the CSI data set, were imported for analysis into a commercial software package. The average pitch was estimated using the mean width of the raw profile elements (PSm), calculated from three profiles across the measured area. The NPL Areal Instrument measurements on a 200 µm pitch and 1 µm depth type ACG artefact (figure 2.21) give a PSm value of 200.17 µm with a standard deviation of 0.15 µm. The CSI measurements on the same type ACG artefact results in a PSm of 199.97 µm and 0.15 µm standard deviation. The difference between the two PSm values (0.2 µm) is well within the limits defined by their standard deviation combined (0.21 µm).

2.7.2 Discussion of the Monte Carlo results

The uncertainty associated with the instrument point co-ordinate measurement depends on a combination of factors such as stage motion, system geometry and the quality of interferometric measurements. The combined, as well as the individual, effect of these factors on the instrument associated uncertainty has been investigated for five cases of interest: perfect geometry; perfect motion, perfect geometry; imperfect motion, imperfect geometry; perfect motion, mirrors' geometry and all factors combined. The four case studies simulation results are presented in table 2.5.

Table 2.5 Uncertainty simulations results. *u(x)*, *u(y)* and *u(z)* are standard uncertainties

Case study	$u(x)$ / nm	$u(y)$ / nm	$u(z)$ / nm
perfect geometry - perfect motion	2.3	2.3	0.9
perfect geometry - imperfect motion	2.9	2.9	0.0016
imperfect geometry – perfect motion	2.4	2.4	1.9
mirrors' geometry	7	7	1.5
all factors	8.0	8.0	2.4

In the perfect geometry–perfect motion case only the PDFs associated with the interferometric measurements were propagated. The input parameters considered for this case were the dead-path, the laser interferometer intrinsic properties and the random measurement errors.

The random errors of the x, y and z interferometers were estimated when the instrument was tested for static noise (the xy stage not moving). Random measurement errors of 2.1 nm standard deviation for the x and y interferometers and 0.6 nm standard deviation for the z interferometer were measured.

The PDFs corresponding to the rest of the input parameters were ignored. In other words, the perfect geometry–perfect motion case considered the stage displacement without rotations, the lasers interferometers' beams perfectly aligned to the mirrors surface normal, the mirrors' surfaces being ideally flat and the system without perpendicularity errors.

Consequently, the measurement model can be rewritten in the following simpler form:

$$\begin{cases} x_l \approx d_{x,l} + \delta\omega_x + \varepsilon_{x-r} + \varepsilon_{x-s} \\ y_l \approx d_{y,l} + \delta\omega_y + \varepsilon_{y-r} + \varepsilon_{y-s} \\ z_l \approx d_{z,l} + \delta\omega_z + \varepsilon_{z-r} + \varepsilon_{z-s} \end{cases} . \qquad 2.12$$

The perfect geometry–perfect motion simulation results are in agreement with the set of equations 2.12 and only the interferometric contributions are propagated through.

The perfect geometry–imperfect motion case accounts only for the stage angular degrees of freedom. The mathematical model is for this case is given by the following set of equations:

$$\begin{cases} x_l \approx d_{x,l} - p_{xy}\gamma_{0,l} + p_{xz}\beta_{0,l} \\ y_l \approx d_{y,l} + p_{yx}\gamma_{0,l} - p_{yz}\alpha_{0,l} \\ z_l \approx d_{z,l} - p_{zx}\beta_{0,l} + p_{zy}\alpha_{0,l} \end{cases} . \qquad 2.13$$

These equations show that the stage rotation effects the measurements only if the interferometers' beams are not aligned to the point of contact between the probe and the sample surface. This means that there are only second order effects on the target estimates if there are no Abbe offsets ($p_{jl} = 0$ with $j \neq l$).

The z standard uncertainty, $u(z)$, is very small compared to the x and y standard uncertainties, $u(x)$ and $u(y)$. This is explained by the difference in magnitude between the z interferometer's Abbe offsets and the x and y interferometers' Abbe offsets.

The imperfect geometry–perfect motion case accounts for the combined effect of laser position and laser orientation. The mathematical model is given by the following set of equations:

$$\begin{cases} x_l \approx d_{x,l}\left(1-\dfrac{\beta_x^2+\gamma_x^2}{2}\right)-\Delta p_{xx} \\ y_l \approx d_{y,l}\left(1-\dfrac{\alpha_y^2+\gamma_y^2}{2}\right)-\Delta p_{yy} \\ z_l \approx d_{z,l}\left(1-\dfrac{\beta_z^2+\alpha_z^2}{2}\right)-\Delta p_{zz} \end{cases} . \qquad 2.14$$

The standard uncertainties would be small in this situation because the variations associated with the influence quantities are small. For example, small Abbe and cosine offsets are matched by the sub-arc-second perpendicularity of pairs of axes. If the uncertainties associated with the laser alignment are increased by a factor of ten, the uncertainties associated with the x and y co-ordinate estimates increase from approximately 2.4 nm to 35 nm.

The mirrors' geometry mathematical model is given by the following set of equations:

$$\begin{cases} x_l \approx \Delta h_x \\ y_l \approx \Delta h_y \\ z_l \approx \Delta h_z \end{cases} . \qquad 2.15$$

The effect of the mirror surface flatness (Δh) is estimated during the dynamic tests and is given by the standard deviation of the measurement noise. The dynamic noise accounts for the combined effect of the air turbulence, interferometer noise and the mirrors' surface non-uniformity. 7 nm standard deviation for the x and y interferometers and 1.5 nm standard deviation for the z interferometer were measured.

The last case shows that the combined effect of all input parameters to the point co-ordinate uncertainty is similar to the mirror geometry case. The maximum difference between the standard uncertainties calculated for these two cases is less than 10 %. Furthermore, the intrinsic properties of the interferometers do not contribute significantly to the uncertainties associated with the point co-ordinate measured by the instrument.

2.8 Summary

In this chapter, the NPL Areal Instrument is described in detail and the uncertainty associated with the NPL Areal Instrument's co-ordinate measurements is calculated. The instrument is a stylus-type instrument that is capable of probing the surface of a sample with a nominal contact force of 0.75 mN throughout the instrument's nominal vertical range of 0.1 mm and nominal horizontal range of 8 mm × 8 mm.

A measurement model was developed that takes into account all the instrument error sources: the perpendicularity of pairs of axes, the reflecting mirror flatness, the interferometers' orientation, Abbe offsets, dead-path effects, thermo-mechanic effects, laser intrinsic error sources and the imperfect motion of the coplanar air-bearing stage. The method of choice for calculating the uncertainties associated with the instrument point co-ordinate measurement was a Monte Carlo method.

It was proven that the NPL Areal Instrument is capable of measuring the relative position of a point on a surface with nanometre-scale uncertainties. The standard uncertainty associated with the distance measurement in the x and y direction is 8 nm, whereas the standard uncertainty in the z direction was found to be 2.4 nm. The measurement noise contribution to the uncertainty has a larger effect than the rest of the contributions combined, thus the measurement noise is the limiting factor for achieving better uncertainties associated with the instrument point co-ordinate measurement. The intrinsic properties of the interferometers do not contribute significantly to the uncertainties associated with the point co-ordinate measured by the instrument.

3 Material measures

Material measures is defined in VIM (BIPM 2008c – 3.6) as:

"measuring instrument reproducing or supplying, in a permanent manner during its use, quantities of one or more given kinds, each with an assigned quantity value".

Note 2 attached to the above definition:

"A material measure can be a measurement standard."

The definition of the measurement standard, also called an etalon (BIPM 2008c – 5.1), is:

"realization of the definition of a given quantity, with stated quantity value and associated measurement uncertainty, used as a reference".

There is a third definition that is relevant to the use of the material measures presented in this chapter, namely reference measurement standard or reference standard (BIPM 2008c – 5.6):

"measurement standard designated for the calibration of other measurement standards for quantities of a given kind in a given organization or at a given location".

In the field of surface texture, alternative terminology is used for material measures such as artefacts, measurement standard, standard artefact and more recently physical measurement standard (ISO/FDIS 25178-70 2012). Perhaps the alternative terminology is used for different reasons: one reason could be the need of using one word for expressing complex meaning; another reason could be the lack of guidelines of using the metrological terms defined in VIM (BIPM 2008c); or a combination of both. It could also be that the word *etalon* is not likely to be used in English technical writing; instead *measurement standard,* which can often be confusing because standard also means a specification, technical recommendation, or similar normative document (see BIPM 2008c – 5.1 Note 8). The use of the term measurement standard implies that the material measure carries a traceable value that is inferred during its calibration.

In the early days, the calibration of the surface texture measuring instruments was performed using a line width type of measurement standard (Timms 1946, Underwood 1953, Schobinger 1956, Sharman 1967) and step height type of measurement standard (Reason 1967). Alternative suggestions were also investigated, such as vibrating platforms that were designed to test the instrument response for different spatial frequencies (Van Hasselt and Bruin 1963, Bendeli 1974). As more accurate measurements were required, interferometric techniques were employed to measure step-heights, but it soon was realised that the measurement technique is not the limiting factor but the sample geometry (Teague 1978). The random type (type D see next section) measurement standards were discussed by Song (1988) , who consequently produced a range of uni-directional random material measures.

As the performance of the measurement instrumentation increased, it became difficult to produce suitable material measures and X-ray interferometry was suggested as an alternative (Whitehouse 1988, Chetwynd *et al.* 1983), as well as material measures that use fullerenes (Griffith and Grigg 1993), square wave gratings using silicone technology (Scheer and Stover 1998) and multiple delta–layer films (Kim *et al.* 2007).

3.1 Previous NPL research work

One deliverable of this PhD project is to produce and characterise a series of areal material measures that are compliant with ISO 25178. This is a follow up of earlier research work carried out at NPL, which is briefly presented in this section.

Previous to 2008, NPL was involved in two research projects aimed to develop surface texture material measures. The first project was the EU-funded CALISURF project with the objective of producing material measures and procedures to calibrate surface topography measuring instruments (Trumpold and Frenzel 2000). CALISURF investigated different manufacturing and replicating techniques of material measures such as: holographic interferometry (Leach *et al.* 2001), ultra-precision diamond machining, injection moulding of plastic copies and electro-formed nickel replicas. The results showed that holographic interferometry could produce and replicate only type C1 (see paragraph 3.3) material measures down to PSm = 0.8 µm, whereas diamond machining was limited to PSm = 25 µm. Diamond machining could produce type C2 (see paragraph 3.3) material measures down to PSm = 15 µm (Trumpold and Frenzel 2000).

The injection moulding and nickel electro-forming were used only for replication. The plastic replicas proved to be very inexpensive and highly reproducible but unfortunately very easy to damage by the contact stylus instruments. The quality of the plastic and nickel replica depended on the cleanness of the manufacturing environment. The project concluded that the sinusoidal material measures were well suited for dynamic calibration of surface measuring instruments in all three orthogonal directions and were used for calibrating other instrument properties (properties of the probing system, guiding deviations, influences of the traversing speed, discrimination length, properties of the applied electrical filters and algorithms for calculating surface texture parameters).

In the 2002 to 2008 NMS Length Programme, NPL led a project that aimed to produce material measures for performance verification of contacting and non-contacting (optical) surface texture measuring instruments (Haycocks *et al.* 2005a,b). The material measures had to be suitable for profile and areal surface texture measuring instruments. The material measures were produced using a range of manufacturing methods, such as optical lithography on glass and silicon, electron beam lithography in silicon, diamond turning in copper followed by replication in nickel. The manufactured material measures were designed to test the surface texture measuring instruments' vertical scale, lateral scale, resolution, dynamic response and probe condition. Type ACG material measures were produced for the calibration of the lateral scale XY grid patterns (chrome on glass). Step heights ranging from 10 nm to 50 µm were manufactured to test the z axis. The step heights up to 1 µm inclusive were produced in glass and silicon. The steps taller than 1 µm were produced by diamond turning in copper and then nickel replication. The silicon steps were manufactured together with waffle step height patterns, or type ACG standards, with various periods that allowed for verification of *z* axis scale over the field of view. Diamond turning in copper and nickel replication methods were used to produce sine wave profiles for testing the dynamic response. The resolution material measures were manufactured by electron beam lithography on silicon and consisted of grating patterns, of equal mark/space ratio at various pitches, and a star pattern. The star pattern provided a continuum of effective pitch values.

3.2 Commercially available material measures

The stylus instrument manufacturers are able to provide a wide range of material measures. For example Taylor-Hobson include in their list of accessories a measurement standard that brings together a depth measurement standard and a roughness measurement standard. They also commercialise profile coordinate measurement standard in a form of a hemisphere (http://www.taylor-hobson.com). Mahr sells spacing measuring standards, depth measuring standards, both types of roughness measurement standards and a coordinate measuring standard (http://www.mahr.com). Among their products Mitutoyo provides depth measurement standards and roughness measurement standards (http://www.mitutoyo.co.uk). QPT has available a unidirectional irregular profile roughness measurement standard (http://www.qpt.de/pdf/en/master.pdf).

A few independent manufactures commercialise only material measures. One of these companies is Rubert and Co. that is specialised in material measures produced by electroforming. They manufacture almost all types of ISO 5436-1 (2000) material measures, except the profile coordinate measurement standards (http://www.rubert.co.uk). SIMetricS in Germany produces a depth measuring standard (http://www.simetrics.de) and a spacing measuring standard (http://www.simetrics.de) that has been developed at PTB in collaboration with TU Chemnitz (Krüger-Sehm *et al.* 2004). These companies also produce a series of material measures according to ISO/DIS 25178-701 (2012) such as the contour profile developed at PTB (Neugebauer and Neuschafer-Rube 2005) and various crossed grating material measures designed to test and calibrate the lateral scales. More recently Frühauf *et al.* (2012) developed a roughness standard for 3D measurements that uses a lapping technique.

In the US, VSLI Standards Inc. markets a series of spacing standards and and depth standards (http://www.vlsistandards.com). Geller MicroÅnalyti-cal Laboratory Inc. manufactures a series of material measures called generically magnification reference standards (MRS) (http://www.gellermicro.com), that have groups of nested squares with various pitches.

The cross gratings and other lateral scale testing material measures are also available as accessories from the majority of the 3D instrument manufacturers. Taylor Hobson and Alicona provide specialised material measures for testing and calibrating the lateral scale for their range of optical surface texture measuring instruments.

PTB has available material measures for calibration of the vertical and horizontal measurement system of contact stylus instruments and for testing of the transfer behaviour of surface measuring instruments (http://www.ptb.de/en/org/5/51/514/entnormale.htm). PTB has also an online review of material measures used for dimensional measurement of microstructures (http://www.ptb.de/de/org/5/51/511/doc/calibration_artefacts.pdf). A second online list of material measures used for calibrating scanning probe microscopes and optical instruments can be found at (http://www.nanoscale.de/standards.htm). Ritter *et al.* (2007) has developed a land mark calibration standard to compliment the list of standards readily available for the calibration of scanning probes microscopes (Koenders *et al.* 2005), and Krüger-Sehm *et al.* (2007) produced an artefact for testing the lateral resolution of the instruments.

NIST is also commercialising a series of material measures called SRM that are used to calibrate scanning electron microscopes that could be of interest. Especially the SRM 8090 is a material measure that could be used for assessing surface texture instruments (see http://www.nist.gov). The SRM 8090 consists of silicon wafer with features of various sizes that mimic electronic components used in the semiconductor industry. Also SRM 8820 (recently released) could be used to calibrate the scales of the instruments (Postek *et al.* 2010).

It is also worth mentioning here that there are plenty of other companies that produce material measures for nanotechnology such as waffle plates, sinusoids and so on. The characteristics of these material measures are not necessarily suited for far-field measuring instruments as they are designed for SPM characterisation. Instead they could be used for testing the limits of far-field instruments.

3.3 Profile material measure standards

Currently there are international specification standards covering 2D or profile measurement of surface texture and a limited number for areal measurement. The profile measurement standards are part of the Geometrical Product Specification (GPS) system and they cover all aspects of the profile measurement process, from nominal characteristics of contact (stylus) instruments to profile parameters that are used to quantitatively characterise a surface.

This section considers only ISO 5436 part 1 (2000) that defines the material measures used to characterise profile measuring instruments as defined in ISO 3274 (1998). The latter standard describes the nominal characteristics of contact (stylus) instruments, thus the profile material measures are defined and designed for stylus instruments only.

ISO 5436 part 1 (2000) defines five material measures, types A to E, each of which may have a number of variants. Each one of these material measures reproduces the value or values of a limited number of quantities and so they are able to test various instrument characteristics.

Type A material measures are also called depth measurement standards and are used to calibrate the vertical characteristics of the stylus instrument. Type A material measures have a wide groove or grooves of known depths that are wide enough to be insensitive to the shape or condition of the stylus tip. There are two variants of these types of material measures. The groove of the first variant (type A1) has a flat bottom (figure 3.1), whereas that of the second variant (type A2) has a rounded bottom (figure 3.2).

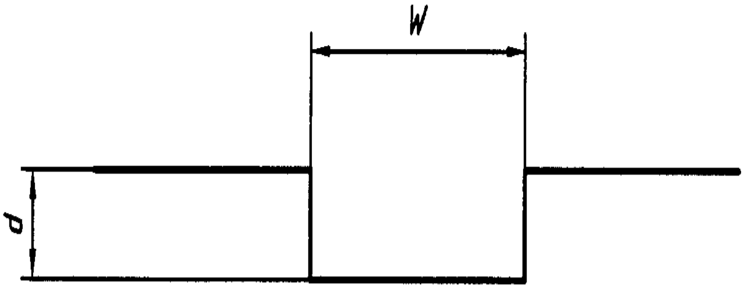

Figure 3.1 Type A1 material measure standard, from ISO 5436 1: 2000

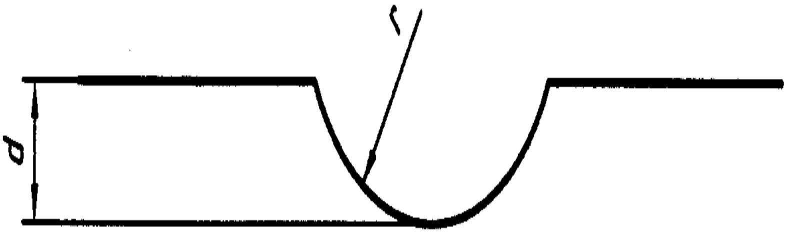

Figure 3.2 Type A2 material measure, from ISO 5436-1: 2000

Type B material measures, referred to as tip condition measurement standards, are used mainly to calibrate the condition of the stylus tip. Type B material measures have narrow grooves of various depths and widths or they can have a sharp protruding edge. There are three variants of type B material measures. Type B1 material measures have a narrow groove with a rounded bottom or a number of separated grooves with rounded bottoms proportioned to be increasingly sensitive to the dimensions of the stylus tip. Type B2 material measures have two groove patterns of nominally equal *Ra* values (ISO 4287 2000), one being sensitive (isosceles triangular grooves with sharp peaks and valleys - figure 3.3) and the other one insensitive (sinusoidal figure 3.4 or arcuate grooves - figure 3.5) to the dimension of the stylus tip. Type B3 material measures have a fine protruding edge with a radius smaller that the stylus tip radius (figure 3.6).

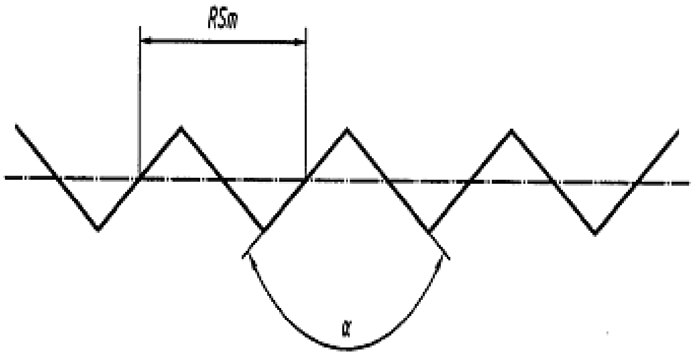

Figure 3.3 Type B2 and type C2 material measure, from ISO 5436-1: 2000

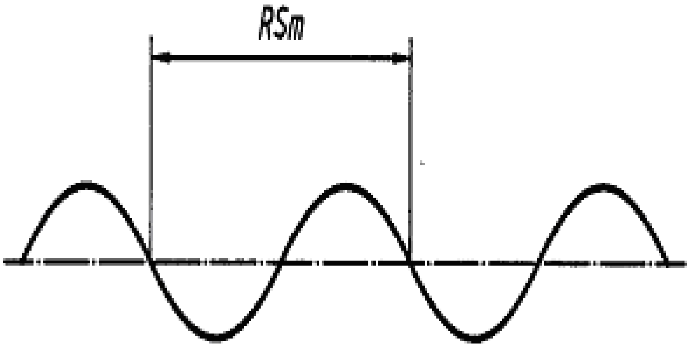

Figure 3.4 Type B2 and type C1 material measure, from ISO 5436-1: 2000

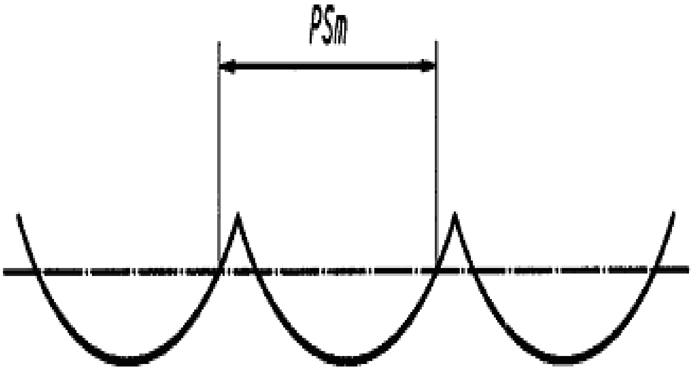

Figure 3.5 Type B2 and type C4 material measure, from ISO 5436-1: 2000

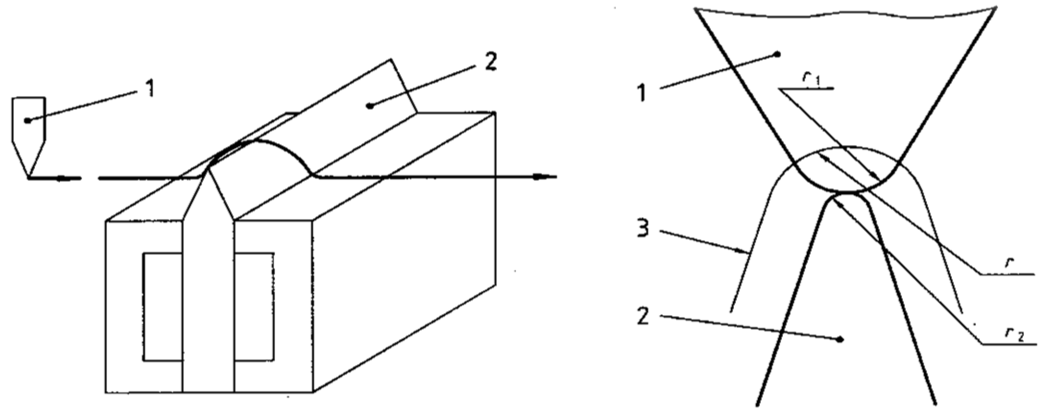

Schematic diagram of razor blade trace for profiling the shape of a stylus tip to determine its radius

The output profile essentially represents the stylus tip shape if the radius and apex angle of the razor blade are much finer

Key
1 Stylus
2 Razor blade
3 Recorded profile

Figure 3.6 Type B3 material measure, from ISO 5436-1: 2000

Type C material measures, referred to as spacing measurement standards, are used primarily to calibrate the vertical profile components, but in certain circumstances they can be used to calibrate the horizontal profile components (the instrument scale along the scanning axis). Type C material measures have a grid of repetitive grooves. There are four variants of these types of material measures. Type C1 material measures have sine waves profile grooves (figure 3.4), type C2 have isosceles triangular profile grooves (figure 3.3), type C3 have simulated sine wave grooves (triangular profile with rounded or truncated peaks and valleys - figure 3.7) and type C4 have arcuate profile grooves (figure 3.5).

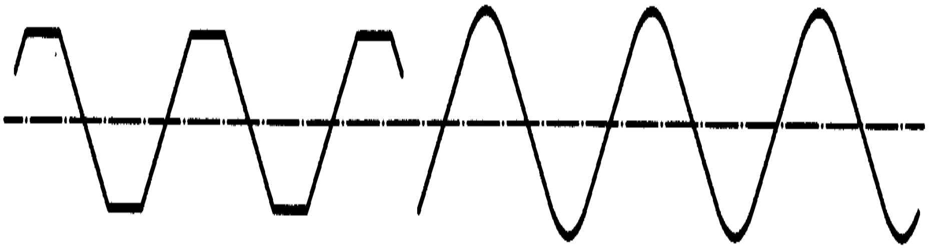

Figure 3.7 Two forms of type C3 material measures standards, from ISO 5436-1: 2000

Type D material measures, referred to as roughness measurement standards, are used to check the overall calibration of the instrument, *i.e.* the instrument's ability to measure and calculate a surface texture parameter. Type D material measures have irregular profile grooves and there are two variants of these types of material measures. Type D1 material measures have unidirectional irregular profiles (figure 3.8) and type D2 material measures have circular irregular profiles (figure 3.9).

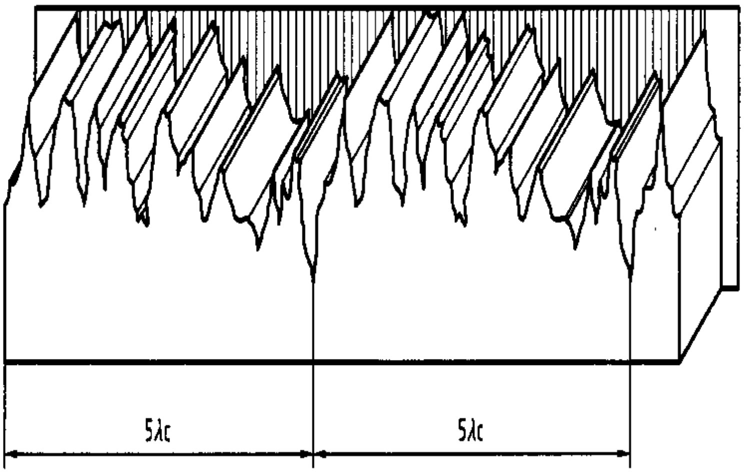

Figure 3.8 Type D1 material measure, from ISO 5436-1: 2000

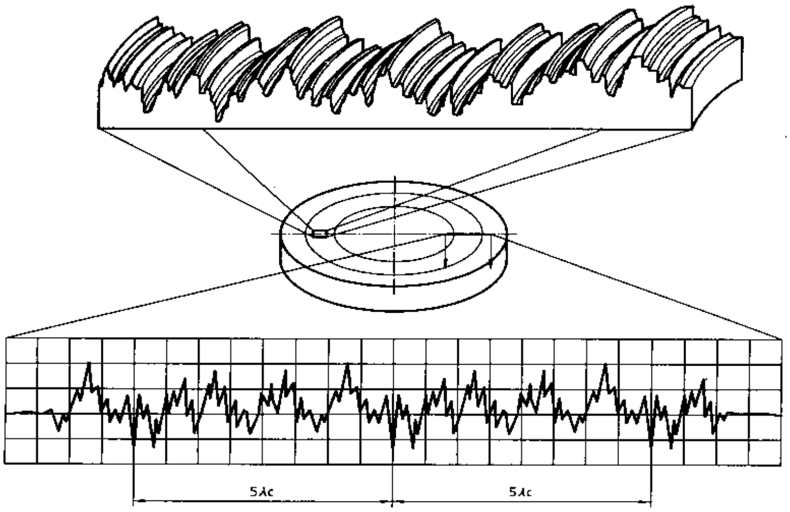

Figure 3.9 Type D2 material measure, from ISO 5436-1: 2000

Type E material measures, referred to as profile coordinate measurement standards, are used for checking the profile coordinate system of the instrument. The type E material measures have basic geometric shapes and there are two variants of this type of artefact. Type E1 material measures consist of a sphere or a hemisphere whereas type E2 are a prism with a trapezium cross-section (figure 3.10).

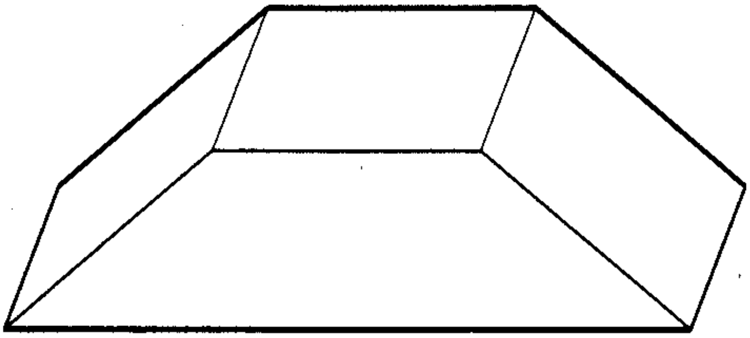

Figure 3.10 Type E2 material measure, from ISO 5436-1: 2000

The profile material measures should be chosen according to the instrument characteristics and to the surface to be investigated. For additional information about the practical application of ISO 5436 part 1 (2000) see the NPL good practice guide on the measurement of surface texture using stylus instruments (Leach 2001).

3.4 Areal material measures

ISO/DIS 25178-70 (2012) defines material measures used as measurement standards to calibrate areal topography measuring instrumentation. The approach chosen in ISO/DIS 25178-70 is to combine the profile material measures described in ISO 5436- 1 (2000) and the newer material measures that can be used to calibrate areal surface topography measuring instruments. Eventually, part 70 will supersede ISO 5436 part 1. A minor inconvenience is that some of the areal and profile material measures are known under different names (Leach 2009). In ISO/DIS 25178-70 the material measures are separated in to two main types: unidimensional (profile) and bidimensional (areal). Table 3.1 presents the profile material measures including their new and old terminology and table 3.2 presents the areal material measures.

Table 3.1 Types of unidimensional (profile) material measures

Areal Type (ISO/DIS25178-70)	Previously known types	Name
PPS	[1]C1 and B2	Periodic sinusoidal shape
PPR	[1]C2 and B2	Periodic triangular shape
PGR	-	Periodic rectangular shape
PRO	[1]B2 and C4	Periodic arcuate shape
PRI	[1]A1	Groove, rectangular
PAS	[1]A2	Groove, circular
PDG	[1]D1	Roughness profile
PPS	[1]D2	Circular roughness profile
PPR	[1]E2	Prism
PGR	[1]B3	Razor blade
PRO	[1]C3	Approximated sinusoidal shape
PRI	CS	Contour standard
PAS	ER1	Double groove

[1] ISO 5436: 1 types

Type PAS, AGP and AGC material measures are used to calibrate the vertical and horizontal amplification coefficients of the measuring instrument, thus, the instrument *x*, *y* and *z* scale. The type PAS, AGP and AGC material measures have a triangular profile groove with a slightly rounded tip. Type PAS have only two parallel grooves (figure 3.11). Type AGP have four grooves forming a rectangle (figure 3.12). Type AGC: circular groove standards have a circular groove (figure 3.13). Type AGP and type AGC are also used to calibrate the squareness of the *x* and *y* axes.

Table 3.2 Type of bidimensional (areal) material measures

Areal Type (ISO/FDIS 25178: 70)	Previously known types	Name
AGP	ER2	Grooves – perpendicular
AGC	ER3	Groove – circular
ASP	[1]E1	Sphere
APS	ES	Plane – sphere
ACG	CG1 and CG2	Cross grating
ACS	-	Cross sinusoidal
ARS	-	Radial sinusoidal
ASG	-	Star-shape grooves
ADT	-	Irregular

[1]ISO5436: 1 types

Type APS material measures, referred to as sphere/plane measurement standards, are used to calibrate multiple parameters such as the vertical and horizontal scale, orthogonality of the *x* and *y* axes, the response curve of the probing system, the stylus geometry (applicable for pivoting types of stylus), the stylus tip radius and cone angle. Type APS material measures are composed of a part of a sphere and a plane (figure 3.14). This material measure does not have variants.

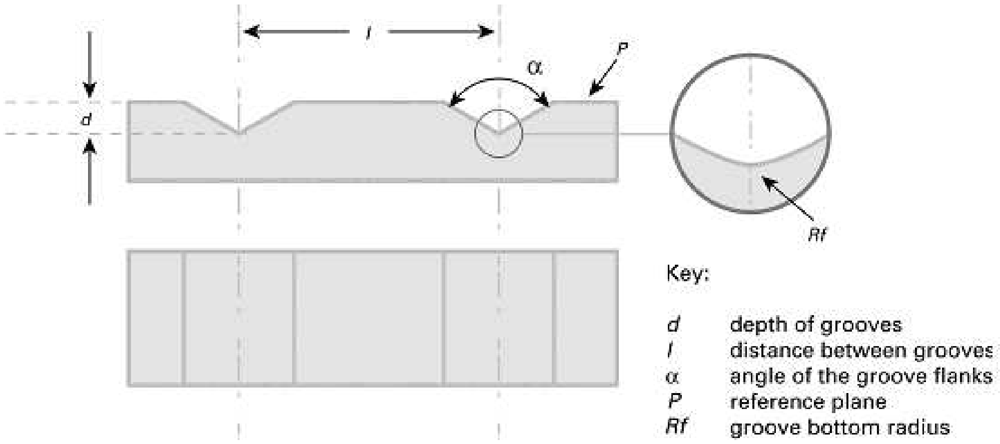

Figure 3.11 Type PAS material measure

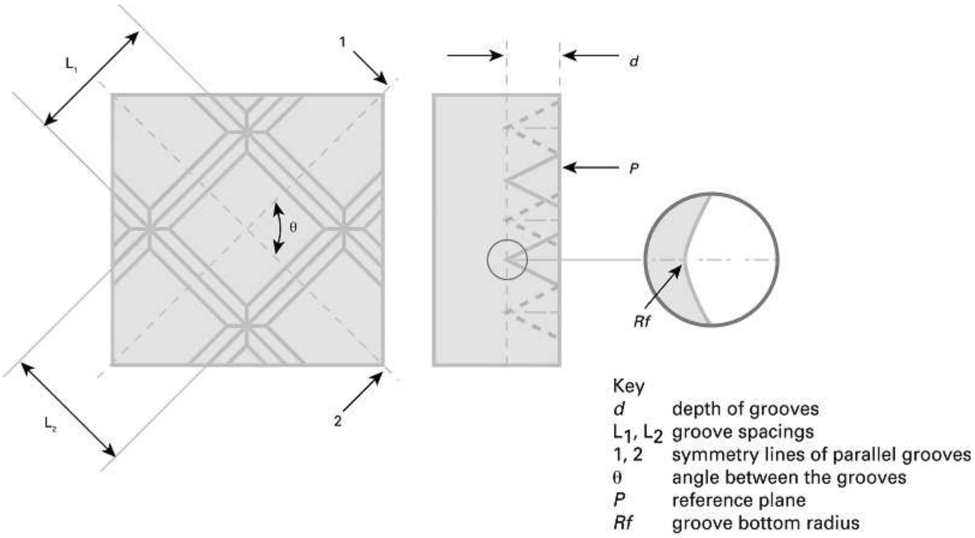

Figure 3.12 Type AGP material measure

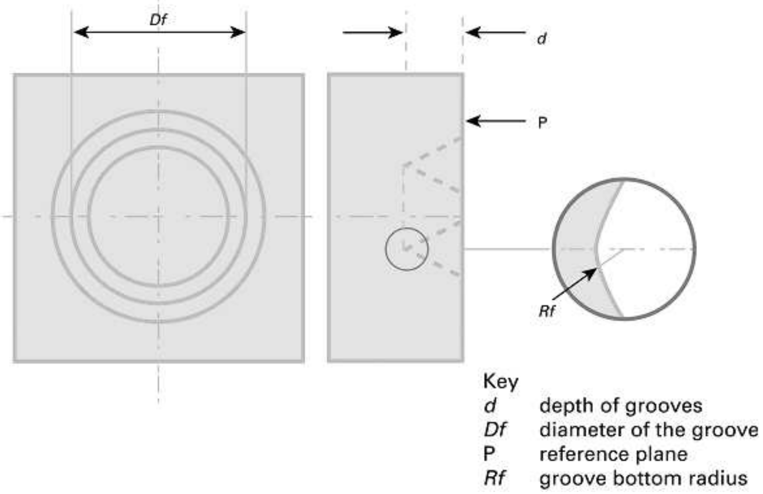

Figure 3.13 Type AGC material measure

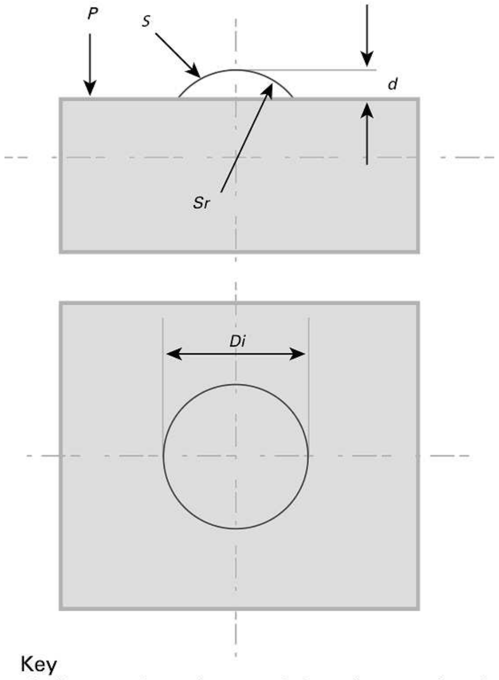

Key

d	distance from the top of the sphere to the plane P
S	part of a sphere
Sr	radius of the sphere
Di	intersection diameter

Figure 3.14 Type APS material measure

Type PRI material measures, referred to as contour standards, are used for overall calibration along one lateral axis of the instrument. Type PRI material measures (figure 3.15) are composed of at least two arcs of a circle (one concave, one convex) and two wedges/triangles (one concave, one convex). There are no variants of this type material measure.

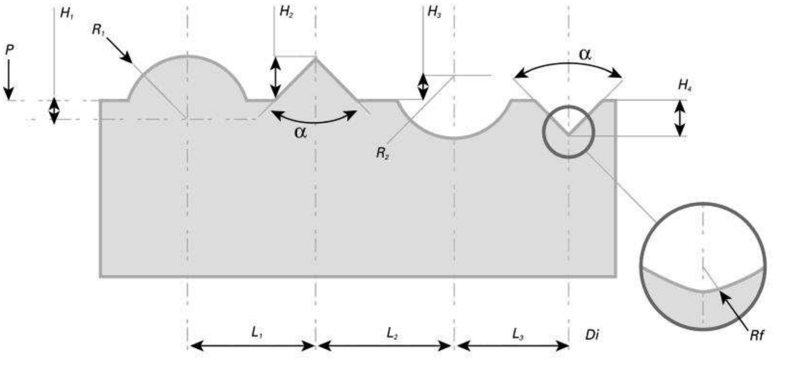

Key

Ri	radius of the arcs of circles
α	angle of the triangles
P	datum plane
$L1,\dots,Ln$	distances between the different patterns
$H1,\dots,Hn$	heights between the different patterns with respect to the datum plane P

Figure 3.15 Type PRI material measure

Type ACG material measures, referred to as cross grating standards, are used to calibrate the amplification coefficients along the instrument axes and the orthogonality of the *x* and *y* axes. There are two variants of this type of the material measure. Old type CG1: X/Y cross grating material measures have a 2D array of raised lines, grooves or dots, and are used to calibrate only the horizontal amplification coefficients and the orthogonality of the *x* and *y* axes (figure 3.16). Old type CG2: X/Y/Z cross grating standards are 2D pits with flat bottoms (waffle pattern). They can also be used to calibrate the vertical scale (figure 3.17).

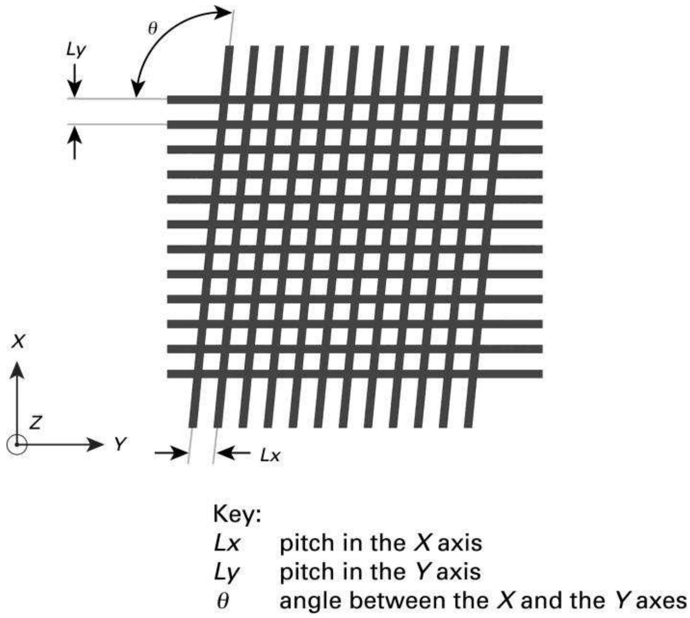

Figure 3.16 Type ACG (CG1) material measure

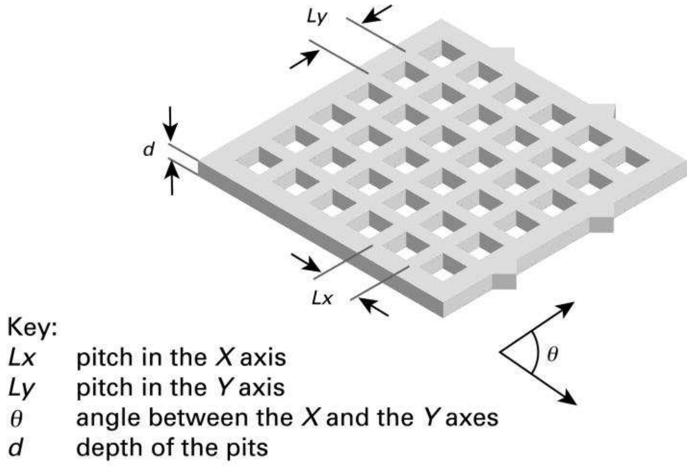

Figure 3.17 Type ACG (CG2) material measure

Type ADT material measures (Yanagi *et al.* 2007), referred to as irregular topography standards, are used for overall calibration of the measuring instrument. Type ADT irregular topography material measures have a minimum of two by two unit isotropic measuring areas (figure 3.18). The measuring area consists of a limited range of wavelength components. Surface texture parameters such as *Sa*, *Sq*, *Sz*, *Ssk* and *Sku* are evaluated with uncertainty.

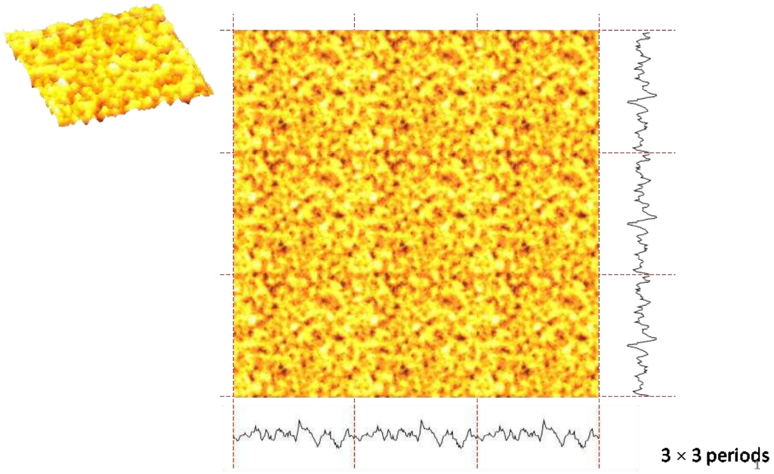

Figure 3.18 Type ADT material measure

Type ACS are composed of a sinusoidal wavelength along the *x* axis and a sinusoidal wavelength along *y* axis. Type ACS material measures can be used for overall calibration of the horizontal axis of the instrument and verification of the vertical axis. The measurands are the arithmetic mean height of the surface *Sa* and root mean height of the surface *Sq*, but the mean pitches along the *x* and *y* axes can also be used for calibration.

Type ASG, star shape grooves consists of a series of constant height grooves with triangular profiles in the *xy* plane (see chapter 7). Type ASG measures are used for verification of the instrument spatial height resolution (ISO/FDIS 25178 part 603 (2012)). The measurand is the depth as a function of pitch on a circular profile extracted concentric to the apex of the standard.

In some cases, the design of the material measure has to account for particularities of instruments. For example, focus variation instruments are incapable of measuring smooth surfaces (*Ra* or *Sa* below 10 nm) and specially designed material measures have to be used (Danzl 2008).

With the exception of types PDG, PPS and ADT, measurement standards are mainly used for the calibration of the instrument scales. However, not all of the material measures are always required because a large number of the profile material measures are designed for contact stylus instruments and other material measures can achieve the same measurement goal.

3.5 Current design

Although ISO/FDIS 25178-70 (2012) contains a large number of material measures, it does not mean that there is a need to use all of them to calibrate an instrument. The choice of material measures should be based on a small selection that is sufficient for a full geometrical calibration of the instrument. An example of such selection of material measures is a calibration set that is limited to flats, type ACG, type ASG and type ADT. These three types of material measures are used to calibrate the metrological characteristics of the instruments and they are the subjects of the NPL areal calibration box set that is presented next.

The type ACG is used to calibrate the linearity, amplification and squareness of the x, y and z scale. The design of the type ACG includes five cross gratings that have different pitch, ranging from 16 μm to 400 μm, which allow testing of the amplification, linearity and squareness of the x and y axes of the instrument (see figure 3.19) for different measurement windows (nesting indexes). The patterns were produced at different thickness: 0.5 μm, 1 μm and 2 μm.

The type ASG is used to calibrate the lateral resolution of the instruments. The NPL design of the resolution artefact is a combination of the type ASG and type ACG and they are manufactured in the same way to the ACG type that is used to calibrate linearity, amplification and squareness of the x and y scale presented above. The design of the resolution artefact includes thirteen ACG types with different pitches ranging from 600 nm to 20 µm and two ASG types of 70 µm and 20 µm radius.

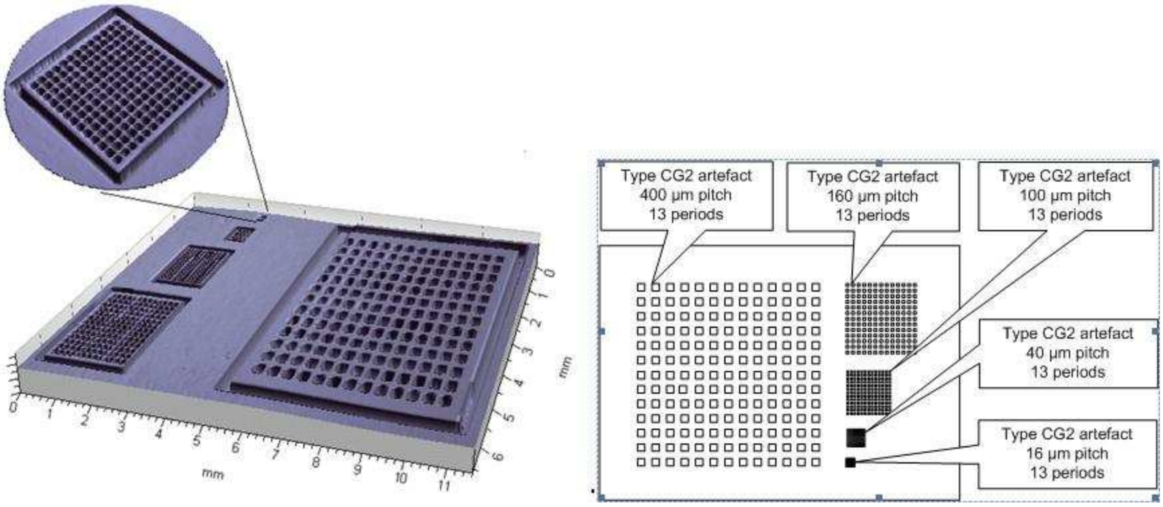

Figure 3.19 NPL ACG type of material measure: measured (left) and design (right)

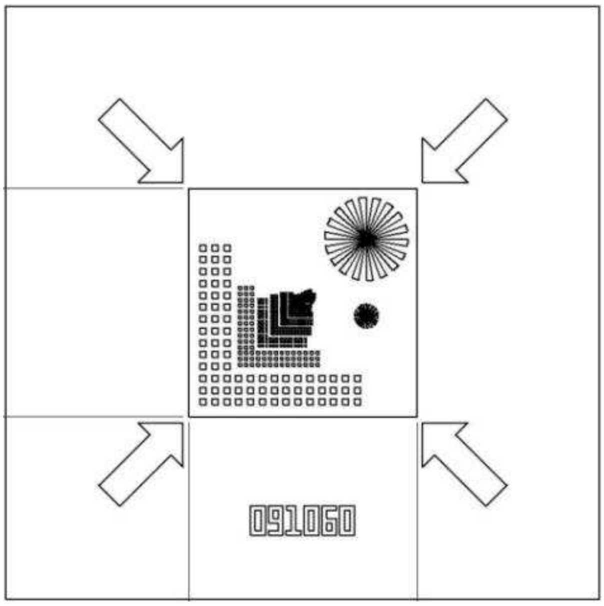

Figure 3.20 NPL resolution artefact

In the final form the type ACG and type ASG is an electroformed nickel replica of a master that was initially produced as a patterned photoresist film deposited on a silicon wafer. The manufacturing of the masters as thin nickel moulding tools was carried out in three main steps:

- Structuring the polymeric master structures with e-beam lithography.
- Metallization of the conductive plating base by plasma vapour deposition (PVD).
- Fabrication of the moulding tool using nickel electroforming.

Finally, the ADT type was produced by diamond turning (Nemoto *et al*. 2009, Yanagi *et al.* 2007) followed by Ni replication. The final material measures have a useful working areas of 1.5 mm by 1.5 mm (see figure 3.21).

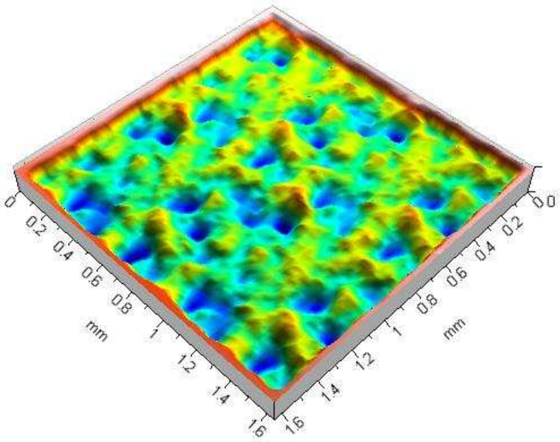

Figure 3.21 NPL ADT artefact

Final replication of all material measures was carried out with higher current density leading to faster deposition rates of nickel (see figure 3.22).

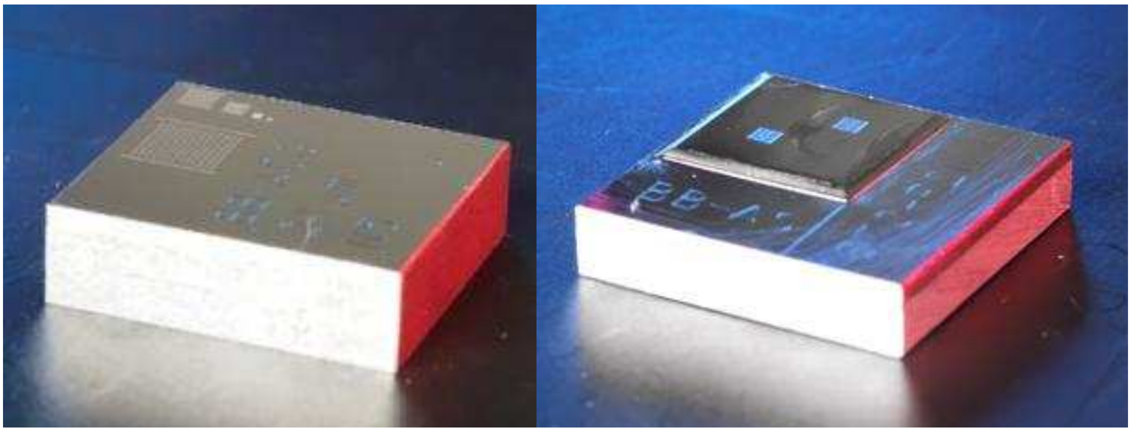

Figure 3.22 Final material measures produced in nickel: left - type ACG, right – type ADT

4 Instrumentation

To a certain extent, the majority of manufactured components need to have some control over the surface. The field of surface topography measurement was developed in order to address these issues and it initially begun by making use of the sight and touch senses (Saw 1936). The first instruments to measure surface texture were introduced in the early twentieth century. These instruments employed different measuring methods, some successful, some not, such as the profile contact stylus (Harrison 1931, Abbot *et al.* 1938), optical (Schmaltz 1929, Linnik 1930), pneumatics (Nicolau 1939, von Weingraber 1942, Whitehouse 1994) and capacitance methods (Perthen 1936, Whitehouse 1994).

In the late 1960s and towards the beginning of 1970s, areal surface topography measuring instruments emerged for the first time using optical probes (Linnik 1930, Tolansky 1960, Bennett 1976, Minsky 1988) and contact stylus probes (Williamson and Peklenik 1967-1968, Grieve *et al.* 1970). The first commercial contact stylus instrumentation became available twenty years later after the development of personal computers in the 1980s which could handle large amounts of data (Teague *et al.* 1982, De Chiffre and Nielsen 1987, Jiang et al 2007b). The digital era had a major impact in the proliferation of the profile parameters that were used to assess surfaces quantitatively. For the first time, computers also allowed for the surface visualisation to be at the fingertip of the operator. Advances made in digital filtration meant that the same instrument could measure profile, waviness and form. Since then the range of areal surface topography measuring instrumentation has expanded and matured (see for example Thomas 1999, Whitehouse 1994, Leach 2011).

When used for 3D characterisation of surface topography, stylus instruments were too slow (at a typical stylus scanning speed of 0.5 mm s^{-1} and 500 nm sampling spacing an area of 1 mm × 1 mm will be measured in more than an hour) and, due to their contacting nature, they were damaging the surfaces under investigation. Subsequently optical principles became a compelling alternative to stylus instruments. Since the 1980s, several instruments based on various focus detection techniques (Schmidt and Compton 1992) and interferometry (Bhushan *et al*. 1985, Greivenkamp and Bruning 1992, Caber 1993, Deck and de Grout 1994) have been successfully developed (see section 4.2 to 4.4). The non-contact nature of the optical methods allowed them to be used as fast investigation techniques, because the measurement speed was not any longer restricted by the potential damage that a contact probe could inflict on the sample. However, there are some disadvantages to surface topography measuring optical instruments. While it is relatively simple to predict the output of a contact stylus instrument as the movement of a ball rolling on the surface, the interpretation of the interaction between the electromagnetic field and the surface requires assumptions that are not easy to defend in practice (Coupland and Lobera 2008).

The list of measuring instruments presented in figure 4.1 is by no means comprehensive, but illustrates the commonly used investigation techniques for measuring roughness (Thomas 1999, Stout and Blunt 2000, Mainsah *et. al* 2001, Muralikrishnan and Raja 2009).

The 1980s are well known for the invention of the scanning tunnelling microscope (STM) by Binning and Rohrer (1983) and for the subsequent invention of the atomic force microscopes (AFM) by Binning *et. al* (1986). These two instruments revolutionised the area of surface metrology as they allowed for the first time quantitative measurement of areal surface topography at the nanometre and atomic scales. However STM and AFM are mostly used to measure a variety of physical and chemical properties of the surface.

The term roughness measuring instrument is often associated with the profile measuring techniques such that the terminology used in figure 4.1 can be confusing. In ISO 25178-6 (2010) the instruments are divided into three main types: line profiling that can be represented as $z = f(x)$; areal topography represented as $z = f(x, y)$; and area integrating that provides a numerical answer which depends on the area integrating properties of the surface (Leach 2011).

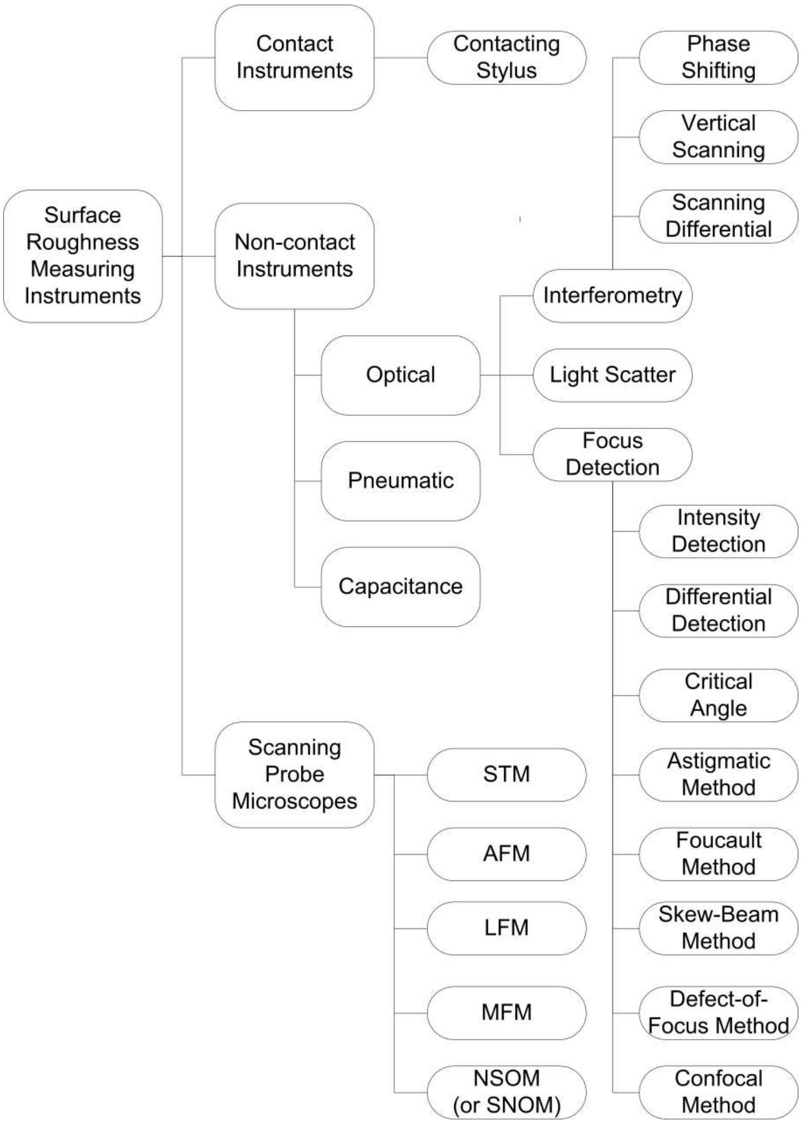

Figure 4.1 Roughness measuring instruments (LFM low force microscopy, MFM magnetic force microscopy, SNOM scanning near-field optical microscope)

Surface topography measuring instruments are able to measure surface features within a broad range of amplitudes and spatial wavelengths. The area of operation of the instruments is constrained by a number of factors such as range and resolution, the geometry of the contact stylus tip or the numerical aperture of an optical instrument, environmental conditions, *etc*. Stedman (1987a, b) was first to present diagrammatically amplitude wavelength (AW) space. AW space helps in the understanding of the operating regimes of surface measuring instruments (see figure 4.2).

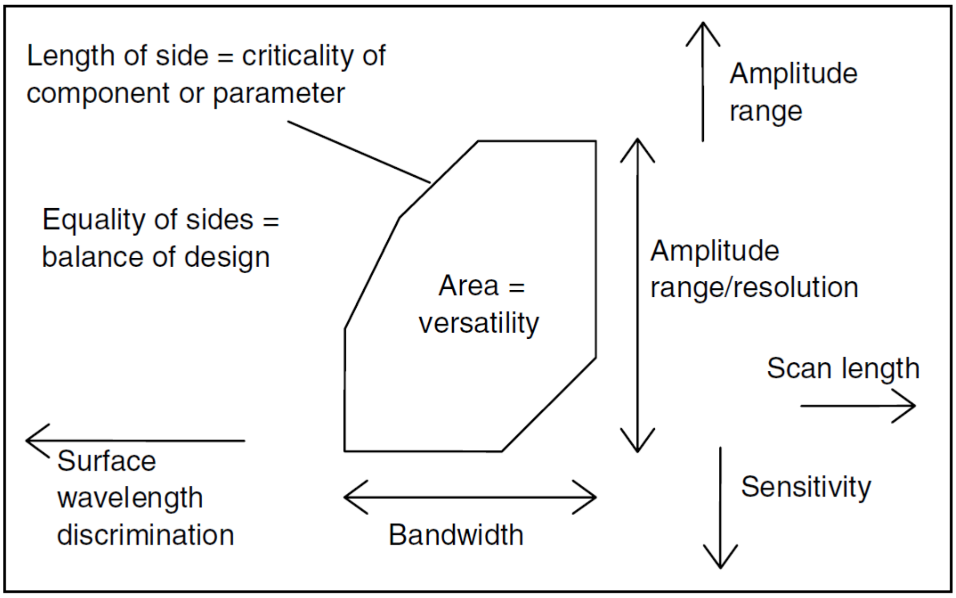

Figure 4.2 Typical constraints in additional AW space (adapted from Stedman 1987a)

There is a natural split at about 500 nm in the spatial wavelength range that divides the surface topography measuring instruments. At one end there are the stylus and far-field optical instruments that are capable of measuring spatial wavelengths larger that 500 nm. At the opposite end there are the scanning probes microscopes that measure 500 nm and smaller features. The 500 nm value does not represent a definite separation as the far-field optical instruments are diffraction limited at about 200 nm to 300 nm and the typical commercial AFMs scanning range goes above 30 µm.

Only the traceability of a limited number of areal surface topography measuring instruments is in scope of this thesis. Line profile traceability has already been demonstrated (Leach 2000) and the areal integrating instruments can be calibrated by direct comparison with a calibrated areal topography measuring instrument. The areal topography type of instruments includes a wide variety of instruments ranging from scanning probe microscopes (SPMs), such as AFMs, STMs, *etc.*, to optical instruments and contacting stylus instruments. Often SPMs have different traceability routes (Danzebrink *et al.* 2006, Yacoot and Koenders 2008), and a different standardisation framework (ISO/FDIS 11952 2012), than the optical and contacting stylus instruments, and they are not discussed here.

4.1 Contact stylus instruments

Instruments based on the contact stylus principle have been used to measure surface topography for one century (Evans and Bryan 1999). During this time, contact stylus instruments have had to adapt to many paradigm shifts that occurred in surface metrology (Jiang *et al.* 2007a b) and, as a result, they have matured into refined metrology tools. Whitehouse (1994) gives a comprehensive history of surface texture metrology in which the development of stylus instruments had an undeniable contribution.

Essentially, contact stylus instruments measure the vertical displacement of a fine stylus that is traversed across the surface of a component, working very much like a gramophone. While the contact stylus principle is simple to understand, the underlying metrology of the instrument has a high degree of complexity. Fortunately, these instruments have been described in great detail in the literature (Whitehouse 1994, Thomas 1999, Leach 2009). A schematic diagram of a typical stylus instrument is presented in figure 4.3.

Contact stylus instruments were used only in profile mode (2D) until the end of 1960s when in separate groups Williamson and Grieve (Williamson and Peklenik 1967-1968, Grieve *et al.* 1970) built the first research instruments that measured areal topography (3D). It took another two decades for their commercial counterparts to appear owing mainly to the advent of personal computers in the 1980s (Jiang et al 2007b). Areal contact stylus instruments generate a 3D image of the surface in a measurement coordinate system such as Cartesian, cylindrical or spherical.

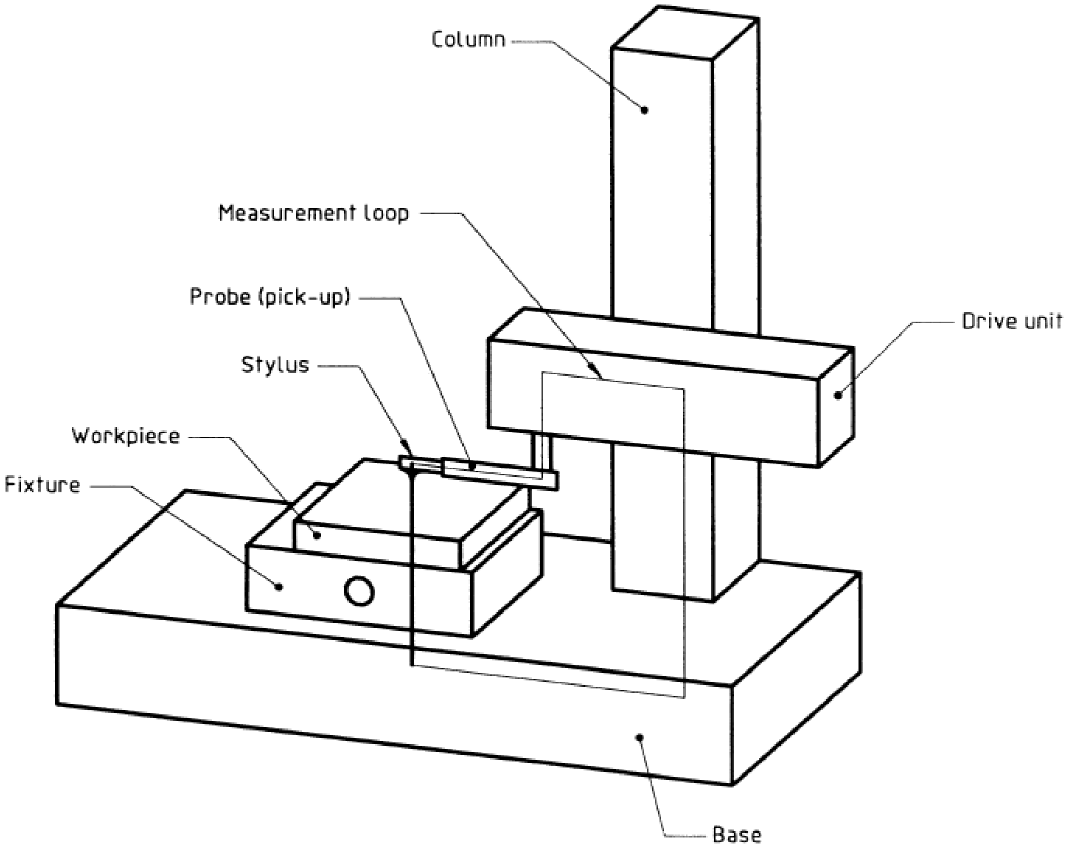

Figure 4.3 Example of a measurement loop of a stylus instrument taken from ISO 3274 (1997)

The Cartesian coordinate system is regularly used by areal topography measuring instruments. In this case the reference axis of the instrument is physically realised by a combination of reference guides, linear or areal guides, that allows the instrument's probing system (*i.e.* stylus) to move relative to the surface of a component along known paths (ISO 25178-601 2010). The device responsible for the relative movement of the probing system to the surface is called the driving unit. The driving unit includes location sensors that measure relative displacements along the reference guides. In many cases it is difficult to discern the driving unit from the reference guide(s) because they are part of an integrated system called the scanning system. Based on the configuration of scanning and probing systems, ISO 25178-601 (2010) Annex A identifies ten possible types of contact stylus instruments that measure areal topography.

The lateral scanning system of the stylus instruments can be based on a combination of two linear reference guides (x and y) or an areal reference guide. Because both the probe and/or the component can be driven laterally relative to each other with similar results, it is possible to have five lateral scanning system configurations: probing system moving along a linear reference guide and component moving along another linear reference guide ($PX\ o\ CY$), probing system moving along two linear reference guides ($PX\ o\ PY$), component moving along two linear reference guides ($CX\ o\ CY$), probing system moving across an areal reference guide (PXY) and component moving across an areal reference guide (CXY).

Largely, the probing system of stylus instruments is based on a design in which a sharp tip (typically conical shapes with a rounded tip of 2 μm radius) is situated at the end of an arm that pivots in a vertical plane around a fixed point. The arcuate motion of this system, called the stylus, could be corrected or not and that gives the two probing system variants: without arcuate error correction (A) and without arcuate motion or corrected arcuate error (S). The second variant of the probing system includes those instruments that are not based on a pivoting arm (for example, Leach 2000, Bayliss *et al.* 2006 and Thomsen-Schmidt and Krüger-Sehm 2008).

Common to all configurations of areal contact stylus instruments are the main error sources, *i.e.* the probing system and the mechanical structure of the instruments (Balsamo *et al.* 1996). Areal surface topography measuring instruments are essentially coordinate measuring machines (CMMs) and their performance is affected by a number of influence factors, such as the squareness of pairs of axes, alignment, imperfect motion (Cox *et al.* 1999) and the interaction between the probe and the component's surface. In consequence, it becomes appropriate to depict the effects of the stylus probe separately from the effects of the mechanical structure.

In the case of areal contact stylus instruments, the probe is identical to profile contact stylus instruments. The difference that sets these two types of instruments apart is the existence of a third axis that allows areal instruments to map the surface in 3D. A vast majority of commercial areal contact stylus instrument are profile instruments that have been upgraded to areal status by adding an additional *y* drive unit. It follows that all the problems encountered with contact stylus instruments that measure surface profile are applicable to those that measure areal topography. Note that unless air bearing stages are employed (see chapter 2) the quality of the *y* drive unit is often inferior to the *x* drive unit (see flatness deviation of the stylus instrument presented in chapter 5). The effects of stylus instruments on the measurement of surface topography have been thoroughly studied. This chapter considers the tactile and dynamic characteristics of the probe (Whitehouse 1994).

Prior to describing the probe effects, the configuration of the probing system as presented in ISO 25178 – 601 will be discussed. Figure 4.4 shows the most common configuration of contact stylus probe that consists of a tip and an arm. The standard also specifies that there are other possible designs of stylus probe that are based on flexures (Leach 2000) or linear probes (Bayliss *et al.* 2006 and Thomsen-Schmidt and Krüger-Sehm 2008). The length of the arm (L) gives the height range that can be covered by the instrument because the movement of the probe in the pivot (2) is restricted to a limited angular range. As the length of the arm is increased or decreased the *z* range becomes larger or smaller, respectively. The stylus is mounted at one end of the arm opposite to the pivot and its height (*H*) establishes the maximum amplitude of the features that can be measured. For example, it would not be possible to measure grooves that have a depth larger than the height of the stylus. In figure 4.4 the stylus terminates in a conical shape with a rounded tip with typical radii ranging from 0.1 µm to 10 µm. In reality, the styli have pyramidal or conical shapes terminating with a truncated flat tip or a round tip, respectively. Depending on the usage, these two types of styli gradually attain similar shapes as the pyramidal tip develops rounded edges and the round tip becomes flatter.

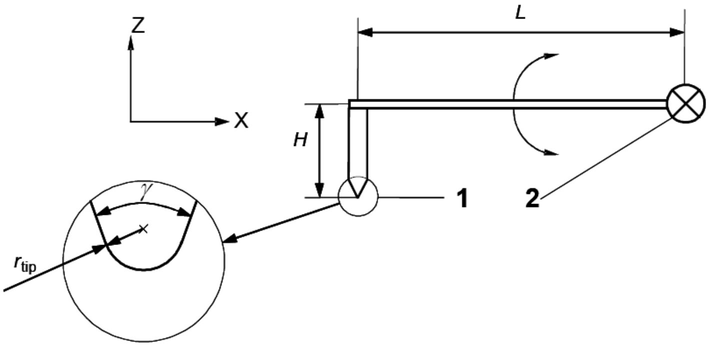

Figure 4.4 Typical stylus as in ISO 25178-601, where: 1 is stylus, 2 is pivot, *L* is length of the arm, *H* is height of the stylus, r_{tip} is radius of the tip and γ is cone angle of the tip

As the component is moved under the stylus, the stylus instrument acquires data that is a combination of the real surface of the component and the stylus shape (McCool 1984, O'Donnell 1993, Whitehouse 1994, Dagnall 1998). For instance, when the tip of the stylus crosses a sharp peak, the point of contact shifts from one side of the stylus to the other without breaking the contact with the highest point of the peak in such a way that a round stylus tip will make the summits appear gentler than they really are. This effect of the stylus geometry will not alter the peak height from the mean line but it will make the peak look wider. In contrast, valleys will appear narrower because the stylus will start to go up at the first contact with the ascending wall with immediate loss of contact between the trailing side of the tip and the descending wall. Another consequence of this effect is that the stylus will not penetrate the bottom of narrow valleys so the trace will look shallower. Moreover, if the tip size is larger than the distance between the surface features, the instrument will not record them. The effects of the stylus tip on the measurement results, also known as the instrument transfer function, has been investigated using various algorithms that accounted for stylus geometry and surface characteristics (Whitehouse 1979, O'Donnell 1993, Mendeleyev 1997, Wu 1999 & 2000, Yoshida and Tsukada 2006, Tian et al 2007, Lee and Cho 2012) and experimentally by (Bennett and Dancy 1981, Song and Vorburger 1991). All the models predict only the contact effect of the stylus tip and the surface features, and by no means do they predict the true surface topography. Ultimately the measured topography data is just an estimation of the surface topography that lacks information about surface areas that are not contacted by the stylus tip. Such areas include undercuts, overhangs and re-entrant angles where the stylus tip loses partial contact with the profile and so does not record these surface characteristics, or narrow valleys where the tip cannot penetrate to the bottom. Similar to the effect of re-entrant angles, surface features that have steeper angles than the half angle of the side of the tip are not contacted by the stylus tip.

Another aspect of the contact stylus instruments is the finite force that should to be exerted by the tip onto the surface to maintain permanent contact during the measurement. The pressure generated by the stylus tip could easily exceed the surface yield stress of the component which will lead to surface damage. Examples of damage produced by the stylus tip are uniform width scars (see figure 4.5) developed during the normal traverse (McCool 1984), shock marks when the stylus vibrates during the transverse and makes a variable width trace, and 'touch-down' mark damage (see figure 4.6), which look like craters in the surface (Bennett and Dancy 1981). It has been shown that the pressure generated by a force of 0.7 mN applied on an effective area of a typical 2 μm radius tip should not exceed the surface yield stress for most materials except some soft coatings (Whitehouse 1994). Even if the tip indents the surface and this method becomes a destructive technique, the results should be acceptable providing that the damage is small compared to the surface texture. As an example, the stylus marks are acceptable in an average machine shop but they could become undesirable when ultra-fine surfaces are investigated. Secondary to the surface damage (plastic deformation), the stylus produces elastic deformations of the surface. The elastic effects can be estimated quantitatively for homogeneous materials and for stylus constant pressure (Walton 1961). However, the surface of a component could change its elastic properties along the scanned area and the homogeneity assumptions no longer hold. The pressure exerted by the stylus could also change due to variation in contact area that depends on the local surface roughness. These effects could allow for various local elastic deformations that can result into measurement errors.

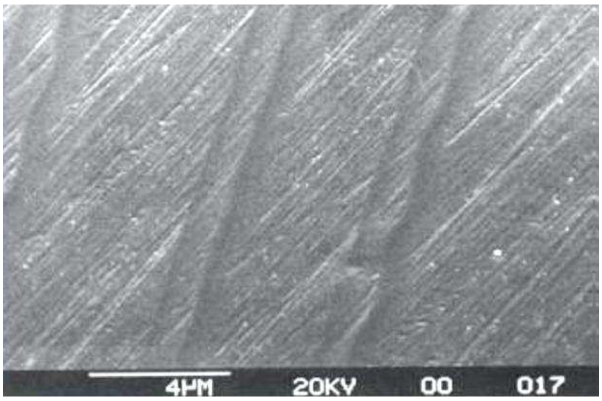

Figure 4.5 Example of uniform width scar produced by a contact stylus (Griffiths 2001)

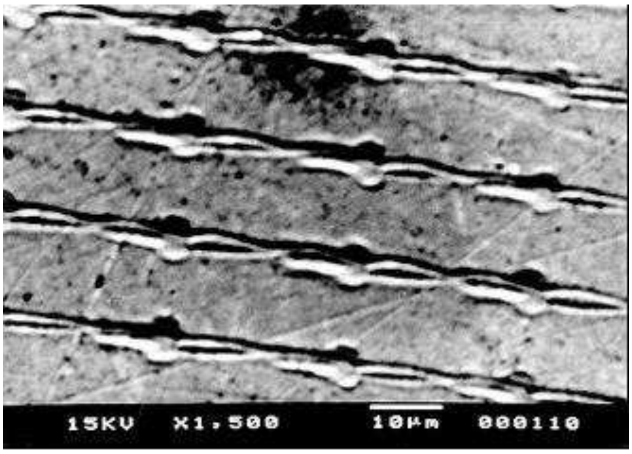

Figure 4.6 Example of uniform shock marks produced by a contact stylus on a brass sample (Mainsah *et al.* 2001)

The tactile considerations are mainly discussed in the literature as 2D problems even though in reality the stylus has three dimensions and certainly interacts with the surface not only in the trace direction but along the orthogonal direction (Stout and Blunt 2000).

All contact stylus instruments that measure areal surface topography are scanning instruments and the measurement data is obtained on the fly, hence the importance of the instrument dynamic characteristics. The dynamic characteristics are mainly concerned with the stylus trackability, which is the ability to track the surface faithfully without lift-off. It is possible to calculate the optimal trace speed and feature slopes, considering the natural frequency of the system and damping ratio, for which the stylus will not break contact with surface (Whitehouse 1990). The limited experimental results available are inconclusive and no optimum speeds for dynamic measurements have been suggested (Stout and Blunt

2000). The recommended speeds for 2D instruments generally are too conservative for 3D measurements because it increases the acquisition time.

Before concluding this section it is worth mentioning that there are different types of transducers or pickups that covert the vertical displacement of the stylus into an electrical signal (Garratt 1979). They can be classified in two categories: analogue and digital transducers (Smith 2002). Possibly the most common analogue transducer is the based on a linear variable differential transformer (LVDT) (Thomas 1999) and the frequent digital one is based on a phase grating interferometer (Smith 2002). Irrespective of the pickup type, the output is converted by instrument electronics and software into height measurements that are part of the measured topography data.

4.2 Same common aspects of optical instruments

The story of development of optical surface topography measuring instruments is twined with that of the contact stylus. Before 1980s, several optical techniques such as Linnik interferometers (Linnik 1930, Miroshnikov 2010), multiple beam interferometers (Tolansky 1960), fringes of equal chromatic order interferometers (Bennett 1976) and confocal scanning microscopes (Minsky 1988), were developed with potential for measurement of surface topography. Owing to the development of personal computers in the 1980s, phase shifting interferometers become available (Bhushan *et al*. 1985, Greivenkamp and Bruning 1992) shortly followed by the development of coherence scanning interferometers (Caber 1993, Deck and de Grout 1994) and confocal microscopes (Schmidt and Compton 1992).

There are a number of similarities between optical and contact stylus instruments. For example, contact stylus and optical instrumentation is prohibited in the measurement of undercuts, although recent research shows that the scattering effects could be used to gather information outside the normal bandwidth of operation (Coupland and Lobera 2010). However, in the relatively short overlapping history of stylus and optical instruments a number of papers have been published that highlight discrepancies between them that are usually due to mismatching the measurement conditions or using the optical instruments outside their capability (Hillmann *et al.* 1996, Brand and Fluegge 1998, Rhee *et al.* 2005, Leach *et al.* 2006). One thing is clear, optical instruments are needed in industry owing to their non-contact nature that allows for fast measurements of areas with relatively good lateral resolution.

The majority of optical areal surface topography measuring instruments are based on the classical design of the conventional microscope such that they inherit the characteristics of their precursor such as chromatic aberrations, spherical aberrations, comatic aberration, astigmatism, curvature of field and distortion, which are detailed elsewhere (Born and Wolf 1997, Hecht 2003, Murphy 2001). All these optical aberrations will affect the metrological characteristics of the instruments such as the linearity of the scales and the resolution (see chapters 6 and 7).

Currently, resolution is a very sensitive topic in the field of surface texture, especially in the ISO TC 213 working group 16, because it is seen as a critical parameter and drives instrument vendors to improve optics and processing algorithms such that they can claim lateral resolutions close or even better than the diffraction limit (de Lega and de Groot 2012). The most common definition used is the Rayleigh criterion (for incoherent illumination), which says that two imaged points on an object are distinguishable if the central maximum of the first point diffraction pattern (Airy disk – see figure 4.7) lies outside the first minimum of the second point diffraction pattern. Hence the optical instrument resolution that operates in air is

$$r = 0.61\frac{\lambda}{A_N}, \qquad 4.1$$

where r is the lateral resolution, λ is the mean wavelength and A_N in the numerical aperture of the objective lens. Other definitions are available such as the Sparrow limit, which replaces the 0.61 factor of equation (4.1) with 0.47, and the Abbe criterion which replaces the 0.61 factor with 0.5 (Lipson *et al.* 2011).

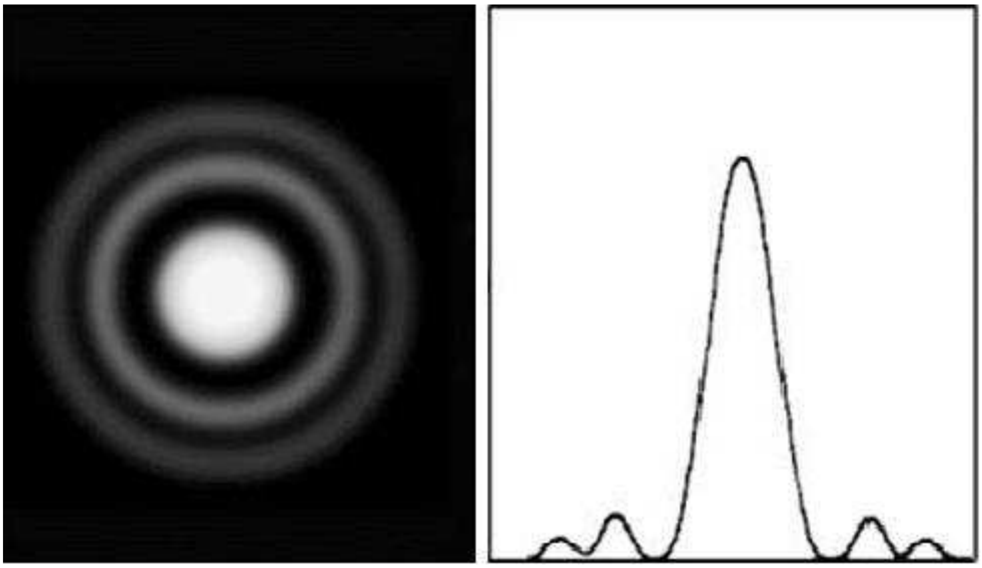

Figure 4.7 Diffraction pattern of an ideal small circular aperture – airy disk (adapted from *Astro Fundamentals: Light and its detection tutorial* – Liverpool John Moore University[1])

In the Sparrow limit case, two points are considered separate if their joint intensity function at the image plane has a minimum on the line joining their centre, whereas according to Abbe criterion two points are distinguishable if they are placed at a distance from each other larger than half the diameter of the central peak. Figure 4.8 depicts the difference between the three resolution criteria for incoherent illumination. In the Rayleigh criterion case there is a distinct central dip in the resulting intensity profile, whereas in the Sparrow limit case, there is no central dip. Abbe sits in between Rayleigh and Sparrow and in consequence a small depression in the central area intensity profile can be observed.

For coherent illumination, the Rayleigh definition is not applicable because the amplitude of the signals add before squaring resulting in an intensity map from which the separation between the two points is not possible. The Sparrow limit for coherent illumination replaces the 0.61 factor of equation (4.1) with 0.47, and Abbe criterion with 1 (Lipson *et al.* 2011).

---

[1] http://www.astro.ljmu.ac.uk/courses/phys134/scopes.html

Figure 4.8 Resolution limits: left Rayleigh, middle Abbe, right Sparrow (adapted from *Super-resolution microscopy tutorial* - the University of Utah[2])

Recently, some instrument vendors have started claiming resolutions based on line and space criteria, which is half of the Rayleigh criterion resolution (Leach 2011 – chapters 2 and 11).

These types of definitions are equally valid for 2D microscopes but not for areal measurements because when it comes to resolving 3D structures there is a more intimate relationship between the lateral resolution and the vertical resolution, see equation (4.2) (Leach 2011 – chapter 3),

$$\delta x \times \delta z = h, \tag{4.2}$$

where δx is the laterally resolvable distance, δz is the vertical resolution and h is a constant of the instrument. This is not an easy problem to solve in practice leading to disagreements when it comes to establish a common definition for the resolution of areal instruments. The answer lies in the instrument transfer function, or the response of the instrument in the spatial frequency domain, which provides information about the lateral resolution of the instrument (de Groot and de Lega 2005, de Lega and de Groot 2012).

More recent research shows that the optical transfer function or instrument transfer function can be used to improve the performance of the instrument (Mandal *et al.* 2012, de Lega and de Groot 2012), at least while the instruments work in the linear regime *i.e.* with no

---

[2] http://www.research.utah.edu/advanced-microscopy/education/super-res/index.html

scattering and inside the numerical aperture (Coupland and Lobera 2008), by measuring the point spread function (Yashchuk *et al.* 2008, Fujii *et al.* 2010, Mandal *et al.* 2010, de Lega and de Groot 2012). The point spread function is very similar in concept to the effect of the stylus geometry in contact stylus method, but unlike the stylus case, the point spread function is unusable for measurements of surfaces that force the instrument to depart from the linear response.

4.3 Coherence scanning interferometry

Interference microscopes were first proposed to be used for surface texture analysis at the end of the 1970s (Davidson *et al.* 1978). Two types of vertical scanning interference microscopes are commonly used for surface texture measurement: phase shifting interferometers (PSI) (ISO/FDIS 25178-603 2012, Leach 2011) and coherence scanning interferometers (CSI) (ISO/FDIS 25178-604 2012, Leach 2011). PSI (not used in this thesis as a test case) works with monochromatic illumination and evaluates the interference phase information to derive height information. CSI employs broadband illumination and assesses the interference signal strength to map the relative height differences against a linear scale. Some instrument manufacturers supply systems that allow access to both techniques by changing the illumination conditions and using different data processing algorithm.

In the classical set up, the active optical components of a CSI are mounted on a supporting bridge above a mounting table that are stably connected to each other forming the metrological loop. The basic interferometer setup, not including the metrological loop, is shown in figure 4.11.

In the upper part of the figure 4.11, the components of the instrument responsible for illumination, generally Köhler illumination (Murphy 2001), are presented together with the interferometric signal acquisition system. The latter system is made of a CCD camera, optical components that are used for projecting the interference pattern onto the CCD camera, a motion actuating device (drive unit) and a linear scale. The choice of the CCD camera, drive units and linear scales varies from one instrument to another. The interferometric signal is obtained using specially designed lenses, interchangeable in most cases, that incorporate different types of interferometer design. Typical designs of interferometric lens are based on the Mirau and Michelson configurations (Kino and Chim 1990); however, Linnik configurations (Linnik 1930, Davidson *et al* 1978) are also possible. The Mirau configuration is mainly used for 10× to 100× magnification objectives lenses and the Michelson configuration is used for low magnifications (5× and lower).

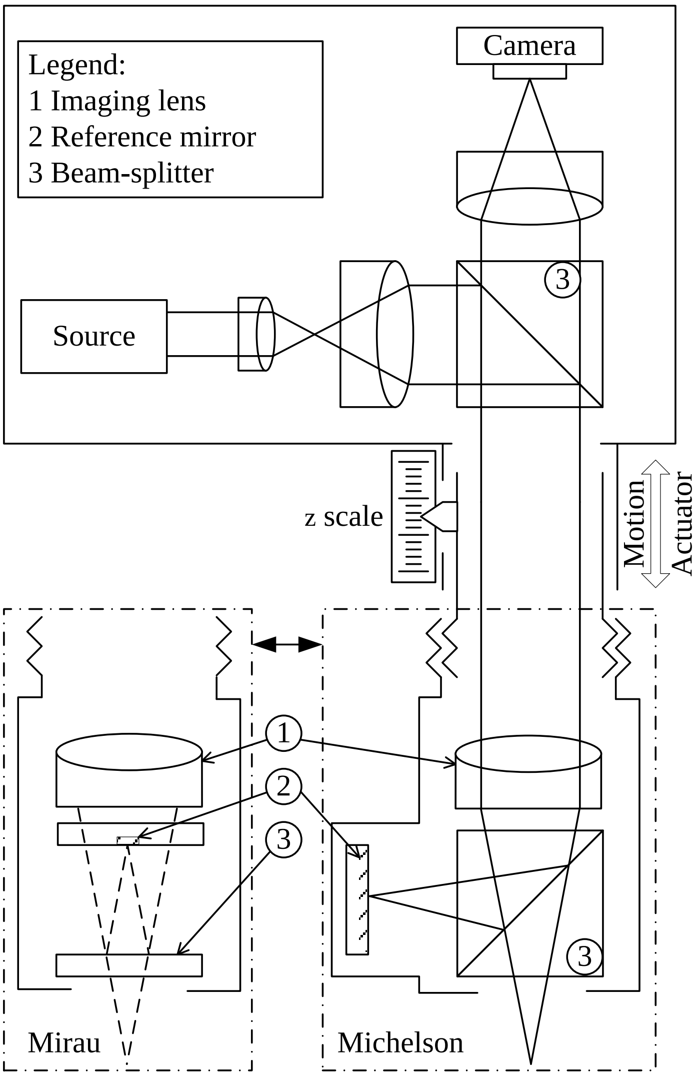

Figure 4.9 Interferometer set-up for CSI

The interferometric optical signal is captured by a CCD camera after the source light traverses two independent paths, one that is reflected from the reference mirror and one reflected from the surface of the measured sample. In essence, the interfrometric signal carries information about the difference between the surface topography of the reference mirror and the surface topography of the measured sample. The light source, broadband light in the CSI case, is divided and sent along the two independent paths by a beam-splitter which is also used to recombine the returning rays before being projected onto the CCD camera.

During the operation of the CSI, the relative optical path difference between the sample and the reference mirror is changed using a linear motion actuator that, in most cases, moves the optical components of the interferometer constant speed r along the *z* axis of the instrument varying only the relative sample position along the measurement arm of the interferometer whilst maintaining the same reference path. Simultaneously, the signal from each pixel of the CCD camera is recorded together with its reciprocal position along the scanning direction, which is given by the *z* scale of the instrument.

Because the CSI uses broadband illumination, the interference effect is strongest when the measuring optical path is equal to the reference optical path of the interferometer and it will quickly diminish as this condition is changed. Therefore, the interference signal at each pixel (see figure 4.12) will start oscillating when the sample is approaching equal path distance and will increase in amplitude until the sample passes the equal path distance condition after which the amplitude of the signal will quickly diminish, for example see Lee (1990) or de Groot and Deck (1995) and references therein.

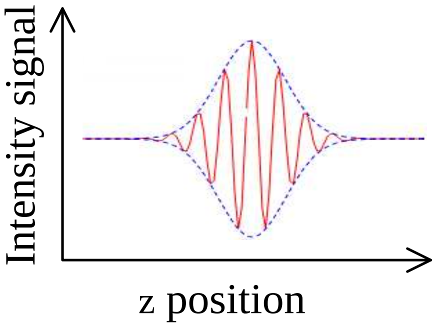

Figure 4.10 Pixel measured signal. In red is represented the raw signal and in blue is the modulation envelope

Height information is attained by processing the interference signal using different algorithms that, in essence, attempt to map as accurately as possible one defining attribute of the interference signal onto the *z* scale. ISO/FDIS 25178 –part 604 (see also Leach 2011) identifies five signal processing algorithms: envelope detection (Caber 1993), centroiding (Ai and Novak 1997), combining of envelope detection with phase estimation (Harasaki and Wyant 2000, de Groot *et al.* 2002), scan domain correlation (Sandoz 1997, Sandoz *et al.* 1997, Schwider *et al.* 1983) and frequency domain analysis (de Groot and Deck 1995). All these algorithms are based on various assumptions that do not hold in all the practical applications and, as a result, errors occur during the normal use of the instrument.

Common errors affecting the CSI are reviewed by Gao *et al.* (2008 and references therein). Along with well known errors that are mainly caused by surface discontinuities and usage of the instruments outside their operational bandwidth, which is given by the numerical aperture of the objective lens, Gao *et al.* (2008) identify other systematic errors that could be compensated. Common errors include: batwing effects that manifest along steps discontinuities and are either the result of interference between reflections of waves normally incident on the top and bottom surfaces following diffraction from the edge for steps smaller than the coherence length of the light source (Harasaki and Wyant 2000, Harasaki *et al.* 2000) or the effect of a phase change caused by the way the optical field interacts around the discontinuity for steps smaller than the coherence length; ghost steps (Proertner and Schwider 2001) characteristic to field-dependent dispersion in Mirau and Linnik interferometers also known as 2π errors (Harasaki *et al.* 2001, de Groot *et al* 2002); tilt-dependent dispersion (Lehmann P 2003) or a combination of field- and tilt dependent dispersion (Lehmann P 2006) is often the cause of errors; the effect of different phase changes on reflection between different materials (Doi *et al.* 1997, Harasaki *et al.* 2001, Park and Kim 2001); scattering errors that have been reported to increase the roughness of the measured samples (Hillmann *et al.* 1996, Brand and Fluegge 1998, Rhee *et al.* 2005, Leach *et al.* 2006), and can simply be explained with the measurement of a v-groove (Gao *et al.* 2006).

4.4 Imaging confocal microscopy (ICM)

Invented in 1957 by Marvin Minsky to help his research on neural characterisation (Minsky M 1961, Minsky 1988), imaging confocal microscopes were initially designed to observe features of biological structures that were not clearly resolved by a conventional microscope. Today confocal microscopes are also used in engineering application due to the high numerical aperture configuration of the magnification lenses allowing for measurement of high slopes (Wilson 1990).

ICM projects structured illumination patterns onto the surface under investigation and captures the returned light using to a pattern identical to the illumination pattern, which discriminates for returned rays that are out of focus (ISO/CD 25178-607 2012, Leach 2011). The basic instrument setup that uses a pinhole as the illumination pattern is presented in figure 4.11.

Light from a laser passes the illumination pinhole and is directed towards the sample *via* an objective lens. On return, the light is directed towards the detection pinhole, behind which is situated a photo-detector. At the focal plane of the objective lens the illuminated spot on the surface is diffraction limited and all the rays of the returned beam pass the illumination pinhole. If the sample is moved from this position the illuminated spot increases in size and the width of the returned beam is larger than the opening of the illumination pinhole. So, whilst the sample is scanned in and out of the focus of the objective lens using a linear motion actuator, similar to the CSI case, the intensity of light passing the opening of the detection pinhole increases reaching a maximum when the sample is situated in the focal plane of the objective, which reveals the height location (Conchelo and Hansen 1990), and decreases as the sample departs from this position.

Height information is attained by simply ascertaining the discrete scan position corresponding to maximum light intensity or more accurately employing fitting algorithms such as paraboloid fitting (Wilson and Masters 1994).

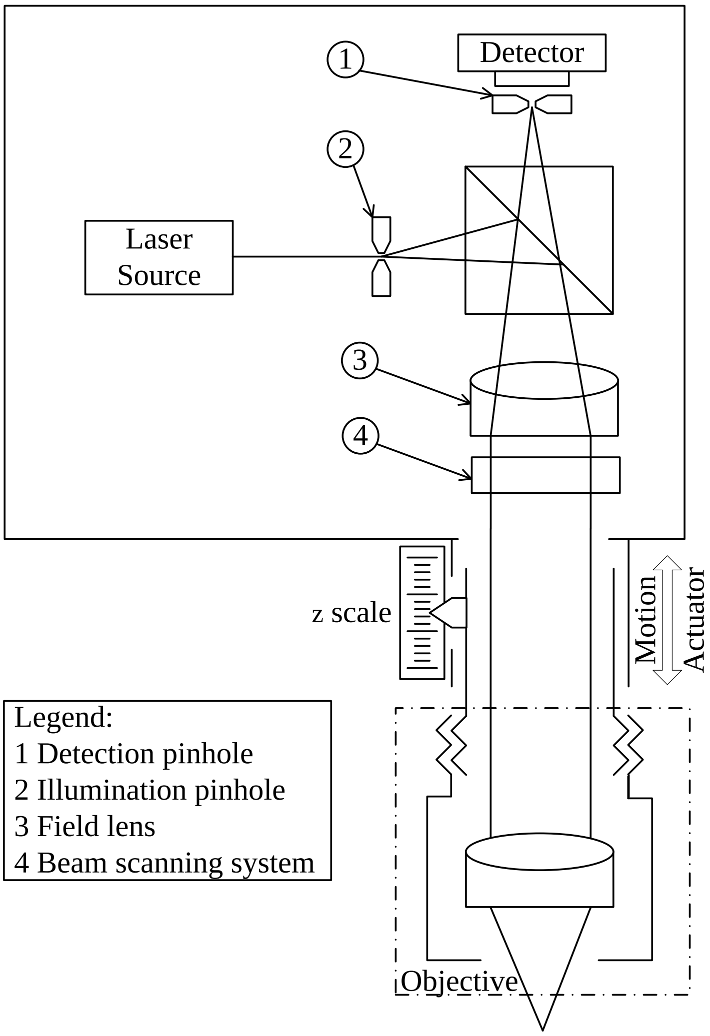

Figure 4.11 Imaging confocal microscope set-up

The intensity variation with the scan position is called the axial response (see figure 4.12).

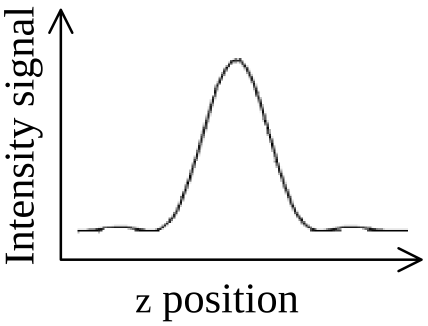

Figure 4.12 ICM axial response

For areal measurements the beam is scanned over a finite area across the surface of the sample using one of the following scanning systems: laser scanning that scans the light beam coming from a pinhole (Minsky 1988) or a slit (Sheppard and Mao 1988, Artigas *et al.* 1999, Botcherby *et al.* 2009) using ether a combination of two galvanometric mirrors moving in discrete steps to build the image in a raster fashion or video rate resonant scanners; disk scanning that use a Nipkow disk (Xiao *et al.* 1988, Tiziani *et al.* 2000, Tanaami *et al.* 2002), scan disks with parallel slits or point rotating slits are also used; and programmable array scanning (Verveer *et al.* 1998, Artigas *et al.* 2004, Karadaglic 2008).

ICM can have smaller lateral resolution than the one postulated by the Rayleigh criterion, at least from a theoretical perspective, due to the effect of the pinhole size, which in some instances is counterbalanced by the increased measurement noise at low magnifications due to the lack of sharpness of the axial response curve (Wilson 1990, Leach 2011).

5 Measurement noise and flatness deviation

Current techniques for determining the measurement noise and flatness deviation (Creath and Wayant 1990, Haitjema and Morel 2005, ISO/CD 25178-600 2012) are based broadly on the assumptions that the measurement noise can be decreased by averaging repeated measurements, the flatness deviation is systematic in nature and the measurements are performed on a calibrated flat reference surface.

The magnitude of the measurement noise can be determined by measuring the root mean square (RMS) value of the scale limited surface, *Sq*, of a flat surface of less than or equal to 30 nm peak to valley (VDI/VDE 2655 Part 1 2008). The challenge of the measurement noise test is to isolate the measurement noise from the intrinsic roughness of the sample and any flatness deviation of the instrument. A method of separating the measurement noise from the surface roughness of the flat is presented elsewhere (VDI/VDE 2655 Part 1 2008, Creath and Wayant 1990). The method consists of taking the difference between two repeated measurements. A further technique of error separation is based on the assumption that the instrument noise contribution to the RMS value of the average surface obtained from repeated measurements performed at the same location on the flat will decrease by the square root of the number of measurements (Haitjema and Morel 2005).

Similar to the measurement noise test, the flatness deviation test is performed on a flat surface but the parameter used to quantify the magnitude of the flatness deviation is the maximum height of the scale limited surface, *Sz*. Unlike *Sq*, the value of *Sz* is highly sensitive to local height variations such as scratches or contamination. It is, therefore, difficult to completely separate the contribution of the instrument from that of the flat and other spurious measurement data. One way to overcome these issues is to measure the topography of the flat at different locations (VDI/VDE 2655 Part 1 2008) without changing the instrument set-up and to average the height measurement at each location. The contribution of the flat and any spurious data should diminish, whereas the quality of the areal reference should be preserved.

Measurement noise and flatness deviation tests are relatively difficult to apply because the assumptions on which the current test methods are based are challenged in practice. For instance, the noise can be non-stationary in a statistical sense (Whitehouse 1976) so that averaging repeated measurements does not isolate the measurement noise from the flatness errors and sample topography, or the standard way of calibrating the flat standard may not match the spatial measurement bandwidth of the instrument (for example the S-filter nesting index used in the calibration certificate of the flat standard can be equal to the largest L-filter nesting index of the instrument). As they are presented in the next sections, some of the techniques require a large number of repeated measurements, which is not always practical. These challenges have to be addressed before being implemented in specification standards, otherwise the standard will be unusable.

In the next two sections, 5.1 and 5.2, practical tests for the measurement of the measurement noise and flatness deviation are presented, and in section 5.3 their contribution to the measurement uncertainty is discussed. Before the summary of this chapter, section 5.5, a method that allows the estimation of the combined effect of the measurement noise and flatness deviation to the measurement uncertainty is presented in section 5.4.

5.1 Measurement noise

5.1.1 Preliminary considerations

The $z(x, y)$ data set from an areal surface topography measuring instrument can be affected by various sources of noise such as: instrument electronics, which is also called the internal noise of the instrument; environmental noise generated by ground vibrations, ventilation (drafts or turbulence), sound, short and long-term temperature fluctuations, and external electromagnetic disturbances; and vibrations generated by those components of the instrument that are designed to move during the measurement.

In some instances the effect of the internal and environmental noise can be identified in isolation from other sources. For example, the majority of stylus instruments allow the recording of the output signal of the probe that contacts a sample without scanning in the *x* or *y* directions. This type of measurement is known as a static noise test and is generally performed in profile mode (ISO 25178-601: 2010). For instance, figure 5.1 and figure 5.2 present the results of two static noise tests along the fast axis (*x* axis) of a the stylus instrument. The measurement spatial bandwidth of the profiles is the same (1 µm sampling spacing and 1.4 mm sampling length); however, the temporal sampling frequencies are different, 100 Hz and 500 Hz, that correspond to scanning speeds of 0.1 mm s^{-1} and 0.5 mm s^{-1}, respectively.

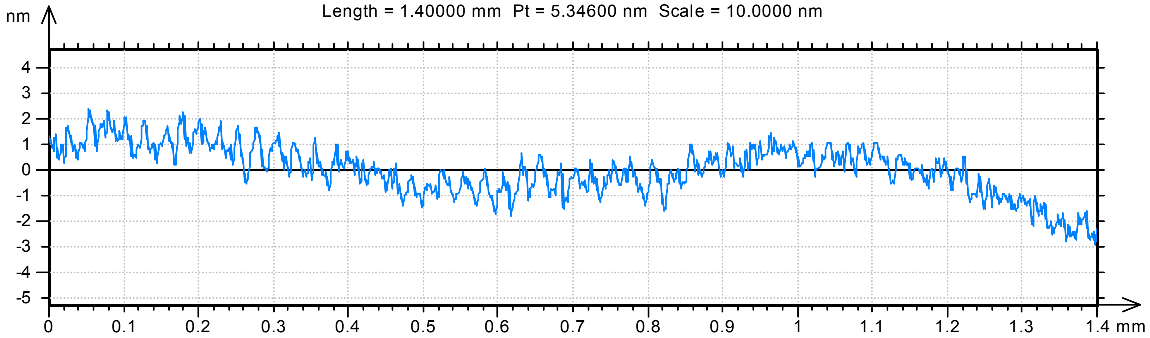

Figure 5.1 Example of the result of a static noise test for a stylus instrument equivalent to a profile measurement along the fast axis of the instrument at a speed of 0.1 mm s^{-1}, 1 µm sampling spacing and 1.4 mm sampling length

A dominant noise component at a temporal frequency of about 4 Hz can be identified in figure 5.1 and figure 5.2. The 4 Hz temporal frequency corresponds to a wavelength of 0.025 mm in figure 5.1 and a wavelength of 0.127 mm in figure 5.2. The frequency of 4 Hz was coupled into the instrument from the air conditioning system.

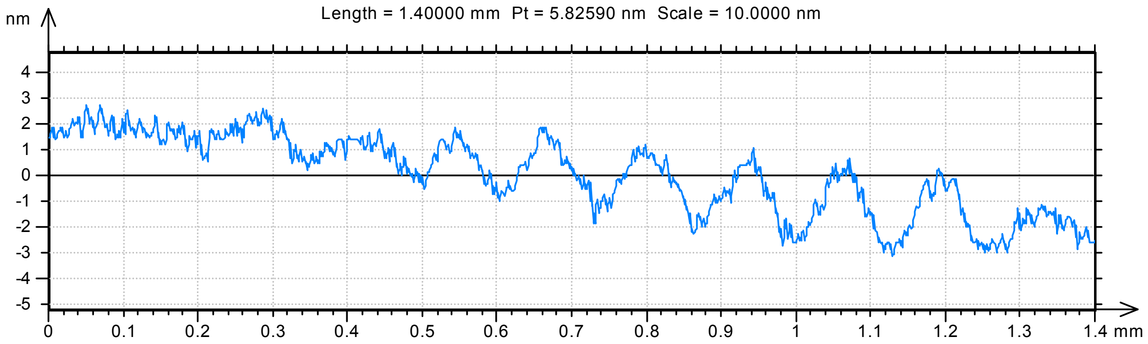

Figure 5.2 Example of the result of a static noise test for a stylus instrument equivalent to a profile measurement along the fast axis of the instrument at a speed of 0.5 mm s^{-1}, 1 µm sampling spacing and 1.4 mm sampling length

The low temporal frequency components of the noise that are not captured in the profiles extracted along the fast axis could be short spatial wavelength components along the slow axis (*y* axis) of the *xy* scanning instruments. It is not always possible to perform the static noise test along the slow axis of the instrument; hence, the contribution to the measurement uncertainty of the static noise cannot easily be considered. The aim of the static noise test is to identify issues with the setup of the instrument, but it is not essential for the measurement uncertainty because the static noise is incorporated into the dynamic noise (ISO 25178-601: 2010) of an *xy* scanning instrument. The dynamic noise is a combination of the internal noise of the instrument, environmental noise and the noise arising from the drive units at the time of scanning. The latter type of noise is also called measurement noise defined as: noise added to the output signal occurring during the normal use of the instrument (Leach R K 2011). Unlike the term dynamic noise, the term measurement noise is applicable to all types of areal surface topography measuring instruments.

5.1.2 Estimation of measurement noise

As discussed above, there are two methods that can be employed to determine the measurement noise, one that is based on a subtraction technique (VDI/VDE 2655 Part 1 2008, Creath and Wyant 1990) and one that is based on an averaging technique (Haitjema and Morel 2005).

The subtraction technique requires two repeated measurements at the same position on the sample in quick succession. The topography data of one measurement is subtracted from the topography data of the other measurement such that the resulting topography data contains only information about measurement noise. The subtraction method combines the variances of two identical probability distributions that each characterise the noise of the instrument. It follows that the measurement noise (Sq_{noise}) can be estimated by the Sq of the resulting topography divided by the square root of two:

$$Sq_{noise} = \frac{Sq}{\sqrt{2}}. \qquad 5.1$$

The averaging method is based on the assumption that the noise contribution decreases when averaging multiple measurements of the surface topography at the same location on a sample (flat). The measured Sq on the surface of a flat is a function of the instrument noise (Sq_{noise}) and the flat roughness (Sq_{flat})

$$Sq = \sqrt{Sq_{flat}^2 + Sq_{noise}^2}. \qquad 5.2$$

After n repeated measurements at the same location on the surface of the flat, the contribution of the instrument's noise into the root mean square height of the averaged surface topography (Sq_n) is decreased by the square root of n while that due to the flat is preserved

$$Sq_n = \sqrt{Sq_{flat}^2 + \frac{1}{n} Sq_{noise}^2}. \qquad 5.3$$

The instrument noise can be extracted from equations 5.2 and 5.3 as follows:

$$Sq_{noise} = \sqrt{\frac{Sq^2 - Sq_n^2}{1 - \frac{1}{n}}}. \qquad 5.4$$

It is difficult to recommend an exact number *n* of repeated measurements but one approach is to make sufficient repeated measurements such that the estimated measurement noise does not change appreciably with an increased number of averaged topography data.

The averaging method is particularly useful when the acquisition software of the instrument can automatically produce an average surface from multiple measurements. The CSI instrument used as test case has an option of averaging two, four, eight and sixteen measurements. The unfiltered results of the measurement noise test of the CSI show that two repeated measurements ($n = 2$) could be enough to measure the noise of the instrument (see table 5.1) because the difference in Sq_{noise} between two and sixteen repeated measurements is small. The value of Sq_{noise} after two measurements would be valid even allowing for a difference of 10 % from the value obtained after sixteen repeated measurements.

In comparison, the subtraction method average result is Sq_{noise} = 0.670 6 nm with an associated standard deviation of the mean of 0.000 5 nm for the case of the 50× magnification objective lens and Sq_{noise} = 0.347 8 nm with an associated standard deviation of the mean of 0.001 3 nm for the case of the 20× magnification objective lens (see

table 5.2). The difference between the two methods is not appreciable (less than 10 %).

Table 5.1 Unfiltered measurement noise of the CSI on a transparent glass flat – averaging method results

Number of averaged measurements	Sq_{noise} / nm	
	20×	50×
2	0.339 8	0.665 0
4	0.349 9	0.665 0
8	0.340 2	0.665 5
16	0.341 5	0.665 0

Table 5.2 Unfiltered measurement noise of the CSI on a transparent glass flat – subtraction method results

Subtractions	Sq_{noise} / nm	
	20×	50×
1	0.346 8	0.671 6
2	0.348 3	0.670 0
3	0.346 6	0.671 2
4	0.349 4	0.669 6

Both subtraction and averaging methods work successfully in the CSI case because the effect of the noise can be easily separated from the topography of the sample and the form errors. However, when the noise becomes non-stationary in a statistical sense (Whitehouse 1976), *i.e.* the noise cannot be removed by averaging, the separation is not possible. An example of such noise was found during the measurement noise test of the stylus instrument. Two repeat areal scans of 1.5 mm by 1.5 mm show a non-repeatable form-like behaviour of the *y* axis drive unit that does not allow the use of either the subtraction or the averaging method to isolate the measurement noise from the sample topography (figure 5.3 and figure 5.4).

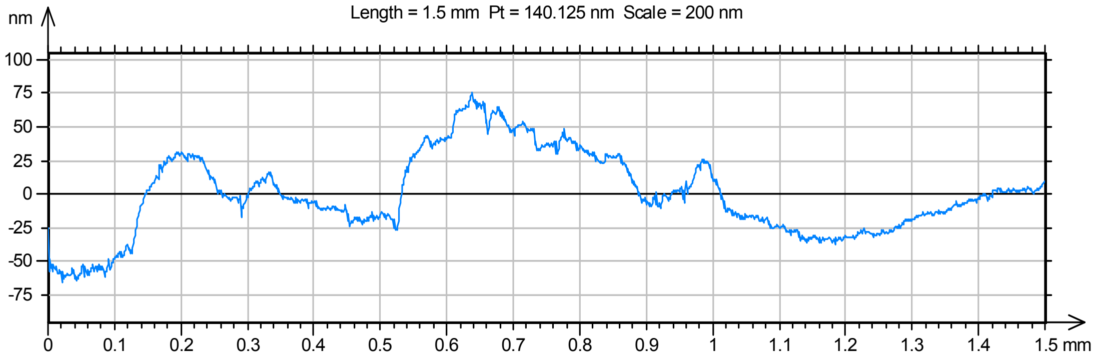

Figure 5.3 Profile along the *y* axis of the stylus instrument resulting from averaging the topography in the *x* direction - first measurement noise test

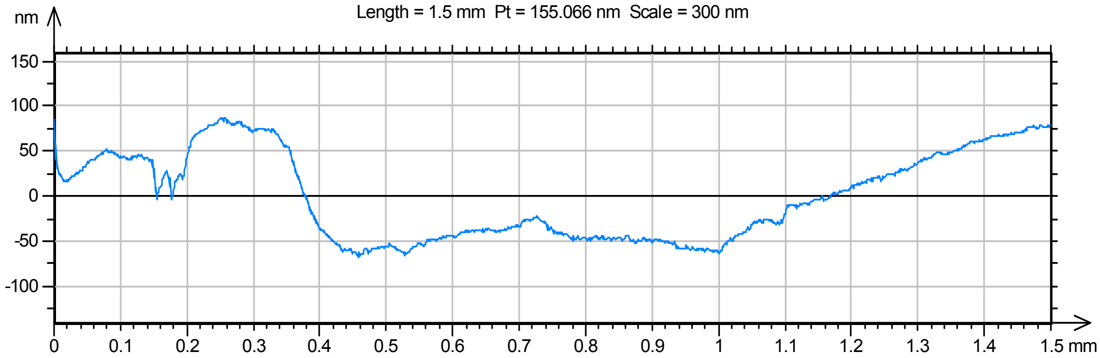

Figure 5.4 Profile along the *y* axis of the stylus instrument resulting from averaging the topography in the *x* direction - second measurement noise test

In the stylus instrument case some of the components of the measurement noise could be analysed in profile mode along the fast axis of the instrument but the non-repeatable form errors of the *y* axis drive unit will ultimately govern the uncertainty associated with the stylus instrument measurements. The measurement noise analysis along the fast axis is not that different from the static noise test along the same axis. The analysis only brings supplementary information in regard to the *x* axis drive unit that is not necessarily usable for the areal measurement uncertainty that needs the combined effect of the slow and fast axes measurement noise contributions. The magnitude of the errors caused by the slow axis of the stylus instrument allows the non-stationary behaviour of the measurement noise to be seen. In some instances it is not as easy to observe the non-stationary behaviour of the measurement noise. Such a characteristic was found during the measurement noise test of the ICM instrument. The averaging method results for the 50× and 20× magnification objectives are presented in table 5.3 and the subtraction method results are presented in table 5.4.

The averaging method results show that with the increased number of averaged measurements, the Sq_{noise} value decreases, so the averaging method is likely to isolate the noise from the form errors only when using a large number of measurements. The average value of the measurement noise obtained from the subtraction method is $Sq_{\mathrm{noise}} = 1.56$ nm for the 50× magnification objective lens with an associated standard deviation of 0.22 nm and

Sq_{noise} = 5.0 nm for the 20× magnification objective lens with an associated standard deviation of 1.2 nm.

Table 5.3 Unfiltered measurement noise of the ICM instrument on a transparent glass flat – averaging method results

Number of averaged measurements	Sq_{noise} / nm	
	20×	50×
2	9.2	1.9
3	7.1	2.2
4	6.5	1.7
5	5.4	1.4

Table 5.4 Unfiltered measurement noise of the ICM instrument on a transparent glass flat – subtraction method results

Subtractions	Sq_{noise} / nm	
	20×	50×
1	6.7	1.4
2	4.7	1.5
3	4.3	1.9
4	4.1	1.5

5.2 Flatness deviation

An important feature of areal instruments is the quality of their areal reference against which the surface topography is measured. Scanning instruments use a reference guide whereas some optical instruments rely on the quality of the optical components to provide a good quality areal reference. Any departure of the areal reference from an ideal flat surface will give rise to errors in the *z* axis measurement direction. VDI/VDE 2655 Part 1.1 (2008) recommends the measurement of flatness deviation by averaging ten measurements acquired at different locations on a good quality flat so that the contribution of the topography of the flat and the measurement noise is minimised, and the flatness deviation of the instrument is preserved. These measurements are not always straightforward because the measurements are often affected by spurious data of high z axis amplitude. In these situations the measurements have to be repeated, or filtration and outlier removal methods (Ismail *et al.* 2010) have to be employed in order to achieve effective measurement of *Sz*.

A threshold method is proposed that can be easily applied and does not filter the data. The method uses a high order polynomial (twelve was used in this case) to remove the form and thresholds the peaks and valleys of the residual surface that are larger than three times the *Sq* value that is calculated on the residual surface. As a result, the *Sp* (maximum peak height) and *Sv* (maximum pit depth – see ISO 25178-2: 2012) values will be three times *Sq*. As long as high frequency flatness components are not present in the residual surface a lower order polynomial can be used to remove form. Finally, the form topography and the threshold residual surface are summed to obtain the threshold surface topography (see figure 5.5 for the process flow).

Despite the fact that it is difficult to propose an exact threshold recipe it is simple to determine whether the threshold has been effective without affecting the measurement of the flatness deviation of the instrument in such a manner that the magnitude of *Sz* is underestimated. Spurious data appear at different (x, y) positions inside the repeated measured areas and as a result their amplitude decreases directly proportional to the number of averages. If the threshold operation is properly applied, the maximum of the *Sz* value of the non-averaged repeated measurements is larger than the *Sz* value of the averaged topography.

The choice of polynomial form removal is arbitrary because the same results can be obtained using a standard Gaussian filter or any other filter. As long as the residual surface with the removed high summits and deep valleys is added back on the filtered surface and *Sz* value of the non-averaged repeated measurements is larger than the *Sz* value of the averaged topography, the operation of removing spurious data can be considered successful.

Similar to choosing the order of the polynomial, the cut-off wavelength of the filter is very difficult to define as the size of the spurious data varies.

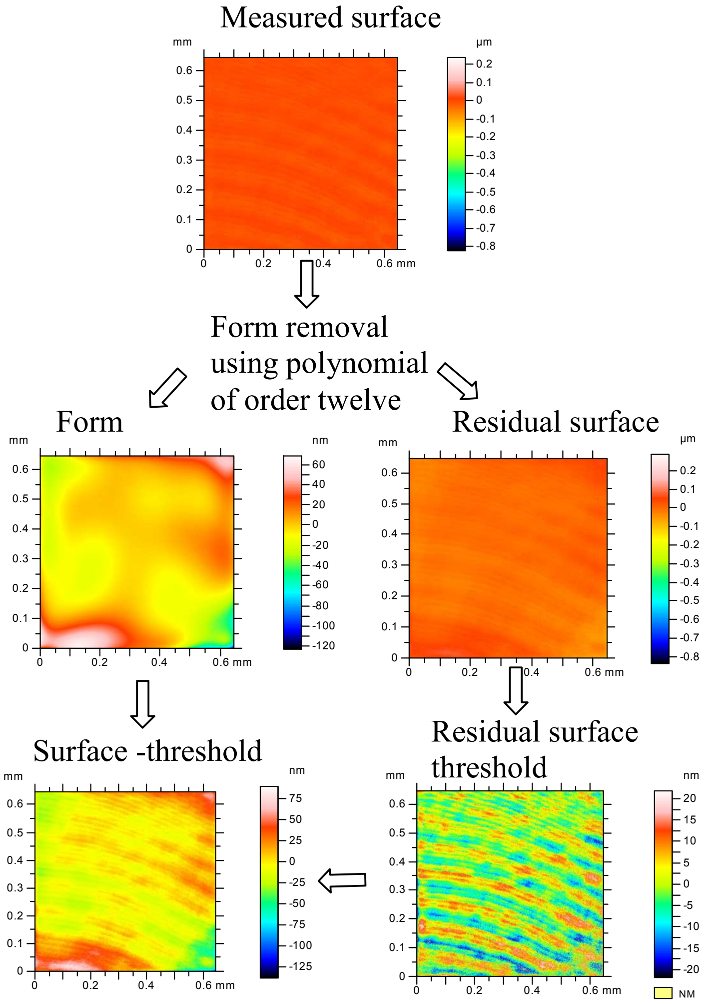

Figure 5.5 Flow chart of threshold method

An example of flatness measurement results on a CSI is presented in table 5.5. Table 5.5 shows that after averaging ten measurements *Sz* is 1.9 nm for the 20× magnification objective lens and 2.7 nm for the 50× magnification objective lens. Before the data threshold the maximum *Sz* value of the repeated measurements was in excess of 200 nm for both magnification objective lenses. Without data thresholding the number of repeated measurements required was close to one hundred.

Table 5.5 Unfiltered measured flatness of the CSI

Number of repeated measurements	Sz_{flatness} / nm	
	20×	50×
2	3.3	3.5
3	2.6	3.6
4	2.6	3.2
5	2.8	3.7
6	2.3	3.5
7	2.2	3.3
8	2.0	3.1
9	2.1	3.0
10	1.9	2.7

The flatness deviation is determined by the ‘virtual’ scratch present in the areal reference of the instrument (see figure 5.6). The areal reference is inherited from the quality of flat used during the flat adjustment of the instrument. A better quality flat would have produced a better quality areal reference.

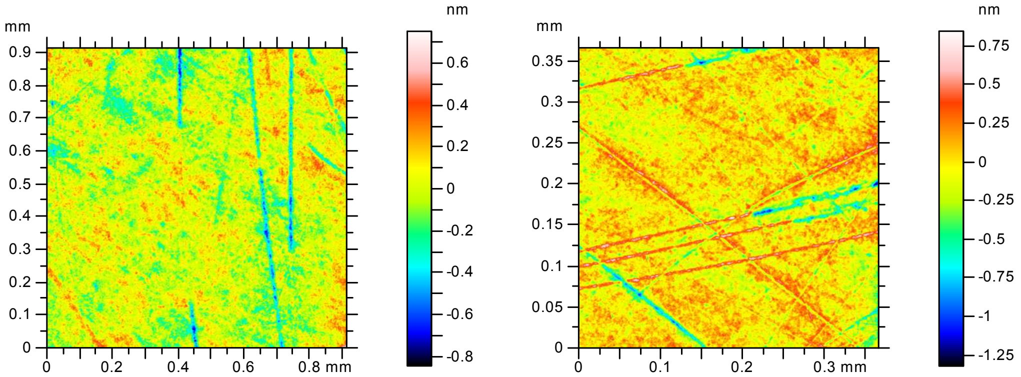

Figure 5.6 Flatness of a CSI that used the 20× magnification objective lens (left) and 50× magnification objective lens (right) to measure a transparent glass flat - result after ten averaged measurements

It is not possible to recommend the exact number of repeated measurements because it depends on the rate at which the value of *Sz* stabilises. The task is even more difficult when the value of *Sz* does not smoothly decrease with an increased number of averages such as with the CSI 20× magnification objective lens. Such behaviour is better seen in the case of the ICM with the 50× magnification objective lens (see table 5.6). Therefore, stating a single number of repeated measurements is impossible to be globally accepted.

The ICM with the 50× magnification objective lens seems to be affected by different flatness deviation errors at different positions of the vertical scan. This could be due to non-repeatable flatness deviation errors or it could be the effect of non-stationary noise. In contrast, the flatness deviation of the 20× magnification objective lens seems to be repeatable and much larger than the effect of any spurious data such that only two repeated measurements are sufficient to determine its flatness deviation (see figure 5.7).

Table 5.6 Unfiltered measured flatness of the ICM

Number of repeated measurements	Sz_{flatness} / nm	
	20×	50×
2	210	34
3	207	35
4	202	32
5	203	38
6	203	31
7	199	30
8	195	29
9	197	29
10	193	28

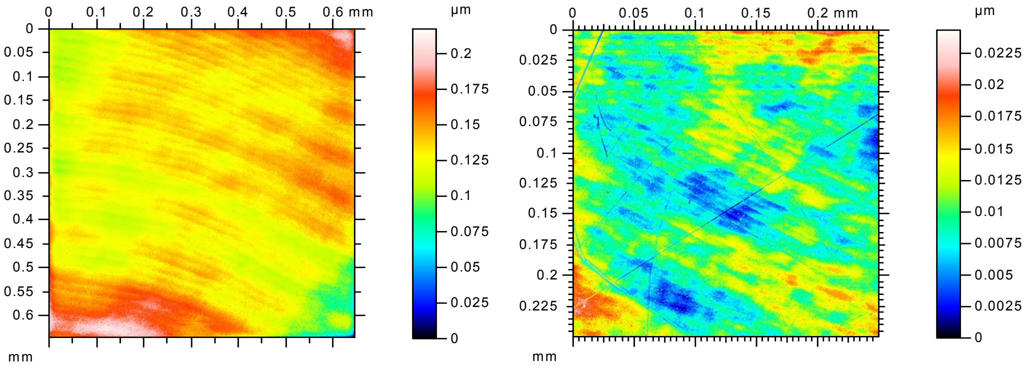

Figure 5.7 Flatness of a ICM that used the 20× magnification objective lens (left) and 50× magnification objective lens (right) to measure a transparent glass flat - result after ten averaged measurements

In the case of instruments that are known to have a flatness deviation larger than the *Sz* value of the flat, only one measurement will suffice. The downfall of this method of estimating the flatness deviation is that the flats are not traditionally calibrated in the spatial measurement bandwidth of the instrument and this makes the measurement traceability of the instrument very difficult to demonstrate. However, CSI type instruments could be used to qualify the flats in the required measurement bandwidth.

5.3 Measurement uncertainty

The measurement noise contribution to the overall measurement uncertainty is propagated in the form of a normal distribution that has an expectation equal to zero and a variance equal to the square of the value of the measurement noise, N(0, Sq_{noise}^2) (BIPM 2008b). The flatness deviation contribution to the measurement uncertainty is propagated in the form of a rectangular distribution, R(-$Sz_{flatness}/2$, $Sz_{flatness}/2$), that has a variance equal to the $Sz^2_{flatness}/12$ (BIPM 2008b). The combined effect of the measurement noise and flatness deviation on the *z* axis measurement standard uncertainty u_{NF} is given by (BIPM 2008a)

$$u_{NF} = \sqrt{Sq_{noise}^2 + \frac{Sz_{flatness}^2}{12}}. \quad 5.5$$

In practice the topography data is filtered before areal parameters are computed, so the Sq_{noise} and $Sz_{flatness}$ have to be calculated from the resulting topographies of the measurement noise and flatness deviation tests. The filtering process is based on the lateral measurement bandwidth of the instrument. Unless specified, the filtering can be established in accordance with ISO 25178 part 3 (2012), which recommends basic rules that allow the choice of S-filters and L-filters/F-operators. Each filter/operator has a range of pre-set values called nesting indexes that set the size of the primary surface and sampling spacing. The S-filter nesting index relates to the maximum sampling spacing, or resolution, and the L-filter or the F-operator relate to the maximum size of primary surface.

Table 5.7 presents the minimum S- and the maximum L-filter that are specific for each instrument used as a test case. Table 5.8 presents the values of the measurement noise and flatness deviation of the CSI and ICM after applying the filters specified in table 5.7.

Table 5.7 S-filter is based on the maximum sampling spacing not on the resolution of the instrument

ISO25178-3 filters	CSI		ICM		stylus	
	20×	50×	20×	50×	1 mm/s	5 mm/s
S-filter / µm	5	2	2.5	0.8	5	5
L-filter / mm	0.8	0.25	0.5	0.25	1	1

Table 5.8 Combined standard measurement uncertainty (u_{NF}) contribution of the measurement noise and flatness deviation

ISO25178-3 filters	CSI		ICM	
	20×	50×	20×	50×
Sq_{noise} / nm	0.17	0.34	4.1	1.4
Sz_{flatness} / nm	1.6	2.2	162	27
u_{NF} / nm	0.5	0.7	47	8

5.4 An alternative method

The methods for determining the measurement noise and the flatness deviation presented above can isolate with success in some cases (for example, for the CSI), these two metrological characteristics but they can run into difficulties when the basic hypotheses on which they rely are disputed (for example, for the ICM or stylus instrument case with non-stationary noise). The relevance of the methods presented above for assessing the measurement noise and flatness deviation is further challenged by other practical problems such as the different response of the instrument with different samples that have similar topography but have different optical properties, or significant variations in the metrological characteristics within the measurement range of the instrument.

A simple test that challenges the relevance of the measurement noise test of the CSI consists of measurements of two different flat surfaces, one transparent and one opaque. The measurement noise for the opaque surface (Sq_{noise} = 0.29 nm for the 50× magnification objective lens) is smaller than the measurement noise for the transparent surface (Sq_{noise} = 0.67 nm for the 50× magnification objective lens) possibly due to the different signal to noise ratios for the two measurements. In the case of the ICM, the flatness deviation varies significantly with the position of the scan within the vertical range of the instrument, whilst for the stylus instrument the flatness deviation varies significantly along the y axis range. In the ICM case the flatness deviation variation along the z axis range could be due to imperfect optics and non-ideal movement of the moving optical components against the fixed optical components of the instrument, whereas the variation of the flatness deviation errors of the stylus instrument could be primarily due to the quality of the y axis stage (Mainsah *et al.* 1994).

There are also practical difficulties with implementing the measurement noise and flatness deviation tests as presented above that are caused by the fact that these tests require a large number of measurements, and are not always simple to implement and fast to perform. Some of the necessary operations may not be available in the analysis software such as topography averaging or subtraction. It is also difficult to recommend the exact number of repeated measurements.

As previously discussed, the measurement noise and flatness deviation measurements have to be filtered before propagating their effect into measurement uncertainties. Once the filtering process is considered it can be argued that the difference between the measurement noise and flatness errors is that they are situated in different areas of the spatial measurement bandwidth, therefore, using appropriate filters, the flatness effect could be separated from the measurement noise contribution. This is not always the case because, as was demonstrated in figure 5.3 and figure 5.4, there are cases when the noise and flatness errors cannot be separated.

One way around the potential problems of the averaging and subtraction methods could be a combination of different filters that are applied to the measurement of a flat. A robust Gaussian filter (Zeng W *et al.* 2010) or a median filter (Stout and Blunt 2000) will smooth the surface such that any spurious data will be removed and the value of *Sz* will account for form measurements with some noise left un-filtered. The residual surface will contain primarily noise that is then filtered with a Gaussian S-filter. The spurious data will be transmitted into the noise measurement and will only have a limited influence on the *Sq* value. This method, together with the use of an un-calibrated flat, will tend to overestimate the magnitude of the flatness deviation but this is at least conservative from the point of view of the uncertainty evaluation. The only drawback of this approach is that it is difficult to establish the bandwidth of the robust Gaussian filter or median filter.

An alternative method for estimating the combined effect of the measurement noise and flatness deviation error is proposed based on the threshold technique using a high order polynomial as discussed above. The threshold process is identical to the process presented in figure 5.5 with only one difference that consists of using a 2 × *Sq* cut-off point instead of a 3 × *Sq* cut-off point. The resulting data set is then S-L or S-F filtered and only the *Sz* value is calculated. Some results are presented in table 5.9 where some data used to assess flatness for the CSI and ICM and five measurements of the flat standard using the stylus instrument was processed as suggested above. In this case, the flatness deviation and measurement noise contribution to the measurement uncertainty is propagated in the form of rectangular distribution with inexactly prescribed limits, CTrap($-Sz_{flatness}/2$, $Sz_{flatness}/2$, σ_{Sz}), that has a variance equal to the $Sz^2_{flatness}/12 + \sigma^2_{Sz}/9$ (BIPM 2008b).

It is likely that in the case of the CSI and ICM with the 50× magnification objective lens the *Sz* value is influenced by the topography of the flat whereas in the case of ICM with the 20× lens the topography of the flat plays no role because it is relatively small compared to the flatness deviation. This alternative method does not isolate the measurement noise from the flatness deviation. However, it finds the combined effect of the measurement noise and flatness deviation to the *z* axis measurements.

Table 5.9 Combined effect of the measurement noise and flatness deviation

	CSI		ICM		stylus	
Measurement ID	20×	50×	20×	50×	1 mm/s	5 mm/s
	Sz / nm					
1	2.4	2.7	180	30	115	48
2	2.2	2.8	164	40	165	49
3	2.4	3.8	178	41	113	58
4	3.0	4.1	163	33	108	39
5	2.5	2.9	175	36	65	244
Average	2.5	3.3	172	36	113	88
Standard deviation	0.13	0.29	4	2.1	16	39
u_{NF} / nm	0.7	0.9	50	10	33	28

5.5 Summary

Currently there are established methods for testing the measurement noise and flatness deviation of areal surface topography measuring instruments, including those presented in sections 5.1 and 5.2, that are used by national measurement institutes, academic institutions and the research and development facilities of instrument manufacturers. These methods are based on the assumption that measurement noise is stationary in a statistical sense and the flatness deviation behaves as a systematic error. However, as demonstrated in in chapter 5, such assumptions do not always apply. This makes the measurement noise and flatness deviation tests difficult to apply or unreliable in a quality control system. Other difficulties that arise when implementing the averaging and subtraction methods into a production quality system are: the long time required to perform the tests; spurious measurement data that affect the effectiveness of the tests; and the validity of the tests, especially in the case of the measurement noise test for optical instruments when there is a difference between the optical properties of the flat and the surface being measured.

An alternative to the averaging and subtraction methods for testing the measurement noise and flatness deviation is the method presented in section 5.4. This alternative method has the tendency to overestimate the combined contribution of the measurement noise and flatness deviation to the z axis scale uncertainty, but in most cases, this will not be significant unless sub-nanometre measurement uncertainties are required, such as in the CSI case. In the case of large flatness deviation errors (for example, in the case of the ICM with the 20× magnification objective lens) the measurement uncertainty is not affected, whereas for instruments that are characterised by nanometre-order residual flatness, the topography of the flat begins to affect the magnitude of the measurement uncertainty, but with no serious effect because it will not affect the overall measurement uncertainty associated with the z axis measurements.

None of the methods discussed requires a calibrated flat such that the traceability could be under debate. In practice, it is very difficult to comprehensively and appropriately calibrate a flat over the full measurement spatial bandwidth of areal surface topography measuring instruments. The traceability of the flat is often established through calibrations that have a sampling distance of 0.5 mm (for example using a Fizeau interferometer), which is comparable to the field of view of a large number of optical areal surface topography measuring instruments. In reality, the flatness measurements are traceable to the calibration of the instrument using measurements of a small and calibrated step height that should be performed as part of the calibration of the amplification and linearity of the scales of the instrument.

A simple procedure for flatness deviation measurement can be based on the method described in section 5.4 and should consist of at least five measurements uniformly distributed in the instrument measurement volume. The contribution to the measurement uncertainty should follow the guidelines presented in section 5.5.

If a calibrated flat is preferred during the flatness deviation tests, the traceability could come from an instrument such as a CSI, which has in turn been calibrated against a primary instrument, but the compatibility of the measurement bandwidth and calibrated bandwidth has to be carefully considered (Leach and Haitjema 2010).

6 Amplification, linearity and perpendicularity of the scales

Amplification and linearity tests establish the relationship between the ideal response curve and the instrument response curve on each of the *x*, *y* and *z* scales. Figure 6.1 shows a typical example of a linear scale response curve. The linearity of the axes is given by the maximum deviation of the instrument response curve from the linear curve, where the slope is the amplification coefficient.

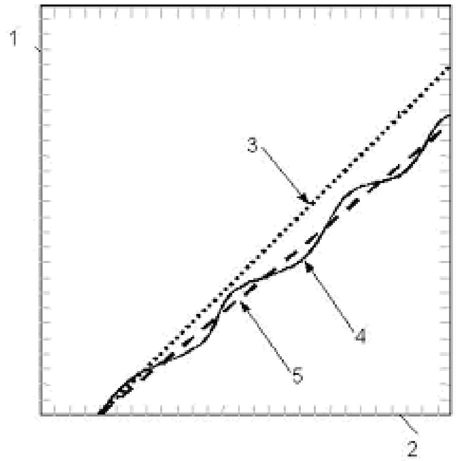

Figure 6.1 Example of an instrument response curve, where: 1 measured quantities, 2 input quantities, 3 ideal response curve, 4 response curve, 5 linear curve whose slope is the amplification coefficient (from ISO 25178-601 2010)

Amplification and linearity tests require calibrated material measures capable of providing multiple values uniformly distributed within the instrument range. However, this is a prerequisite rarely fulfilled in practice, especially during the test that provides information about the *z* axis linearity and amplification coefficient (but see Boedecker *et al.* 2011).

The amplification and linearity tests of the *z* scale are discussed in section 6.1. Section 6.2 describes the amplification and linearity tests of the *x* and *y* scales. Before the summary section, the contribution of the amplification and linearity to the measurement uncertainty is discussed in section 6.3.

6.1 z scale

Areal surface topography measuring instruments are potentially very accurate height measuring devices (Brand and Hillmann 1995, Haitjema 1997) as long as the instruments are calibrated, and if the instruments are not challenged by the design of the height standard or its orientation relative to the *z* axis of the instruments.

The design of the height standards could introduce errors, for example those standards manufactured using two different materials (chrome on glass), for both stylus (due to different mechanical properties of the two materials (Whitehouse 1994)) and optical instruments (due to different optical properties of the materials (Doi *et al.* 1997)). The aim of the calibration of the *z* scale is to isolate and measure only the response curve of this scale from which amplification coefficient and any non-linearity errors can be derived, avoiding the effect of other influence parameters into the *z* measurement. The surface of the calibration standard should be nominally parallel to the areal reference of the instrument such that the mathematical process of tilt removal and the quality of the *xy* scale have limited effects on the height analysis.

Another limitation for achieving small *z* measurement uncertainties is the uniformity of the height standards. Small depth height standards are generally of good quality, which allows for nanometre measurement uncertainty. Large height standards are characterized by non-uniformity of the groove, which generates non-repeatability in the profile assessment of the order of tens of nanometres (Haitjema 1997). The areal measurement should overcome the effect of standard uniformity because the height measurement could be expressed as the average of a greater number of profiles (for example 1000 profiles) than in the profile case (up to twenty five profiles to as low as five profiles). Areal measurements also allow for precise positioning over the calibrated area of the height standard that will also help to provide more reliable results.

One situation to avoid is the calibration of the z axis using a single height standard, which is also used to adjust the software of the instrument. This is because it could only shift the response curve in such a way that it crosses the ideal response curve only at one point. One height standard does not provide sufficient information about the z axis response curve. Instead z axis calibration should involve different height standards with various heights that establish the relationship between the ideal response curve and the instrument response curve. The height standards should cover the entire range of the z axis, or at least they should range from the minimum to the maximum height of interest and be measured at different positions inside the instrument range. The linearity and amplification coefficient can be extracted from the measurement results by simply performing a linear fit against the certified values of the height standards.

Currently there is no standardised analysis of the height standard measurement in areal mode. One method of measuring the height of the height standard, which uses the areal data and standard height analysis (ISO5436-1: 2000), is to calculate the depth from the average of all the parallel profiles that run nominally perpendicular to the step direction. Figure 6.2 presents a flowchart of the analysis of the measured height standard in areal mode (figure 6.2 top). The ISO 5436-1 (2000) analysis (figure 6.2 bottom) is performed on the middle groove of the average profile (figure 6.2 middle).

The range of the z scale of the CSI instrument is 100 µm and the maximum depth of the available height standards is nominally 17 µm, height which does not cover the instrument range. However the instrument can measure a similar depth at any position inside the instrument range such that the z scale has to be certified for such a situation.

The CSI measurement results were compared to the values reproduced by the height standards that were measured using the NPL Areal Instrument (see chapter 2). The height standards were measured in five positions within the range of the instrument (10 %, 30 %, 50 %, 70 % and 90 % of the instrument working range), which allowed a determination of the reproducibility of the measurements within the instrument range. At each of these five positions, the height standards were measured five times, which allows the calculation of the repeatability of the measurements (type A uncertainty – BIPM 2008a).

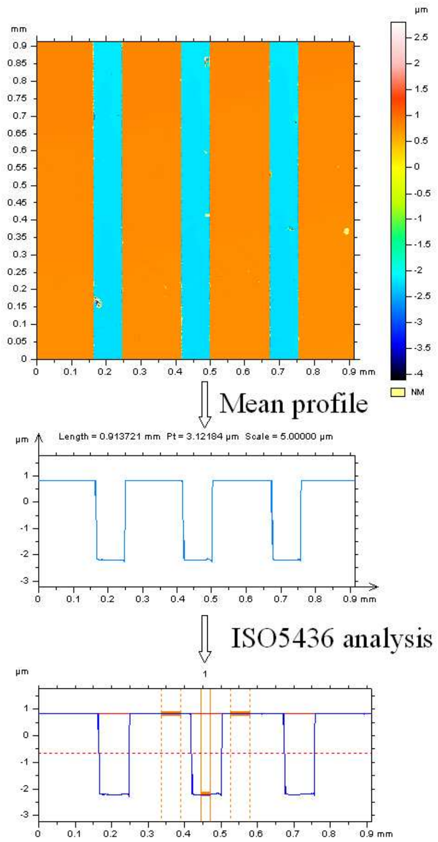

Figure 6.2 Flow chart of height standard analysis

The summary of the results is presented in table 6.1: the repeatability of height standard measurement was taken to be the maximum standard deviation of the mean value calculated at each of the five positions inside the instrument range; the reproducibility was calculated as the standard deviation of the average values of the height standards measured in each of the five positions; and the calibration standard uncertainty of the height standards with the NPL Areal Instrument (see chapter 2) was taken to be the traceability contribution.

The error plots of the CSI 20× and 50× magnification lenses are presented in figure 6.3 and figure 6.4 respectively. The value of the error bars is calculated as the quadratic sum of the repeatability, reproducibility and traceability values presented in table 6.1.

Table 6.1 CSI *z* scale calibration results

Nominal height	19 nm		350 nm		3 µm		17 µm	
Magnification	20×	50×	20×	50×	20×	50×	20×	50×
Error (at 50 %) / nm	-0.91	-0.78	-0.37	-1.06	-6.8	-9.8	4.9	1.1
Repeatability / nm	0.11	0.03	0.19	0.09	2.0	0.3	3.5	3.5
Reproducibility / nm	0.04	0.03	0.40	0.36	1.6	4.0	5.4	6.0
Traceability / nm	0.90	0.90	0.90	0.90	0.9	0.9	0.9	0.9

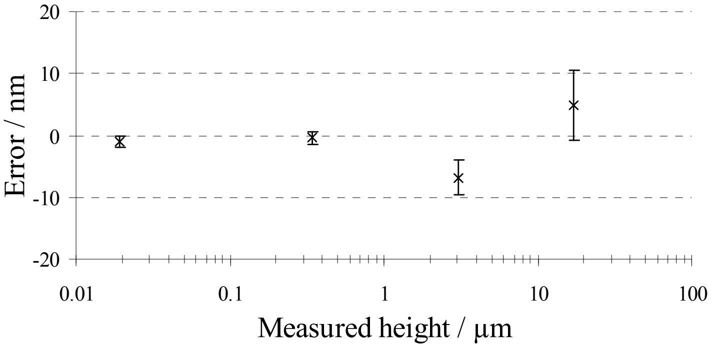

Figure 6.3 Calibration of the *z* axis of the CSI equipped with 20× magnification lenses – error plot

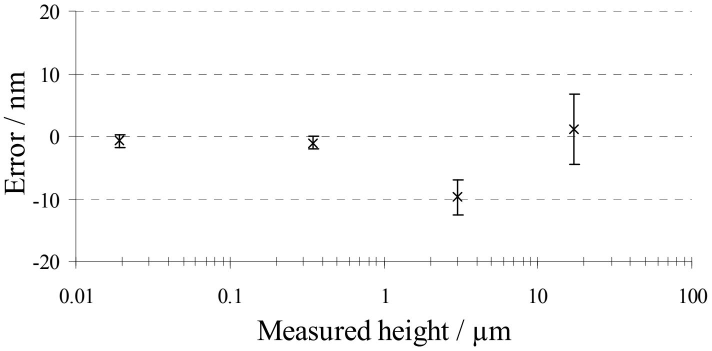

Figure 6.4 Calibration of the *z* axis of the CSI equipped with 50× magnification lenses – error plot

In the ICM case the same experiments were carried out as outlined above for the CSI case. Due to the large flatness errors across the *z* working range of the ICM (10 mm - see chapter 5) the reproducibility values were relatively large to those of the CSI (see table 6.2). In the 20× magnification lens configuration of the ICM, the ISO 5436-1 method failed to provide any results at 90 % of the instrument working range, which would limit the lower value of the certified *z* measurement range to 350 nm above 70 % of the working range of the *z* scale.

Table 6.2 ICM *z* scale calibration results

Nominal height	18 nm		350 nm		3 μm		17 μm	
Magnification objective	20×	50×	20×	50×	20×	50×	20×	50×
Error (at 50 %) / nm	-3.3	1.1	-14.4	-5.7	-13.5	5.3	-16.2	6.0
Repeatability / nm	0.4	0.3	2.3	1.0	3.3	3.8	7.6	10.4
Reproducibility / nm	4.6	6.4	8.7	9.0	17.4	10.8	13.7	14.3
Traceability / nm	0.9	0.9	0.9	0.9	0.9	0.9	0.9	0.9

The results presented in table 6.2 do not provide a true reflection of the quality of the *z* scale, but reflect the effect of the residual flatness on the height standard measurement. A way around this issue consists of measuring a reference flat at each of the five locations in the instrument range that were used to measure the height standards, then subtract the measured topography of the flat from the corresponding measured topography of the height standards (see table 6.3). Table 6.3 shows improved reproducibility in the measurement of the 18 nm height standard for both magnification lenses, and on the 350 nm standard for 20× magnification lens. In addition, the calibration is valid for the whole working range of the instrument.

The ICM error plots, after flat correction, are presented in figure 6.5 and figure 6.6 corresponding to 20× and 50× magnification lenses respectively.

Unlike the CSI case, where the calibration of the *z* scale provided similar results for both 20× and 50× magnification lenses (see figure 6.3 and figure 6.4), the *z* calibration results for the two lenses of the ICM show different error trends (see figure 6.5 and figure 6.6), which could be explained by the effect of different vertical scanning speeds and the number of confocal planes between the two lens configurations.

Table 6.3 ICM *z* scale calibration results - flat corrected

Nominal height	18 nm		350 nm		3 µm		17 µm	
Magnification objective	20×	50×	20×	50×	20×	50×	20×	50×
Error (at 50 %) / nm	0.1	0.4	-11.3	-5.7	-10.1	5.3	-16.2	6.0
Repeatability / nm	0.6	0.2	2.3	1.0	3.3	3.8	7.6	10.4
Reproducibility / nm	1.8	1.0	6.6	9.0	17.3	10.8	13.7	14.3
Traceability / nm	0.9	0.9	0.9	0.9	0.9	0.9	0.9	0.9

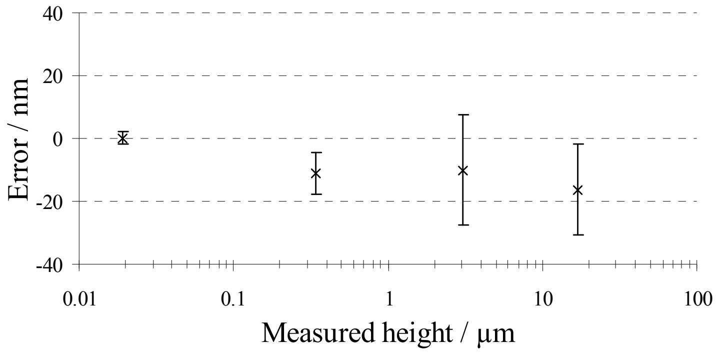

Figure 6.5 Calibration of the *z* axis of the ICM equipped with 20× magnification lenses – error plot after flat correction

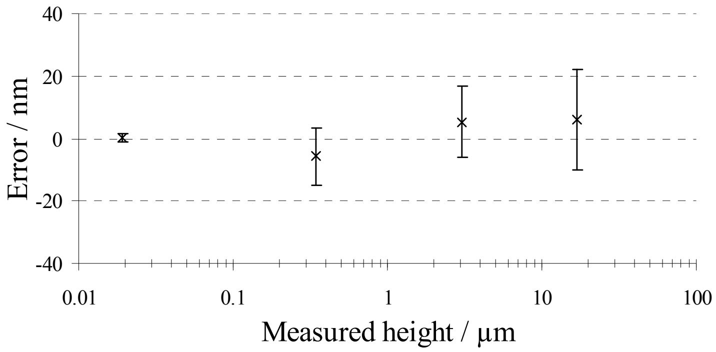

Figure 6.6 Calibration of the *z* axis of the ICM equipped with 50× magnification lenses – error plot after flat correction

Five repeated measurements at each of the five positions inside the instruments' working range could be a lengthily task. Instead one measurement at each of the five positions inside the instruments working range (10 %, 30 %, 50 %, 70 % and 90 % of the instrument working range) can be performed because the measurement repeatability will be included in the reproducibility term.

Instruments that use *xy* raster scanning method should have the fast axis oriented nominally perpendicular to the groove length of the height standard (stylus and ICM case). In this orientation of the height standard relative to the fast axis of the instrument, the effect of the flatness errors of the slow axis on the height measurement will be minimised.

The stylus instrument measurement results are presented in table 6.4. Unlike the two optical instruments, the calibration of the stylus instruments was performed only in the centre of the working range of the *z* scale, such that the reproducibility was not calculated.

Table 6.4 Stylus instrument *z* scale calibration results

Nominal height	18 nm	350 nm	3 µm	17 µm
Error (at 50 %) / nm	1.5	11.6	99.7	547.2
Repeatability / nm	0.5	0.1	0.7	2.1
Traceability / nm	0.9	0.9	0.9	0.9

The calibration of the *z* scale of the stylus instrument (see figure 6.7) shows an amplification coefficient significantly different from unity. Unlike in the CSI and ICM cases where the amplification coefficients do not necessarily need to be corrected, the amplification coefficient of the stylus instrument has to be adjusted.

The amplification coefficient can be calculated using equation 6.1

$$\alpha = \frac{\sum_i^n C_i I_i}{\sum_i^n C_i^2}, \qquad 6.1$$

where α is the amplification coefficient, C_i is the calibrated value, I_i is indicated value and *n* represents the number of different height standards used.

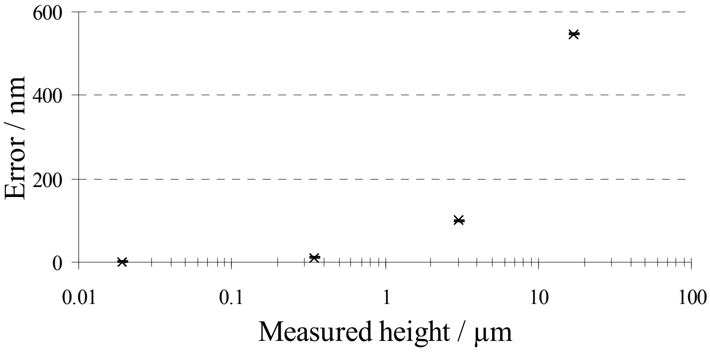

Figure 6.7 Calibration of the *z* axis of the stylus – error plot

The amplification coefficient of the *z* scale of the stylus instrument was found to be 1.032 18. The slope correction does leave an absolute residual error, which is a measure of linearity of the *z* scale – l_z, in excess of 2.1 nm (see figure 6.8).

The perpendicularity between the areal reference and the *z* axis can be determined by measuring the pitch of a periodic structure mounted at different angles relative to the instrument's areal reference (Xu 2008). If the *z* axis scale is not perpendicular to the areal reference the pitch will change according to the angle between the areal reference and the step height surface. On the other hand, the calibration of the *z* axis scale with multiple step height artefacts can correct for the perpendicularity errors. The cosine error that is introduced by the *z* axis scale perpendicularity behaves as an amplification error.

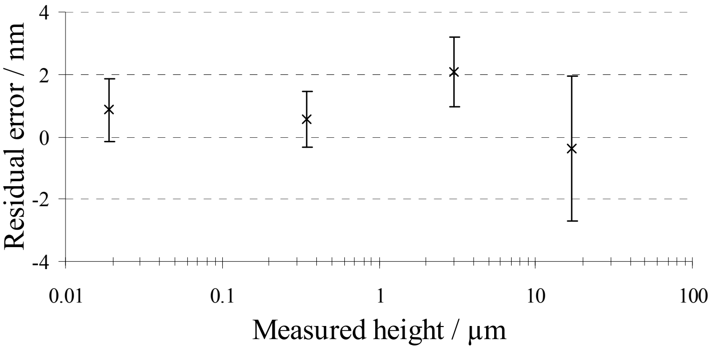

Figure 6.8 Calibration of the *z* axis of the stylus – residual error plot

6.2 x and y scale

Often pitch measurements on sinusoidal artefacts are used to estimate the characteristics of the *x* and *y* scales. Such measurements are not sufficient to fully satisfy the requirements of the scale calibration because only information about the amplification coefficient can be obtained. The *x* and *y* axes amplification and the perpendicularity can be measured using a calibrated (using traceable areal surface topography measuring instruments - Leach and Giusca 2009, Thomsen-Schmidt and Krüger-Sehm 2008) areal cross-grating artefact (Leach *et al.* 2006) or pyramidal structures (Ritter *et al.* 2007), for example.

Using a calibrated cross-grating artefact, both amplification coefficient and linearity errors of the *x* and *y* axes were estimated by measuring the positions of the centre of gravity of the squares of the cross gratings. In addition the angle between two nominally orthogonal rows of square holes of the cross-grating artefact can be used to measure the perpendicularity between the *x* and *y* axes. Although the centre of gravity analysis method is not commonly used in surface texture analysis software, this method can be easily implemented by the instrument manufactures as additional modules.

Two cross-gratings were used to calibrate the scales of the test instruments; a 100 µm pitch cross-grating was used to calibrate the stylus instrument and the optical instruments in the 20× magnification lens configuration, and a 30 µm pitch cross-grating was used to calibrate the 50× magnification lens configuration of the optical instruments. Both cross-gratings were initially calibrated using the NPL Areal Instrument (see chapter 2).

In order to minimise the effect of the scales cross-talking, the cross-gratings were oriented such that rows of squares were as parallel as possible to the *x* and *y* axis of operation of the test instruments. A five degrees misalignment of the cross-grating axis to the *x* and *y* axes of the instrument under test will have no effect in terms of measurement uncertainty contribution of one axis of the instrument to another if the measurement uncertainties associated with the *x* and *y* scales of the instrument are comparable. That is not to say that the contribution of one axis, say the *y* axis, has to be excluded completely from the measurement of the cross-grating along of the other axis, say the *x* axis, and *vice versa*.

A feature identification algorithm should be used to isolate the square holes. The position of the centre of gravity of the square holes in the *x* direction can be calculated, for example, using the equation 6.2.

$$x_i = \frac{\sum_j x_{ij} z_{ij}}{\sum_j z_{ij}}, \qquad 6.2$$

where x_i is the position of the centre of gravity of the *i*-th hole along the *x* axis, (x_{ij}, z_{ij}) is the location of the *j*-th measured point on the *i*-th holein the *xz* plane.

The CSI measurement results at 10 %, 30 %, 50 %, 70 % and 90 % of the instrument vertical working range were compared to the values reproduced by the calibrated cross-grating artefacts. At each of the five positions the cross-grating artefacts were measured only once. The 20× magnification lens results are presented in figure 6.9 and figure 6.10. The error bars are a combination of the measurement reproducibility and the calibration standard uncertainty of the cross-grating standards (see section 6.3). Both the *x* and *y* axes of the CSI present similar error trends, which could be improved by adjusting the scales using a common amplification coefficient.

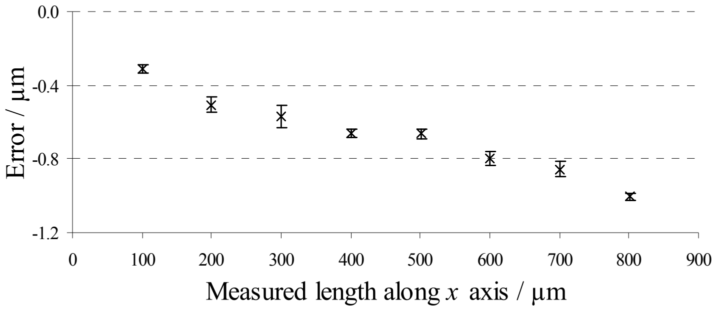

Figure 6.9 Calibration of the *x* axis of the CSI equipped with 20× magnification lenses – error plot

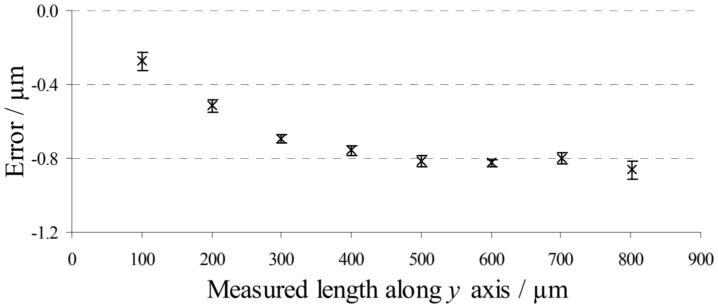

Figure 6.10 Calibration of the *y* axis of the CSI equipped with 20× magnification lenses – error plot

Using equation 6.1, the *x* and *y* axis amplification coefficients were found to be 0.998 638 and 0.998 631 respectively. If both axes are to be corrected with the average amplification coefficient (0.998 635) the absolute residual error does not exceed 0.3 µm (see figure 6.11 and figure 6.12).

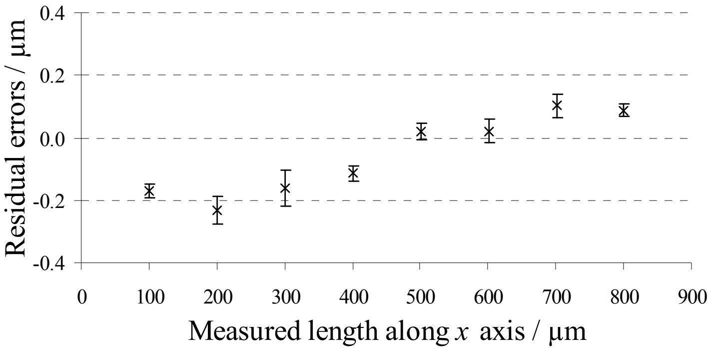

Figure 6.11 Calibration of the *x* axis of the CSI equipped with 20× magnification lenses – residual errors after correcting the results using the 0.998 635 amplification factor

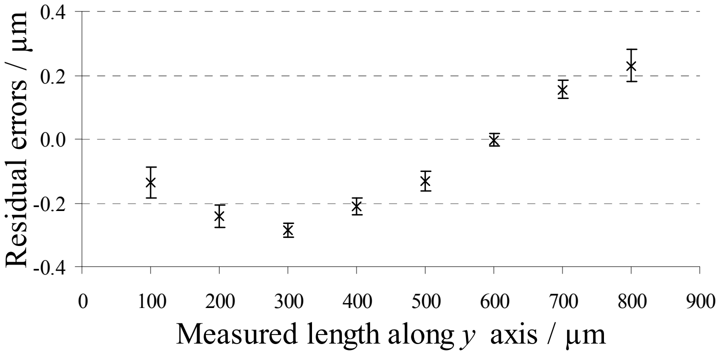

Figure 6.12 Calibration of the *y* axis of the CSI equipped with 20× magnification lenses – residual errors after correcting the results using the 0.998 635 amplification factor

The calibration of the 50× magnification lens found the amplification coefficients of the *x* and *y* scale to be 0.999 832 and 1.000 329 respectively (see figure 6.13 and figure 6.14). There is no need to correct the scales using an average amplification coefficient because it will not produce a significant improvement of the quality of the scales.

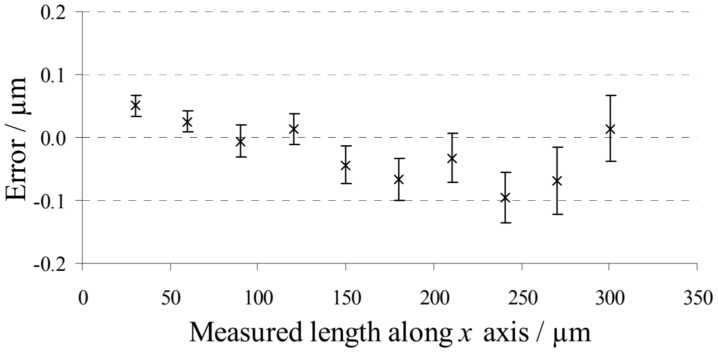

Figure 6.13 Calibration of the *x* axis of the CSI equipped with 50× magnification lenses – error plot

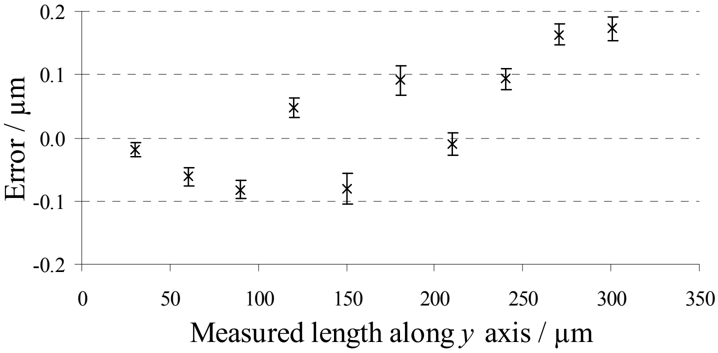

Figure 6.14 Calibration of the *y* axis of the CSI equipped with 50× magnification lenses – error plot

In the CSI case the linearity and amplification errors are smaller, or at least comparable to, the pixel size, or to the optical resolution, of the instrument. In similar calibration conditions the ICM results for both 20× and 50× magnification lenses show that the *x* and *y* amplification coefficients are on the opposite sides of unity (see figure 6.15 and figure 6.16), such that a common correction factor for *x* and *y* scales will not improve the quality of the scales.

Instead one common amplification coefficient for the *x* scale and another for the *y* scale can be used to improve the readings of the instruments in both lens configurations. This is possible because the difference between the calculated amplification coefficients of one scale, either *x* or *y*, in the two magnification lens configurations is within the measurement uncertainties associated with the amplification coefficient calculation (see section 6.3).

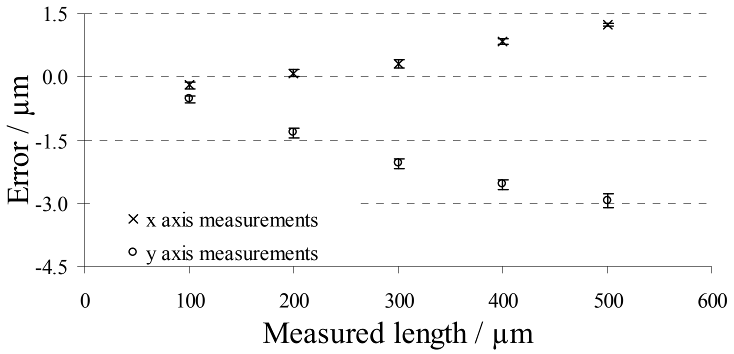

Figure 6.15 Calibration of the axes of the ICM equipped with 20× magnification lenses – error plot

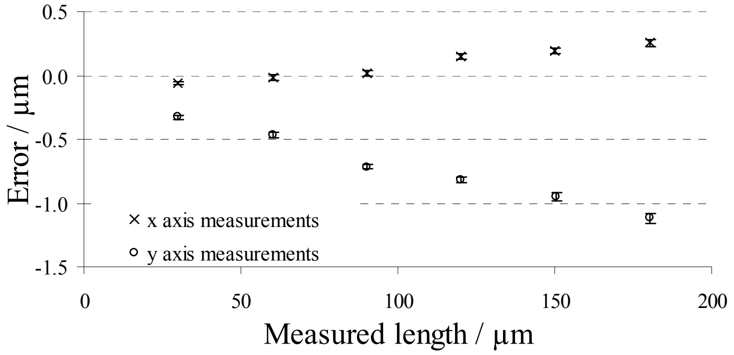

Figure 6.16 Calibration of the axes of the ICM equipped with 50× magnification lenses – error plot

Correcting the readings of the *x* scale of the ICM, of the magnification lens used, using an amplification coefficient equal to 1.001 90 will generate a linearity error in excess of 500 nm in the 20× configuration (see figure 6.17) and 120 nm in the 50× configuration (see figure 6.18). In the same way, an amplification coefficient of 0.993 57 will produce a linearity error smaller than 300 nm in the 20× configuration (see figure 6.19) and 140 nm in the 50× configuration (see figure 6.20).

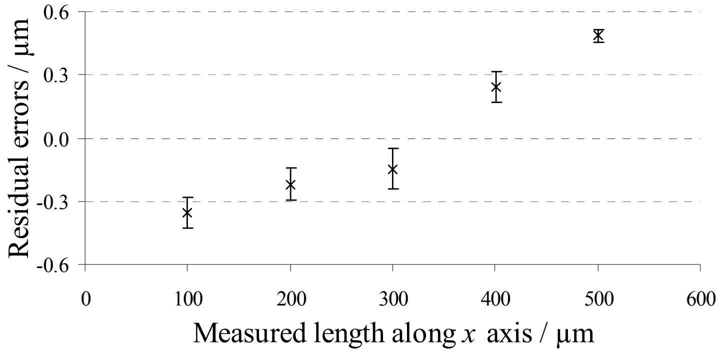

Figure 6.17 Calibration of the *x* axis of the ICM equipped with 20× magnification lenses – residual errors after correcting the results using the 0. 1.001 90amplification factor

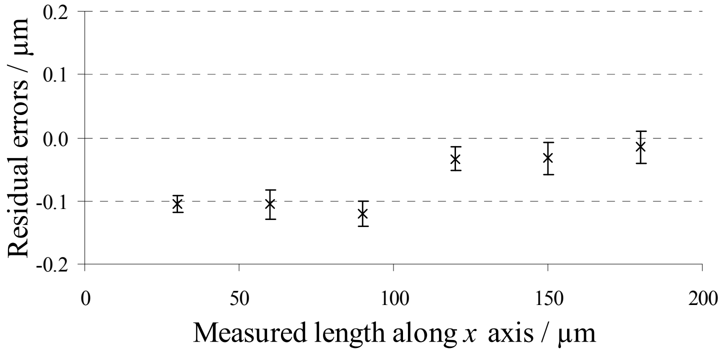

Figure 6.18 Calibration of the *x* axis of the ICM equipped with 50× magnification lenses – residual errors after correcting the results using the 1.001 90 amplification factor

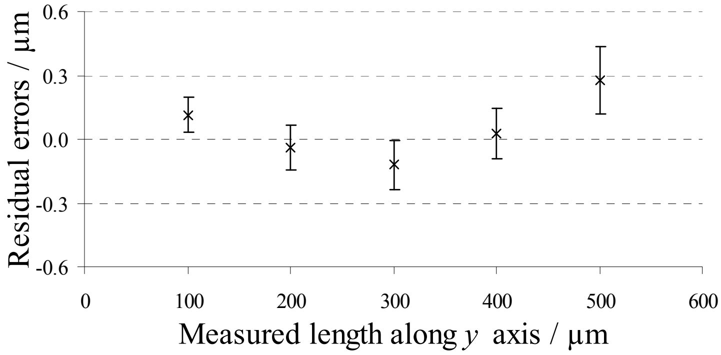

Figure 6.19 Calibration of the *y* axis of the ICM equipped with 20× magnification lenses – residual errors after correcting the results using the 0.993 57 amplification factor

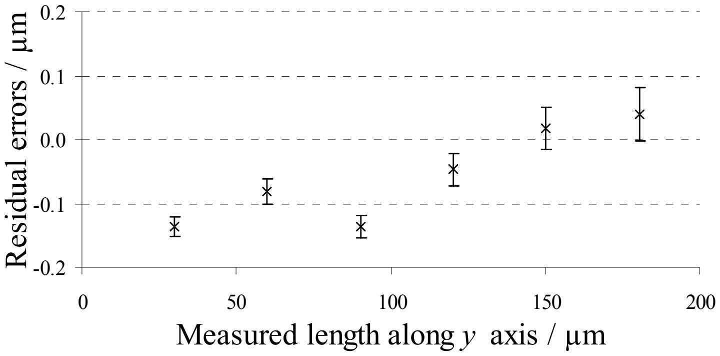

Figure 6.20 Calibration of the *y* axis of the ICM equipped with 50× magnification lenses – residual errors after correcting the results using the 0.993 57 amplification factor

The calibration of the lateral scale of the stylus instrument consisted of five repeated measurements performed only in the centre of the working range (*x*, *y* and *z*) of the instrument. The results of the *x* scale calibration found an amplification coefficient close to unity, which does not necessarily need to be adjusted (see figure 6.21). In contrast the amplification coefficient of the *y* scale is approximately 13 % larger than the ideal amplification coefficient while the linearity errors will not exceed 4 µm (see figure 6.22).

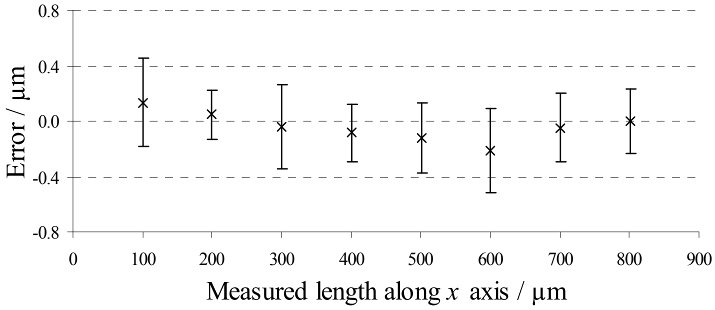

Figure 6.21 Calibration of the *x* axis of the stylus instrument – errors plot

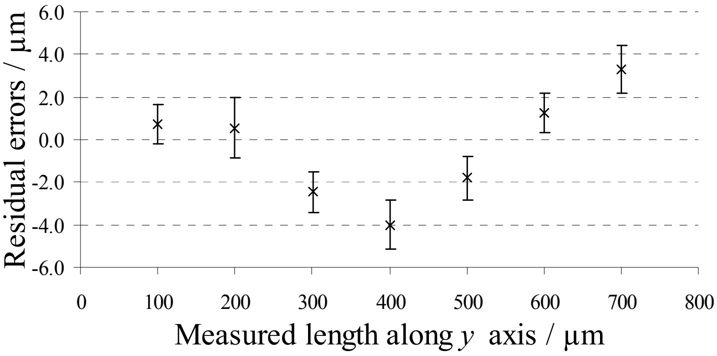

Figure 6.22 Calibration of the *y* axis of the stylus instrument – residual errors after correcting the results using the 1.126 09 amplification factor

The perpendicularity of the *x* and *y* axes can be determined by measuring the angle between two nominally orthogonal rows of square holes whose perpendicularity is known. The orientation of each row of squares can be calculated by fitting a line though the centre of gravity of the corresponding squares.

Using the same cross-grating results used to calculate the amplification and linearity, the absolute perpendicularity error between the *x* and *y* axes was calculated. The absolute perpendicularity errors were found to be smaller than 0.03º, 0.3º and 1.1º for CSI, ICM and stylus respectively. The maximum effect of these perpendicularity errors corresponds to errors of 0.000 014 %, 0.001 4 % and 0.02 % of measured length. Therefore, for a measured length of 1.4 mm, which is a diagonal measurement in the 1 mm ×1 mm area, the cosine errors translate in an absolute length error of 0.2 nm, 20 nm and 0.25 µm respectively. The magnitude of the effect of the cosine errors to the length measurements is at least ten times smaller than the linearity errors, such that they do not have to be taken into account during the calculation of the measurement uncertainties (for the instruments used here).

6.3 Measurement uncertainty

There are two ways to account for the contribution of the amplification of the scales to the measurement uncertainty. The first way is to split the contribution of the amplification coefficient from the contribution of the linearity, which can be inconvenient, as it requires uncertainty propagation using the equation of the line fit. The second way is to consider the combined effect of the amplification coefficient and scale linearity. In this way the uncertainty contribution of the magnification of the scales will be given by the largest error that is measured against a calibrated line scale.

The measurement errors (δ_{error}) contribution to the measurement uncertainty is propagated in the form of a rectangular distribution that has a variance equal to the square of the value of the error divided by three (BIPB 2008a). The repeatability (δ_{repeat}) and reproducibility (δ_{reprod}) contribution to the overall measurement uncertainty is propagated in the form of a normal distribution that has an expectation equal to zero and a variance equal to the square of the value of the repeatability. The combined effect of the measurement errors, traceability, repeatability and/or reproducibility on the co-ordinate measurement standard uncertainty $u_{T\text{-}x}$, $u_{T\text{-}y}$ and $u_{T\text{-}z}$ is given by

$$u_{T-i} = \sqrt{u_{\text{traceability}}^2 + \delta_{\text{repeat}}^2 + \delta_{\text{reprod}}^2 + \frac{\delta_{\text{error}}^2}{3}}\,, \qquad 6.3$$

where $i = \{x, y, z\}$.

A summary of the standard measurement uncertainties associated with the calibration of the *z* scale of the all three instruments used as test cases are presented in table 6.5. In comparison to the optical instruments, the stylus instrument has lower linearity errors that allow the z scale calibration contribution to the standard measurement uncertainty to be below 3 nm throughout the calibrated range, when the *z* scale amplification is adjusted. Starting with 3 µm and above, the *z* scale calibration contribution of the CSI to the standard measurement uncertainty is dominated by the linearity errors, whereas in the ICM case the repeatability and reproducibility have equal magnitude.

Table 6.5 Summary of the standard measurement uncertainties associated with the calibration of the *z* scale

Nominal height	CSI		ICM		Stylus	
	20×	50×	20×	50×	unadjusted	adjusted
	$u_{\mathrm{T}\text{-}z}$ / nm^{-1}					
18 nm	1.0	1.0	2.1	1.4	1.3	1.1
350 nm	1.0	1.2	10	10	7	1.0
3 μm	5	7	19	12	58	1.6
17 μm	7	7	18	18	316	2.3

Summaries of the standard measurement uncertainties associated with the calibration of the lateral scales of the all three instruments used as test cases are presented in table 6.6 and table 6.7.

Table 6.6 Summary of the standard measurement uncertainties associated with the calibration of the lateral scales when 30 μm cross-grating was used

Nominal length	CSI 50×		ICM 50×$^{\text{adjusted}}$	
	$u_{T\text{-}x}$	$u_{T\text{-}y}$	$u_{T\text{-}x}$	$u_{T\text{-}y}$
	$\mu\mathrm{m}^{-1}$			
30	0.03	0.02	0.06	0.08
60	0.02	0.04	0.05	0.04
90	0.03	0.05	0.05	0.07
120	0.03	0.03	0.02	0.03
150	0.04	0.05	0.03	0.04
180	0.05	0.06	0.04	0.06
210	0.04	0.02		
240	0.07	0.06		
270	0.07	0.10		
300	0.05	0.10		

Table 6.7 Summary of the standard measurement uncertainties associated with the calibration of the lateral scales when 100 µm cross-grating was used

Nominal length	CSI 20× $^{\text{adjusted}}$		ICM 20× $^{\text{adjusted}}$		Stylus	
	$u_{T\text{-}x}$	$u_{T\text{-}y}$	$u_{T\text{-}x}$	$u_{T\text{-}x}$	$u_{T\text{-}x}$	$u_{T\text{-}y}^{\text{adjusted}}$
			μm^{-1}			
100	0.10	0.09	0.24	0.10	0.33	1.0
200	0.14	0.14	0.19	0.12	0.18	1.5
300	0.11	0.17	0.18	0.16	0.31	1.7
400	0.07	0.12	0.09	0.12	0.21	2.6
500	0.03	0.08	0.17	0.19	0.26	1.5
600	0.04	0.02			0.33	1.2
700	0.07	0.09			0.25	2.2
800	0.06	0.14			0.24	

6.4 Summary

Calibration of the amplification coefficient, linearity and squareness of areal surface topography measuring instruments is often performed using techniques developed for calibration of profile measuring instruments. The calibration of step height artefacts involves the assessment of a small number of profiles, as low as five, such that the measurement uncertainty is strongly affected by the non-uniformity of the artefact. Areal characterization allows an improvement in the measurement uncertainties because it permits for accurate positioning over the calibrated area of the step height artefact and averages the results of a considerably larger number of profiles, if the method of calculating the height of the step height artefact presented in section 6.1 is used.

Currently, the established methods for calibrating the lateral scales of areal instruments are based on pitch measurements that only estimate the local characteristic of the scales and do not give information about the instrument response curves, therefore, they are not suitable to measure the linearity errors. The amplification coefficient and linearity of the lateral axes can be determined by measuring the positions of the centre of gravity of the squares of a calibrated cross-grating artefact. Additionally, the squareness of the *x* and *y* axes can be determined by measuring the angle between two nominally orthogonal rows of square holes by fitting a line though the centre of gravity of the corresponding squares.

The measurement uncertainty associated with the calibration of the scales of the instruments can be calculated using a simple model that accounts for traceability, repeatability, reproducibility and measurement error. The measurement error contribution accounts for both the amplification coefficient and the linearity of the scales.

All three instruments used as test cases have good quality *z* axis scales that potentially allow for nanometre-level measurement uncertainties associated with the measurement of step height artefacts that reproduce larger values than the discrimination threshold of the instruments. The uncertainty associated with the step height measurement can be improved if the measurements are performed at one position inside the calibrated range of the instrument *z* axis scale, because the reproducibility contribution is not taken into account. The contact stylus is capable of standard measurement uncertainties associated with the calibration of the *z* axis scale that are consistently below 3 nm.

7 Resolution

Several factors can influence the resolution of an instrument, either in the *z* direction or in the *x* and *y* directions. The most common influence factor which limits the *z* resolution is the measurement noise. There are instances in which some of the contact stylus instruments, especially those that have large *z* ranges, are restricted by the digitisation step due to the fixed dynamic range. In these instances a simple measurement noise test (see chapter 5) would not be able to estimate the value of the *z* resolution as the root mean square deviation (*Sq*), because the *Sq* value measured on a flat without tilt could be equal to zero. The limiting height digitisation cases are rare nowadays but not unknown, whereas lateral digitisation problems are more often visible due to restrictions in sampling distance that, for example, are given by the limited pixel number of a CCD camera. There are instruments, such as interferometric-based techniques, of which height detection algorithms, supported by measurement strategies, demonstrate sub-nanometre height measurement capabilities, although measurement noise is often ten times higher. Other instruments, which are not capable of resolving very small steps, can resolve steps above a certain height with sub-nanometre accuracy. As demonstrated in the previous two chapters, nanometres accuracy is possible for a restricted range of applications similar to step height measurements or pitch measurements, where the length measurements are taken between known geometrical shapes, such as planes, defined by a series of measured points, which allows a diminished contribution of the measurement noise or of the resolution. However, from the coordinate point measurement perspective, the measurement noise or the resolution plays an important role because they limit the length measurement between two isolated points.

In contrast to the other metrological characteristics discussed in the previous two chapters, the topic of resolution for the areal surface topography measuring instruments is still being discussed in the standards committee, ISO/TC213 working group 16. The debate is fuelled by disagreements in regards to the definition of resolution, which leads to problems in the way resolution is estimated. In practice the resolution along each axis is measured and stated separately. For example, the measurement of the resolution of the *z* axis can be performed on a structure such as a groove several times wider than the lateral resolution of the instrument, decoupling in this way the influence of the lateral resolution from the measurement of the height of the groove. *Vice versa*, lateral resolution tests can be designed in such a way that the instrument can accurately measure the pitch of a periodic structure that is close to the lateral resolution of the instrument with serious loss of vertical accuracy. In this case, the lateral resolution of the instrument is defined as the smallest lateral separation between two points that can be distinguished.

In the *z* resolution case, the general consensus is that only the combination of the *z* scale resolution and of the fitting algorithm, if applicable, is taken into account without any contribution of the lateral component. Therefore, the measurement noise test and/or digitisation contribution are enough to quantify the effect of the *z* resolution from a measurement uncertainty point of view. Otherwise, the effect of the resolution along the *z* axis will be doubly counted in the uncertainty analysis. As discussed above, finding the value of the smallest resolvable step has, to a certain extent, nothing to do with the resolution since some instruments cannot resolve small steps but they still can provide accurate height measurements above a height discrimination threshold (see BIPM 2008c).

In the next section several definitions of the lateral resolution are discussed. Section 7.2 presents a method of estimating the lateral period limit using the measurement of a type ASP material measure. Two examples, one using the a CSI and one using an ICM, of estimating the lateral period limit using a type ASP material measure are presented in sections 7.3 and 7.4. Measurement uncertainty is discussed in section 7.5 and summary of the chapter is presented in section 7.6.

7.1 Definitions and their implementation

ISO/TC213 working group 16 has attempted to produce a new term for resolution specific for areal surface topography measuring instruments. One of the new definitions was for the term *topographic spatial resolution* defined as "*metrological characteristic describing the ability of a surface topography measuring instrument to distinguish closely spaced surface feature".* This definition is closer to the *metrological structural resolution* introduced in VDI/VDE 2617 Part 6 (2005) in which the definition is "*smallest width of a structure, whose measured height agrees with the real height within the specification (e.g. uncertainty of height measurement) of the instrument"* (Krüger-Sehm 2010). Both definitions intend to account for the interrelationship between the vertical and lateral resolution (see chapter 4, equation 4.2).

Recent developments favour the use of the term lateral period limit (D_{LIM}), which was previously defined as "the spatial period of a sinusoidal profile at which the height response of an optical instrument falls to 50%". The latter definition is only applicable to optical instruments, but there was no reason for lateral period limit definition to exclude contact stylus instruments. Therefore, the definition was changed to "the spatial period of a sinusoidal profile at which the height response of an instrument falls to 50%" (ISO/CD 25178–600 2012). In the note of the definition of the lateral period limit, ISO/CD 21578-600 formally recognises definitions related to the lateral resolution that could be adhered to when the measurement of the D_{LIM} is required. In effect, the 2D types of lateral resolution definitions, such as Rayleigh criterion, Sparrow criterion or lateral resolution (see chapter 4), are acknowledged as viable ways of estimating the topographic spatial resolution until a consensus method of testing the 3D resolution becomes available. The list of terms also includes: stylus tip radius (ISO 25178-601); width limit for full height transmission (ISO 25178–601); topographic spatial resolution; and instrument transfer function.

The instrument transfer function (ITF) provides the instrument height response at different spatial frequencies. For stylus instruments the ITF has been studied but for optical systems this is in its infancy (de Lega and de Groot 2012).

Both stylus radius and the width limit for full height transmission have been defined (ISO 25178-601 2010) for stylus instruments. The implementation of the width limit for full height transmission definition requires a material measurement standard similar to type PGR or ACG (see chapter 3). These types of material measurement standards are characterised by sharp vertical edges that optical instruments often cannot measure without errors.

de Lega and de Groot (2012) identify five lateral resolution definitions that are applicable to optical instruments used as areal surface topography measuring instruments. These lateral optical resolution definitions include Rayleigh criterion for incoherent illumination, Sparrow limit for coherent and incoherent illumination and Abbe criterion for coherent and incoherent illumination (see chapter 4). Resolution measurement tests require physical measurement standards that have been mainly developed for incoherent systems (Foreman *et al.* 2012). However, the illumination conditions (coherent or incoherent) necessary for the above mentioned criteria to be applicable are rarely met in practice, which make their practical implementation problematic (de Lega and de Groot 2012).

The lateral period limit can be measured using sinusoidal material measures with different pitches, often with the same amplitude, from which the spatial wavelength corresponding to a 50 % drop in amplitude can be found. Such an artefact has been produced in a form of the chirped artefact (Krüger-Sehm *et al.* 2007, Fujii *et al.* 2011). A 3D Siemens star, ASG type physical measurement standard (ISO/FDIS 25178-70 2012), can be used to find the approximate value of the spatial period at which the height response of an instrument falls to 50 % (Leach 2006, Sun and Weckenmann 2011). Unlike the material measures that are capable to reproduce a discrete series of spatial wavelengths, frequently unidirectional, 3D stars generate a continuum of wavelengths that test the resolution in all lateral directions, such that it is potentially a good lateral resolution standard.

The following section presents a novel method of measuring the resolution of areal surface topography measuring instruments.

7.2 Type ASG analysis

Type ASG material measures can be used to measure the resolution of areal instruments in a way compliant with the definition of lateral period limit. Note that the lateral period limit definition calls on a sinusoidal type of material measure, whereas the material measure used in this chapter has a rectangular profile. However, the analysis method proposed in this paragraph can be used on a type ASP that has a sinusoidal profile.

Often the star patterns are assessed using circular profiles of different diameters centred on the apex of the star (see figure 7.1, Wekenmann 2009). However, circular profiles are limited to a discrete series of pitch values.

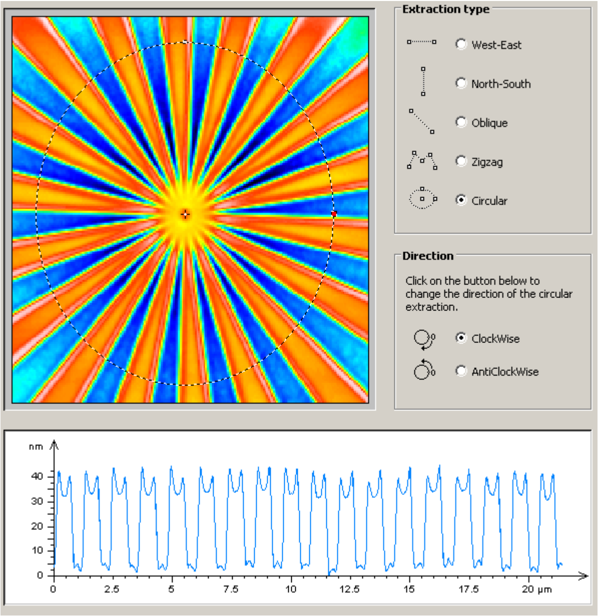

Extraction type

○ West-East
○ North-South
○ Oblique
○ Zigzag
● Circular

Direction

Click on the button below to change the direction of the circular extraction.

● ClockWise
○ AntiClockWise

Figure 7.1 Example of circular profile extraction on a type ASG material measure. Batwing like effect present on the extracted profile is produced during manufacturing process

One way of fully exploiting the advantage of type ASG material measures is to assess the star-pattern with profiles that are extracted along the radius of the star. To find the 50 % fall in the height response of an instrument, two profiles are required. One is extracted through the centre of two diametrically opposed raised petals (see figure 7.2 left) and one running through the centre of two diametrically opposed lowered petals (see figure 7.2 right). The two profiles should be extracted from adjoining raised and lowered petals.

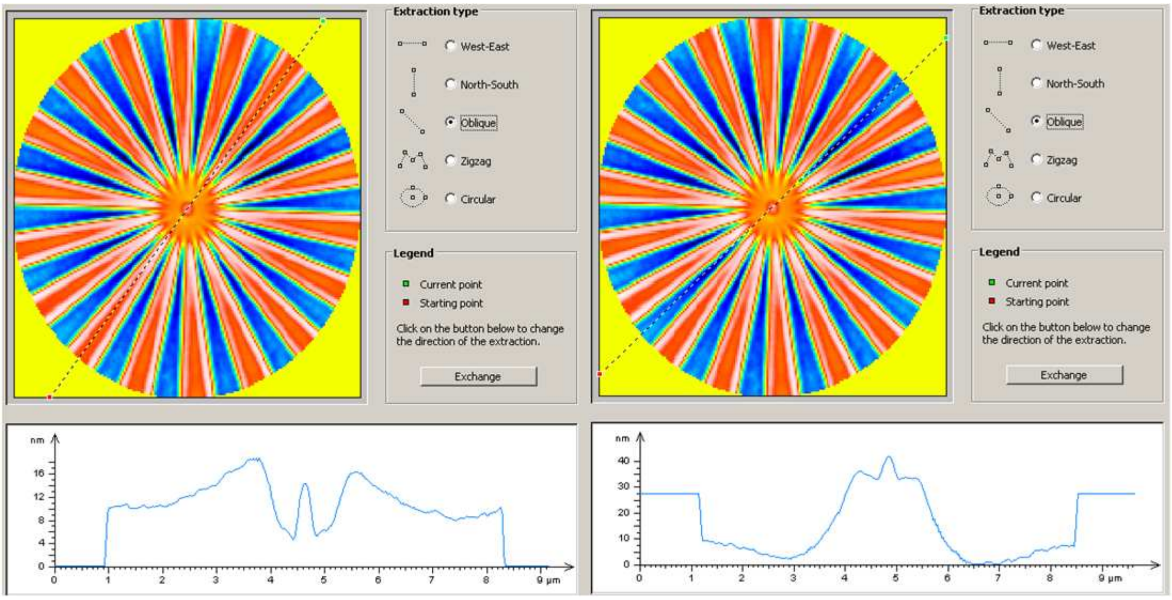

Extraction type
○ West-East
○ North-South
● Oblique
○ Zigzag
○ Circular

Legend
🟩 Current point
🟥 Starting point
Click on the button below to change the direction of the extraction.

Extraction type
○ West-East
○ North-South
● Oblique
○ Zigzag
○ Circular

Legend
🟩 Current point
🟥 Starting point
Click on the button below to change the direction of the extraction.

Figure 7.2 Example of linear profile extraction: left - profile extracted through the middle of two diametrically opposed raised petals; right - profile extracted through the middle of two diametrically opposed lowered petals

The profile resulting from subtracting the height difference between the raised petals and lowered petals (see figure 7.3), called from now on the instrument response profile (IRP), allows the measurement of the resolution of the instrument.

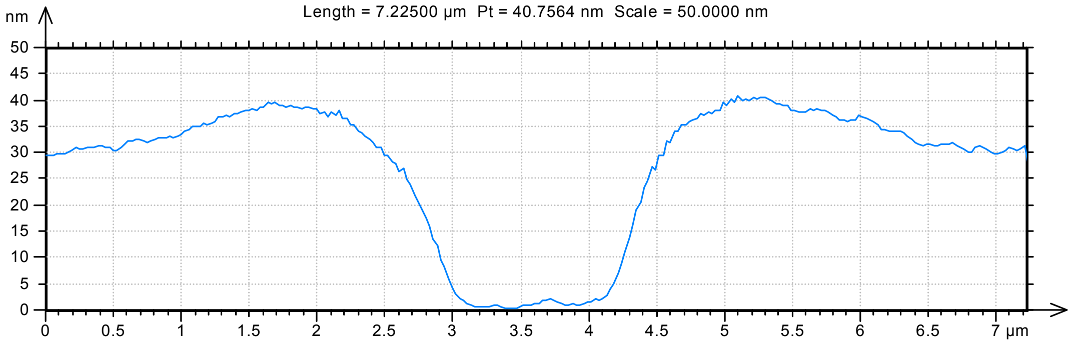

Figure 7.3 Height difference between the raised petals and lowered ones (optical response profile)

As the profiles cross the apex of the type ASG material measure, the height difference drops, highlighting the loss of lateral resolution. To find out what the resolution of the instrument is based on the lateral period limit definition, the vertical scale of the IRP is normalised to the maximum height value and the lateral scale is divided by π / 18 (see figure 7.4), where 18 is the number of raised or lowered petals, resulting in the normalised IRP.

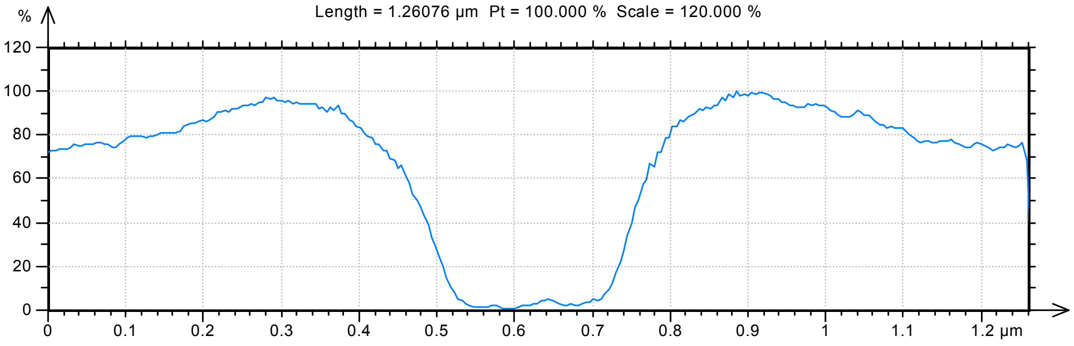

Figure 7.4 Normalised IRP

The resolution of the instrument is given by the width of the central depression at 50 % (see Figure 7.5).

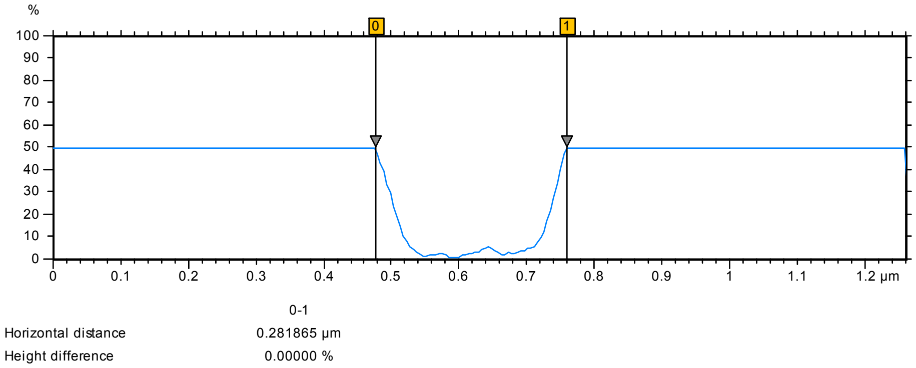

Figure 7.5 Example of measurement of the resolution at 50 % cut-off

The data used to produce figure 7.1 to figure 7.5 were measured using an atomic force microscope. Figure 7.5 suggests that the sample can be used to measure lateral resolution larger than 0.28 µm. The summits flanking the depression are coming from the manufacturing process, which in this case was focus ion beam milling, and they are not caused by a measurement error.

7.3 CSI example

An example of the measured topography of the type ASG material measure using the CSI instrument in the 20× magnification lens configuration is shown in figure 7.6 - left and with the 50× magnification lens presented in figure 7.6 - right. Both images presented in figure 7.6 are not representations of the full field of view of the instrument but they are circular digital zooms of 30 µm radius.

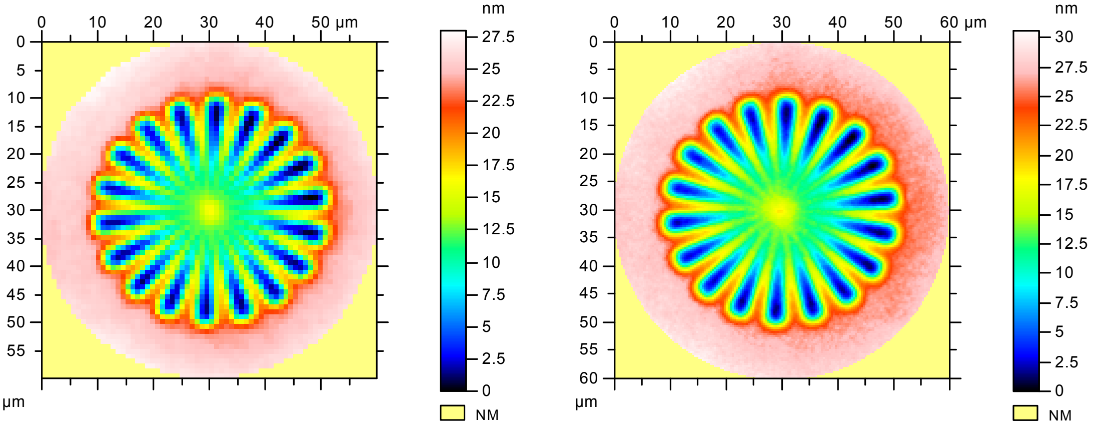

Figure 7.6 CSI measurement of the type ASG material measure: left - 20× magnification lens results; right - 50× magnification lens results

According to the instrument specification, the resolution of the 20× magnification lens theoretically is limited by the pixel size, which is 879 nm, whereas for the resolution of the 50× lens is limited by the optical resolution, which is 665 nm (based on the Raleigh criterion – the pixel size was approximately 350 nm).

The lateral period limit is larger than 4 µm with both magnification lenses (see figure 7.7 and figure 7.8).

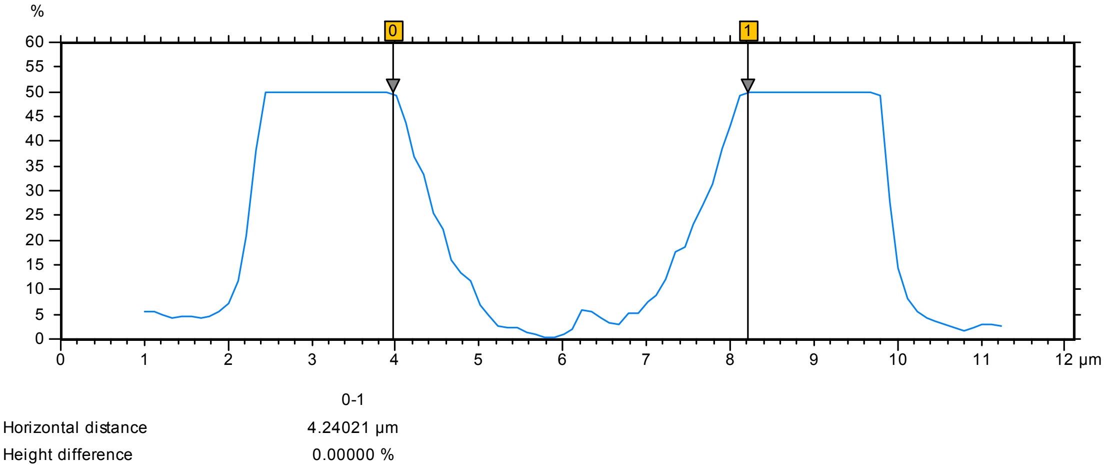

	0-1
Horizontal distance	4.24021 µm
Height difference	0.00000 %

Figure 7.7 Measurement of the resolution at 50 % cut-off of the CSI width 20× magnification lens

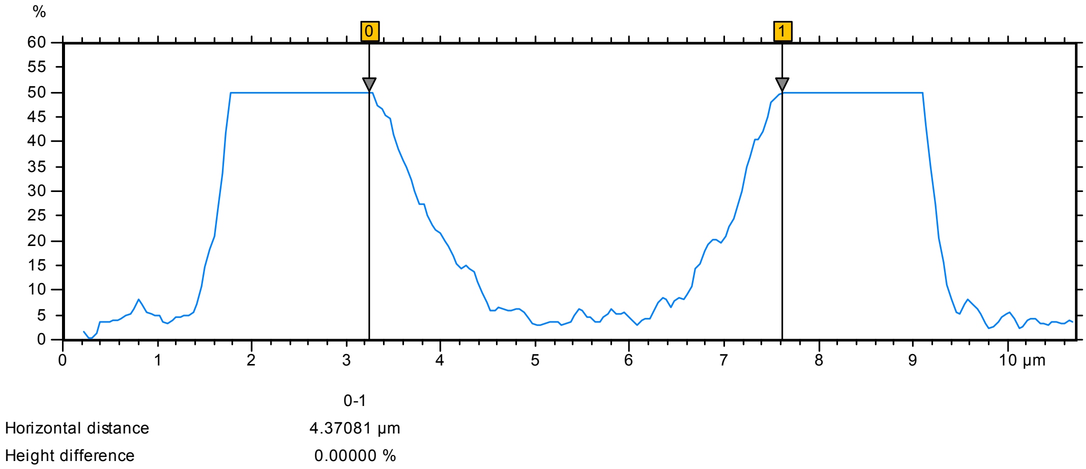

	0-1
Horizontal distance	4.37081 µm
Height difference	0.00000 %

Figure 7.8 Measurement of the resolution at 50 % cut-off of the CSI width 50× magnification lens

These results suggest that the practical numerical aperture of the 50× magnification lens is approximately 0.09 instead the indicated 0.6 value. The low value of the practical numerical aperture was reconfirmed by measurements of a mercury droplet (see figure 7.9) of approximately 77 µm radius. Due to large surface tension value of the mercury, the mercury droplets can be considered to be perfect spheres such that simple topography measurements of the droplet can provide quick indications of the numerical aperture (Mandal *et al.* 2012, Hiemenz and Rajagopalan 1997). In figure 7.9 it can be seen that only a small portion of the ball was resolved correctly as 2π errors surround the top of the sphere.

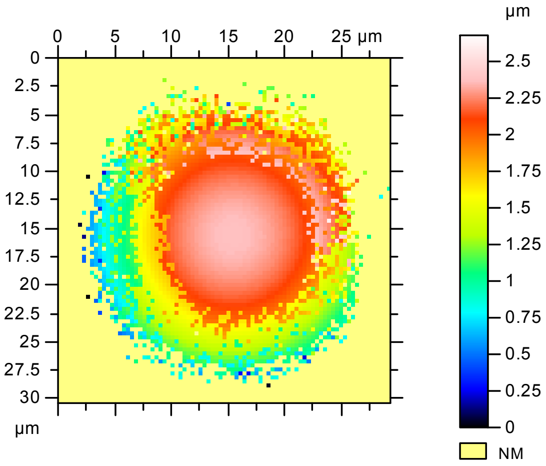

Figure 7.9 CSI measurement of a mercury droplet using 50× magnification lens

A simple profile extraction (see figure 7.10) can highlight the 2π errors (Gao *et al.* 2008) and, subsequently, allow identification of a region of the sphere that is measured correctly.

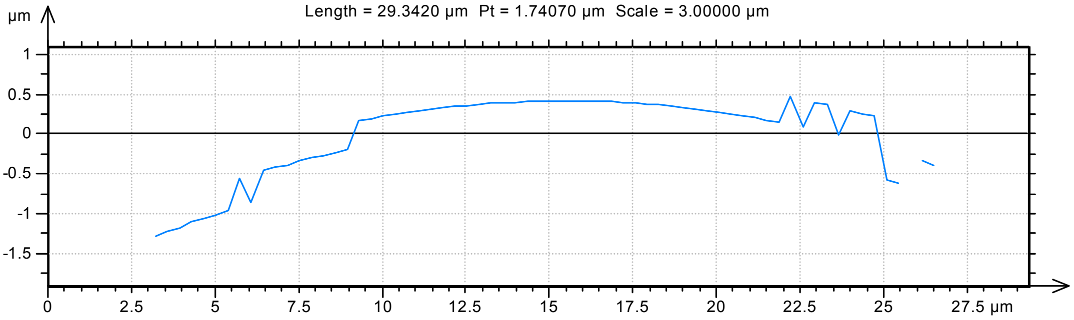

Figure 7.10 Profile extracted across the top of the mercury droplet

Only a central region of 12 µm was measured appropriately. Using the height and the length of the profile of the region that was measured without 2π errors, a numerical aperture of 0.08 was obtained that was close to the numerical aperture value given by the ARS measurement of 0.09. The 2π errors are caused most probably by misalignment of the optical components of the interferometer.

The results from a different CSI that was equipped with an adjustable 50× magnification lens are presented in figure 7.11. The magnification lens in this case is designed such that optimal position of the reference mirror can achieved. The results show an improvement of nearly three times compared to the 50× magnification lens resolution, which is presented in figure 7.8.

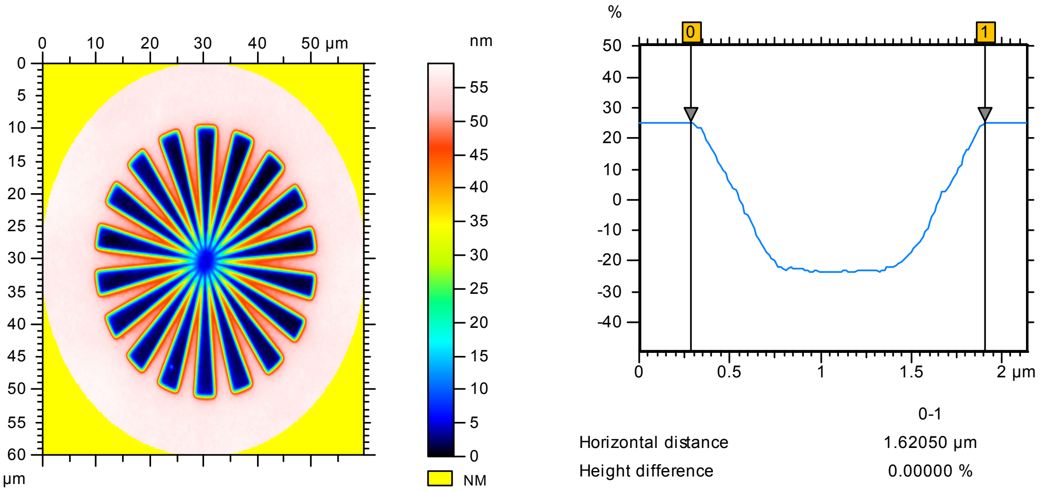

Figure 7.11 CSI measurement of the type ASG material measure using a 50× magnification lens with adjustable reference mirror: left – topography results; right – measurement of the resolution

7.4 ICM example

The ICM measurement results for the 20× magnification lens configuration are shown in figure 7.12 - left and with 50× magnification lens are presented in figure 7.12 - right.

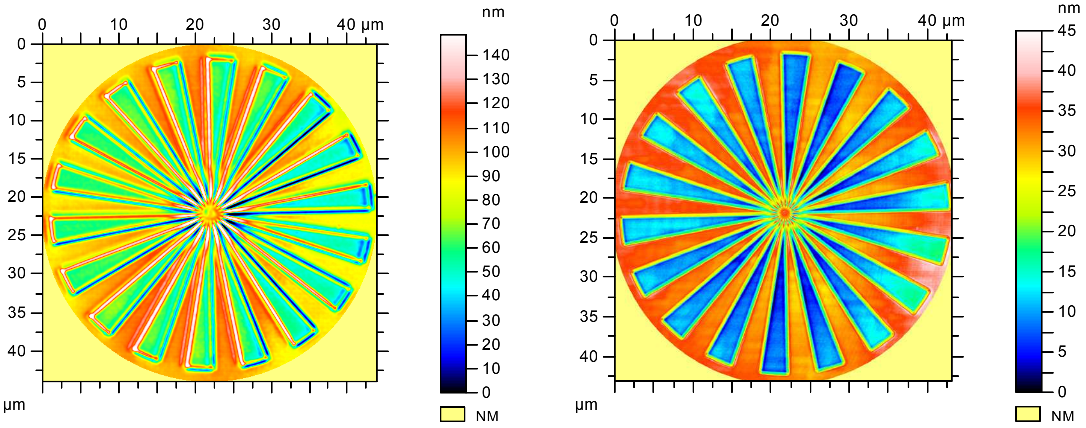

Figure 7.12 ICM measurement of the type ASG standard: left - 20× magnification lens results; right - 50× magnification lens results

The ICM can zoom without reducing the number of topography points (optical zoom) unlike the case of the instruments that use a CCD camera (CSI example). Hence the optical resolution of the instrument can be tested and not the instrument resolution, which can be governed by sampling conditions or Nyquist limit respectively. The nominal sampling distance was 80 nm for the 20× measurement results presented in figure 7.12 - left and 40 nm for the 50× measurement results presented in figure 7.12- right.

The IRPs for ICM 20× and 50× magnification lenses, presented in figure 7.13 and figure 7.14, are W shaped in the central area. The W shape in the centre is attributed to some defocusing problems of the instrument (Fujii *et al.* 2010). The fine detail obtained by zooming into the apex of the measured ASP pattern reveals that the bottom and the top of the petals are inverted in the vertical direction. The inversion takes place at around 2.4 µm away from the apex of the star (see figure 7.15).

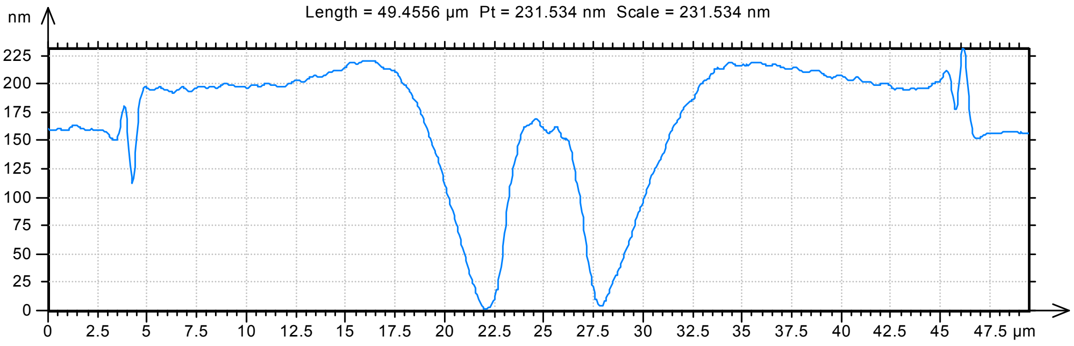

Figure 7.13 IRP – 20× magnification lens

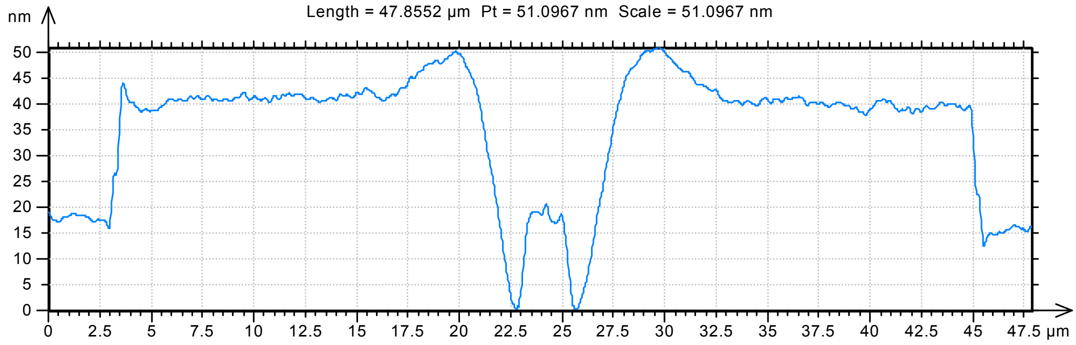

Figure 7.14 IRP – 50× magnification lens

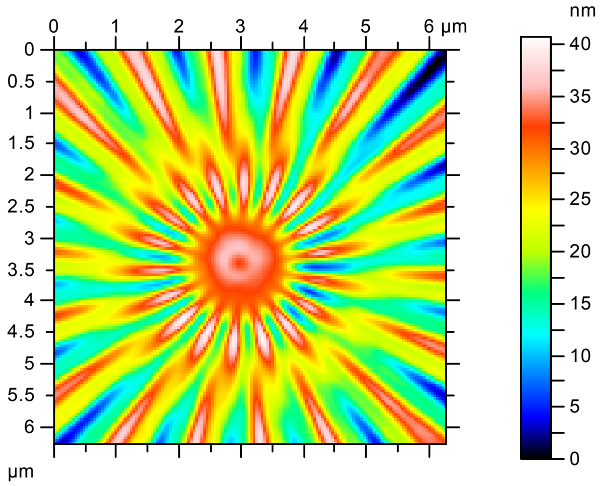

Figure 7.15 ICM measurement of the type ASG standard using 50× magnification lens results –zoom in

In the ICM case the profiles have to be thresholded such that the bottom of the W structure is brought to the level of the outer edges of the IRP.

The resolution of both 20× and 50× magnification lenses should be limited by the optical resolution, which is 400 nm and 250 nm (based on the Raleigh criterion) respectively. After thresholding the W structure, the lateral topography resolution based on the lateral period limit definition is larger than 2.4 µm and 1.07 µm for 20× lens and 50× lens respectively (see figure 7.16 and figure 7.17).

A closer analysis of the ICM measurement results in the 20× magnification lens configuration (see figure 7.12- left) reveals that the instrument is incapable of resolving appropriately shallow structures such that a taller ASG type standard would be suitable. For comparison, a similar star pattern, but 200 nm tall was measured using the ICM.

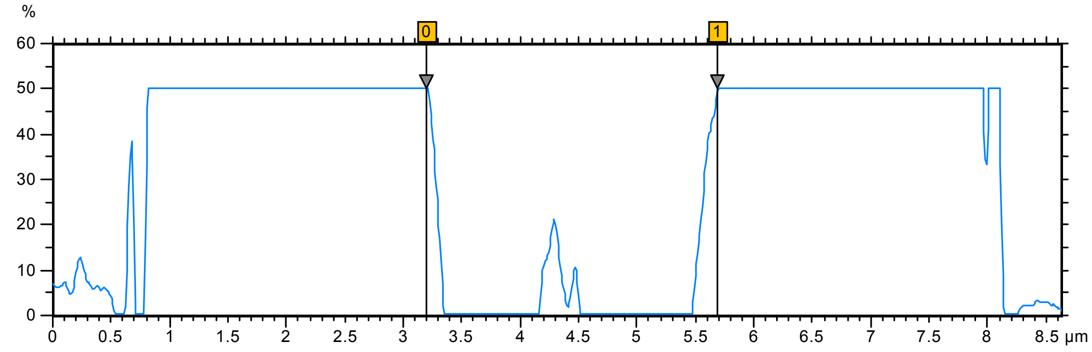

	0-1
Horizontal distance	2.48322 µm
Height difference	0.0739645 %

Figure 7.16 Measurement of the resolution at 50 % cut-off of the ICM width 20× magnification lens

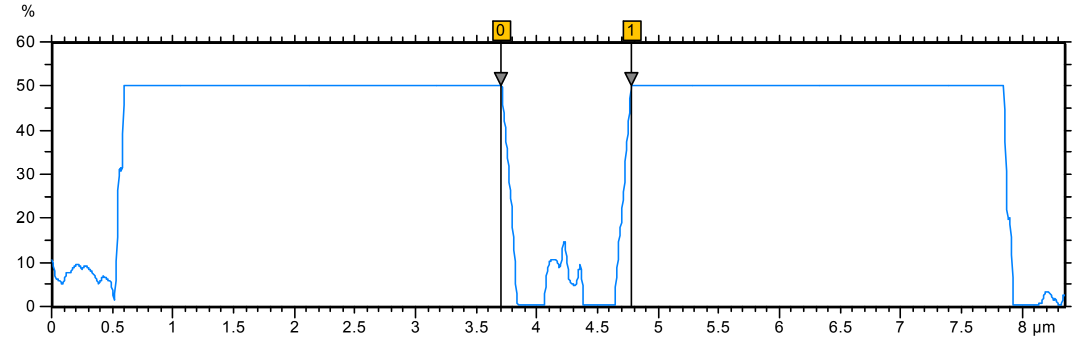

	0-1
Horizontal distance	1.07800 µm
Height difference	0.00000 %

Figure 7.17 Measurement of the resolution at 50 % cut-off of the ICM width 50× magnification lens

For comparison, measurements results at zoom 4 (four times smaller in the *x* and *y* direction than the maximum field of view) were acquired for both magnification lenses that corresponded to a nominal sampling distance of 160 nm and 60 nm for the 20× and 50× magnification lenses, respectively (see figure 7.18-left and figure 7.19-left). Unlike the measurements of the 30 nm type ASP material measure, the measurements on the 200 nm standard did not show any inversion in the vertical direction of the bottom and the top of the petals. Instead, the 50× magnification lenses result presents a significant width enlargement of the raised petals that starts at approximately 2.4 µm from the apex of the pattern (see figure 7.19-right).

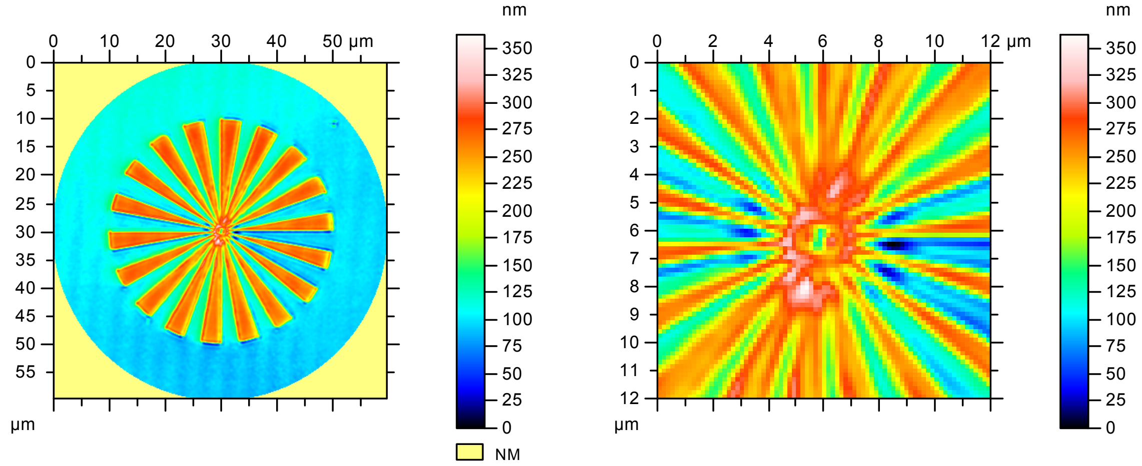

Figure 7.18 ICM 20× magnification lens measurement results of the 200 nm type ASG material measure: left - 4× optical zoom; right – detail of the apex

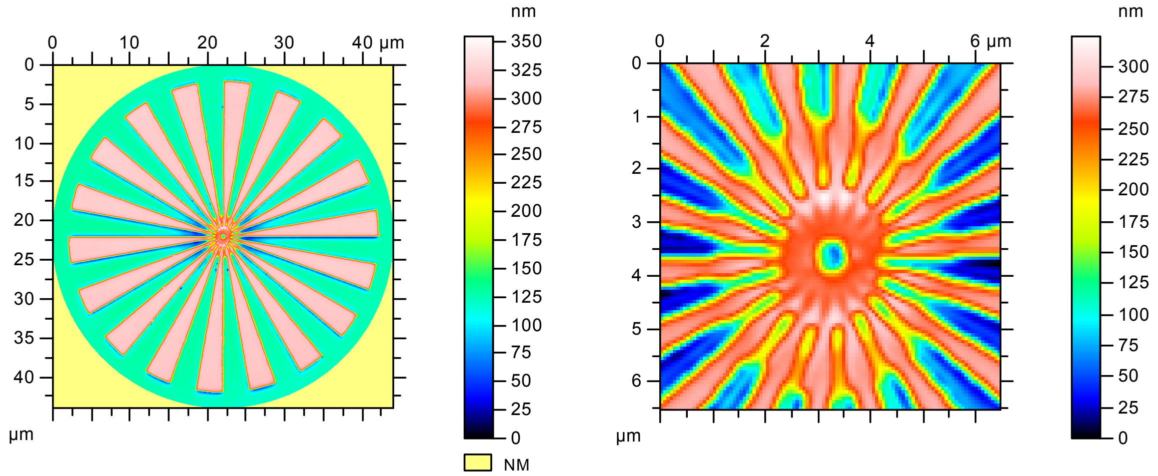

Figure 7.19 ICM 50× magnification lens measurement results of the 200 nm type ASG material measure: left - 4× optical zoom; right – detail of the apex

The lateral period limit measured on the 200 nm type ASG material measure is around 1 µm and 0.6 µm for 20× magnification lens and 50× magnification lens, respectively. The latter results are significantly improved comparing to the 30 nm type ASG material measure measurement results.

7.4.1 Fitting algorithm effect

The lateral resolution of the ICM can be improved by selecting a different type of algorithm to estimate the position of the measured point on the surface relative to the vertical scale of the instrument. In the examples presented above, the ICM was configured to use a centroid method of estimating the confocal peak position. The ICM can also be used in a measurement configuration that estimates the peak position using the maximum measured value of the confocal response. The measurement results on the 30 nm type ASP material measure using the latter method show that the vertical inversion of the bottom with the top of the petals take place at around 0.46 µm (see figure 7.20). This suggests that the fitting algorithms are as important as the quality of the optical components for achieving good areal measurements.

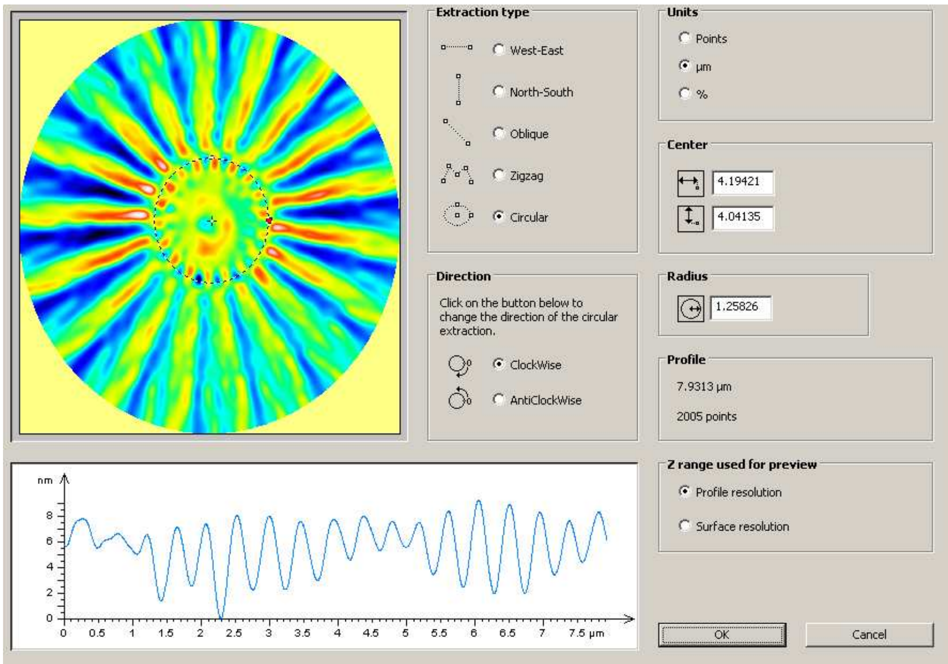

Extraction type
○ West-East
○ North-South
○ Oblique
○ Zigzag
● Circular

Units
○ Points
● µm
○ %

Center
4.19421
4.04135

Direction
Click on the button below to change the direction of the circular extraction.
● ClockWise
○ AntiClockWise

Radius
1.25826

Profile
7.9313 µm
2005 points

Z range used for preview
● Profile resolution
○ Surface resolution

Figure 7.20 ICM 50× magnification lens measurement results of the 30 nm type ASG material measure in peak mode

7.4.2 Sampling effect

When used without optical zoom, *i.e.* maximum field of view, and with a 1024 by 1024 number of points in the *x* and y direction, both ICM magnification lenses measurements should be limited by the sampling conditions (Nyquist theorem). Instead, the resolution tests show that the topographic resolution is at least twice as large as indicated by the sampling conditions without optical zoom. A summary of the ICM resolution test results when using the 200 nm type ASP material measure are presented in table 7.1. The tests consisted of several measurements using both magnification lenses in different optical zoom conditions. In all situations the measured topographical resolution was larger than the calculated resolution.

Table 7.1 Summary of the ICM resolution tests results with a 200 nm type ASP material measure

Resolution	20×			50×		
	Optical zoom					
	×4	×2	×1	×4	×2	×1
	/µm					
Optical	0.4	0.4	0.4	0.25	0.25	0.25
Sampling	0.3	0.6	1.3	0.13	0.25	0.5
Measured	1.0	2.2	3.2	0.5	0.9	1

The results presented in table 7.1 that are based on implementation of the lateral period limit definition do not negate the ICM instrument capability of resolving small 2D structures. In contrast, the instrument can measure fine periodical structures that are close to the optical 2D resolution. The fine detail of the apex of the star presented in figure 7.19-right shows that a circular profile can be extracted close to the apex of the star, which matches the lower limit of the resolution reproduced by the 30 nm type ASP material measure, but with serious loss of both lateral and vertical accuracy. Pitch measurement wise, the ICM instrument can be used close to the theoretical optical resolution but for topography measurement that is not the case.

7.5 Measurement uncertainty

The lateral resolution contribution to the measurement uncertainty, u_{Res}, is propagated in the form of a rectangular distribution that has a variance equal to the $Res^2/3$, where *Res* is the lateral topographical resolution.

A summary of the standard measurement uncertainties associated with the calibration of the lateral topographical resolution of the CSI and ICM instruments used as test cases are presented in table 7.2.

Table 7.2 Summary of the standard measurement uncertainties associated with the lateral topographical resolution of the CSI and ICM – no optical zoom

Magnification objective lens	CSI	ICM
	/µm	
20×	2.5	1.8
50×	2.5	0.6

7.6 Summary

Most commercial surface topography measuring instrument manufacturers specify the lateral resolution of their instruments in terms of a 2D theoretical value that does not take into account the 3D nature of how the instrument is used. The new definition of the lateral period limit given in ISO 25178 part 600 (2012) is an attempt to formulate a definition of lateral resolution that can be experimentally determined and is representative of the 3D nature of the instruments. Implementation of such a definition is complicated because it is application-dependent and, therefore, it is impossible to produce suitable all-purpose physical measurement standards. For example, grating-type artefacts are designed with a predefined pitch, which that allows the testing of the performance of instruments in limited situations. For a contact stylus instrument, such a simple artefact is enough to portray the instrument behaviour, as these instruments already have a well-understood measurement model. However, this is not always the case for optical instruments, which often have problems due to their non-linear response to certain surface features. Although, the non-linear response of optical instruments should not be the object of attention during the resolution tests, to a certain extent, it is unavoidable, as these problems often arise during measurements. In such situations it becomes easy to point out to the errors and forget about resolution, which is not a correct approach because, like in the stylus flight at high speeds (Whitehouse 2004), these measurement conditions should be avoided as they do not characterise the optical systems in what should be their prescribed operational conditions.

The current compromise is to test the z axis measurement resolution independent of the x and y axes resolution. In this situation, the measurement noise includes the contribution of the z resolution and the lateral period limit is used to determine the x and y resolution in the areal measurement context. An easy practical test has been described in section 7.2 that uses a type ASP artefact to test the lateral period limit. Both CSI and ICM show various errors that are not easily captured by traditional tests that use unidirectional grid patterns. The lateral period limit provides useful information about the minimum value of the S-filter and allows calculation of the contribution of the resolution of the x and y scales to the measurement uncertainty, when the instrument is used in a linear operational regime.

8 Examples of measurement uncertainty calculations

The standard uncertainty associated with a measurement result can be written as the square of a quadratic sum of two components that are called the type A and the type B measurement uncertainty (BIPM 2008a)

$$u = \sqrt{u_A^2 + u_B^2} \qquad 8.1$$

where u is the standard uncertainty, u_A is the type A standard uncertainty and u_B is the type B standard uncertainty. The type A standard uncertainty is given by the standard deviation from repeated measurements. According to GUM (BIPM 2008a) the components of the type B measurement uncertainty are taken from: *experience with or general knowledge of the behaviour and properties of relevant materials and instrument; manufacturer's specification; data provided in calibration and other certificates and uncertainties assigned to reference data taken from handbooks.*

The difference between the type A and type B standard uncertainties is that former one is based on a frequency distribution (taken from repeated measurements) and the latter is based on *a priori* distribution (known information that can also be given by a standard deviation).

If the components of the type B standard uncertainty are uncorrelated, the type B standard uncertainty can be calculated using the following equation

$$u_B^2 = \sum_n C_i^2 u^2(x_i) \qquad 8.2$$

where C_i is the sensitivity coefficient (BIPM 2008a) and the $u(x_i)$ is the uncertainty associated with the n-th component. Each of the metrological characteristics of the instrument represents a separate component of the type B standard uncertainty associated with the calibration of the scales.

The contribution of the scales calibration can be calculated using equation 8.2, where the sensitivity coefficients (C_i) are all equal to unity and $u(x_i)$ is the contribution of each of the metrological characteristics to the measurement uncertainty(measurement noise and residual flatness u_{NF}; the combined effect of the measurement errors, traceability, repeatability and/or reproducibility on the co-ordinate measurement standard uncertainty $u_{T\text{-}x}$, $u_{T\text{-}y}$ and

$u_{T\text{-}z}$; lateral resolution contribution to the measurement uncertainty u_{Res}). The models for calculating the contribution of the calibration of the x, y and z scales are given below.

$$\begin{cases} u_x = \sqrt{u_{T-x}^2 + u_{\mathrm{Res}}^2} \\ u_y = \sqrt{u_{T-y}^2 + u_{\mathrm{Res}}^2} \\ u_z = \sqrt{u_{NF}^2 + u_{T-z}^2} \end{cases} . \qquad 8.3$$

The contribution of the metrological characteristics to the uncertainty associated with the calculation of a parameter from an areal measurement has to be considered on a case by case basis. For example, the calculation of the height of a type PGR material measurement standard requires averaging the measured profiles along the y axis, which has a different effect on the residual flatness contribution then the effect of the L-filter, which is used in the calculation of areal parameters. In the case of calculating *Sq* from the measurement of a type ADT material measure, the sensitivity coefficient corresponding to the residual flatness and measurement noise is different from the one used to deduce the equations 8.3.

8.1 Example 1 – Step height measurements

The step height standard artefact measured in this example is similar to the 350 nm step height standard artefact used to calibrate the z scale of the instruments, see figure 8.1. The central groove is the measurement groove. The other two grooves are for position identification only.

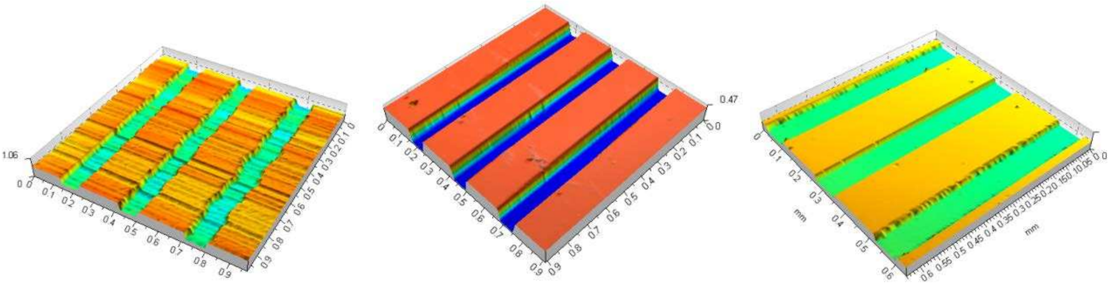

Figure 8.1 Measurement result of a 350 nm step height standard artefact measured using: left – stylus instrument; centre – CCI in using the 20× magnification lens configuration; and right – ICM in using the 20× magnification lens configuration

According to equation 8.1 the standard measurement uncertainty associated with the step height measurement is a combination of type A and type B measurement uncertainty. The type A measurement uncertainty is given by the standard deviation of the mean value of minimum of three repeated measurements. The type B measurement uncertainty will include the measurement noise and flatness deviation contribution, and a linearity and amplification contribution, and it can be written as

$$u_B^2 = C_{NF}^2 u_{NF}^2 + C_{T-z}^2 u_{T-z}^2 \text{ .} \qquad 8.4$$

Measurement noise and residual flatness contribution

Since the step height analysis in areal mode averages the profiles along the *x* axis of the instrument some of the effects of the *y* axis flatness of the stylus instrument into the measurement uncertainty associated with step height calculation are diminished (see figure 8.2 left). As the step height calculation uses a limited area of the measured topography, only 0.3 mm in the 350 nm standard artefact case, the contribution of the measurement noise and residual flatness has to be calculated on a reduced length of the mean profile (see figure 8.2 right).

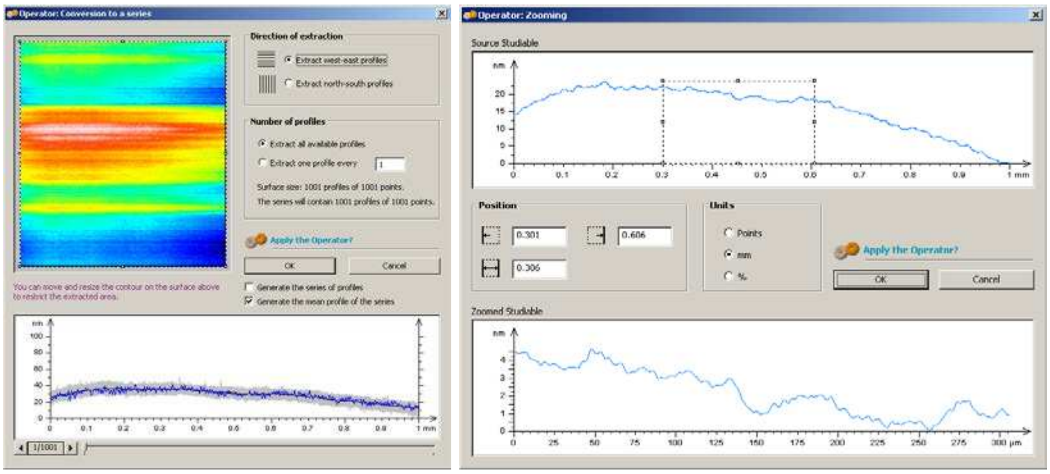

Operator: Conversion to a series

Direction of extraction
● Extract west-east profiles
○ Extract north-south profiles

Number of profiles
● Extract all available profiles
○ Extract one profile every 1

Surface size: 1001 profiles of 1001 points.
The series will contain 1001 profiles of 1001 points.

You can move and resize the contour on the surface above to restrict the extracted area.

☐ Generate the series of profiles
☑ Generate the mean profile of the series

Operator: Zooming

Position
0.301
0.606
0.306

Units
○ Points
● mm
○ %

Figure 8.2 Extraction of mean profile along the *x* axis of stylus instrument (right) and zoom operation of the mean profile (left)

The residual flatness and the measurement noise can be estimated by measuring *Pt* directly without any other surface averaging on a flat. The measurement noise and the residual flatness are superimposed such that their combined contribution is propagated in the form of a rectangular distribution with inexactly prescribed limits, which has a variance equal to the $Pt^2/12 + \sigma^2_{PT}/9$, where σ_{PT} is the standard deviation (BIPM 2008a).

It follows that the u_{NF} for the 350 nm step height measurement using the stylus instrument at 0.5 mm s^{-1} scanning speed, is 0.66 nm (see table 8.1). Similarly the u_{NF} for CSI and ICM in 20× lens configuration, is 0.08 nm and 5 nm respectively.

Table 8.1 u_{NF} calculation

Measurement No.	CCI 20× magnification lens	ICM 20× magnification lens	Stylus 0.5 mm s^{-1} scanning speed
	Pt /nm		
1	0.22	8.8	2.64
2	0.27	20	2.15
3	0.15	4.2	2.50
4	0.28	14	1.89
5	0.36	33	2.26
Average	0.26	16	2.29
Repeatability (σ_{Pt})	0.08	5	0.13
u_{NF}	0.08	5	0.66

The step height analysis algorithm calculates the distance between two parallel lines that are fitted through a restricted number of the topography data points (see figure 8.3, ISO 5436-1 2000). For the analysis of a ISO 5436-1 (2000) type A1 standard , and considering the co-ordinate measurements to be un-correlated, the sensitivity coefficients that are used to propagate the measurement noise and residual flatness component are given by equation 8.5.

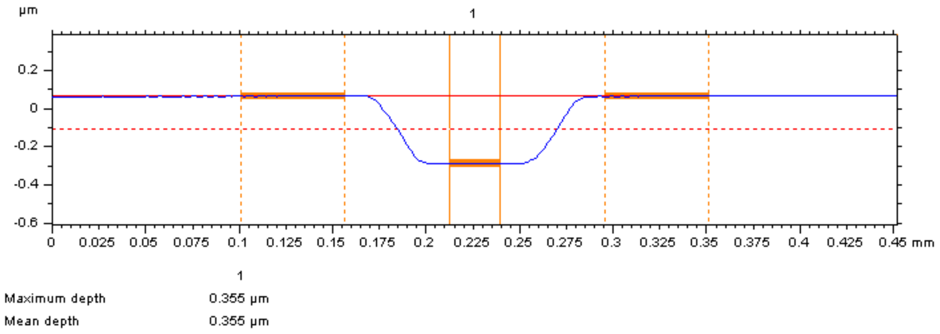

	1
Maximum depth	0.355 µm
Mean depth	0.355 µm

Figure 8.3 Example of step height analysis in profile mode

$$C_{NF} = \frac{3d}{W} + \frac{3d}{4W} = 3.75\frac{d}{W} \qquad 8.5$$

where C_{NF} is the sensitivity coefficient, d is the sampling distance and W is the width of the groove. For a step height standard, similar to the one presented in figure 8.3 the width of the groove is approximately 0.09 mm. If the sampling distance is 1 µm the C_{NF} is approximately $0.042^{½}$, which is a typical value for CSI and stylus instrument, whereas for the ICM that is characterised by a sampling distance of 0.6 µm, the C_{NF} is approximately $0.025^{½}$.

Amplification and linearity contribution

The contribution of amplification and linearity remains unchanged (see table 6.5) and the sensitivity coefficient will be equal to unity.

Type A uncertainty

Type A uncertainty is calculated as the standard deviation of the mean of n repeated measurements. Repeatability values in table 6.1, table 6.3 and table 6.4 are representative for type A uncertainty. If the non-uniformity of the standard artefact is not known, the three repeated measurement can be performed at slightly different positions along the length of the groove such that the type A uncertainty will account for non-uniformity of the standard artefact.

Coverage factor

The calculation of the combined measurement uncertainty requires the value of the coverage factor (k) for a 95 % confidence level. The value of the coverage factor is based the number of effective degrees of freedom (ν) that can be calculated with the following formula (BIPM 2008a):

$$\nu = \frac{u^4}{u_A^4}. \qquad 8.6$$

The k values can be obtained from table G2 at page 78 of GUM (BIPM 2008a). For these examples, the coverage factor is equal to two.

Uncertainty

A summary of the uncertainty associated with the measurement of a 350 nm step height standard is presented in table 8.2.

Table 8.2 Uncertainty budget associated with the measurement of a 350 nm step height standard

Contribution /nm	CCI 20× magnification lens	ICM 20× magnification lens	Stylus 0.5 mm s^{-1} scanning speed- adjusted
$C_{NF} \times u_{NF}$	$0.042^{½} \times 0.08$	$0.025^{½} \times 5$	$0.042^{½} \times 0.66$
$C_{T\text{-}z} \times u_{T\text{-}z}$	1 × 1.0	1 × 10	1 × 1.0
Type B	1.0	10	1.0
Type A (typical values)	0.19	2.3	0.1
u	1.0	10	1.0
U (k = 2)	2.0	20	2.0

8.2 Example 2 – Pseudo-random standard artefact

In this example type ADT material measure was measured (see figure 8.4) and only the *Sq* parameter was compared with the calibrated value. The measurement area of the standard artefact is a square with a nominal side of 1.5 mm.

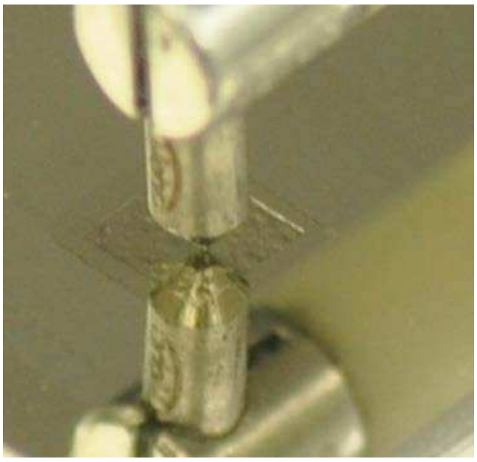

Figure 8.4 Measurement of a type ADT material measure using the stylus instrument

i. Three stylus measurements were performed at 0.5 mm s^{-1} x axis scanning speed with a 2 µm sampling distance in both x and y directions. The *Sq* value was calculated in a central region of 1 mm by 1 mm of the measurement area of the standard artefact (see figure 8.5 left).

ii. Three CSI measurements were performed in the 20× magnification lens configuration (see figure 8.5 centre). The *Sq* value was calculated in a central region of 0.9 mm by 0.9 mm of the measurement area of the standard artefact with a 0.9 µm sampling distance in both *x* and *y* directions.

iii. Three ICM measurements were performed in the 20× magnification lens configuration (see figure 8.5 right). The *Sq* value was calculated in a central region of 0.6 mm by 0.6 mm of the measurement area of the standard artefact with a 0.6 µm sampling distance in both *x* and *y* directions.

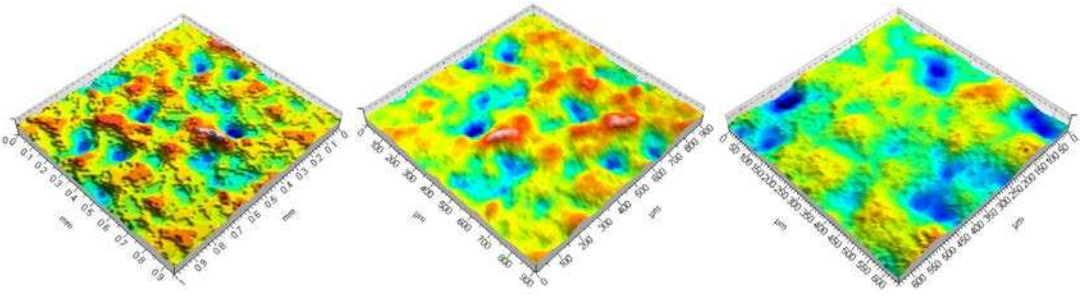

Figure 8.5 Measurement result of the central area of the ADT type standard artefact: left – stylus instrument; centre – CCI in using the 20× magnification lens configuration; and right – ICM in using the 20× magnification lens configuration

The standard uncertainty associated with the type ADT measurement is a combination of type A and type B measurement uncertainties. The type A measurement uncertainty is given by the standard deviation of the mean value of minimum of three repeated measurements. The type B measurement uncertainty will include the measurement noise and the residual flatness contribution, a linearity and amplification contribution, and is given by equation 8.2, where the sensitivity coefficients have to be calculated to suit the conditions of the current measurement example.

Measurement noise and residual flatness contribution

The value of *Sq* is calculated using the model given by

$$Sq = \sqrt{\frac{\sum_{NM}\left(z_{ij} - \bar{z}\right)^2}{NM}} \qquad 8.7$$

where N is number of points measured along the x axis, M is number of points measured along the y axis, the z_{ij} is a height measurement corresponding to an arbitrary position inside the NM grid of points and $\bar{z}$ is

$$\bar{z} = \frac{\sum_{NM} z_{ij}}{NM} . \qquad 8.8$$

C_{ij} is the sensitivity coefficient corresponding to z_{ij} and is calculated using

$$C_{ij} = \frac{\partial Sq}{\partial z_{ij}} \cong \frac{1}{Sq}\frac{\left|z_{ij} - \bar{z}\right|}{NM} . \qquad 8.9$$

Considering that the contribution of the NM height measurements to the Sq measurement uncertainty has a correlated effect, the residual flatness and measurement noise contribution to the Sq measurement uncertainty can be calculated as follows

$$u(NF) = \sum_{NM} C_{ij} u_{NF} = \frac{Sa}{Sq} u_{NF} . \qquad 8.10$$

The values of the measurement noise and residual flatness uncertainty component, which affects the z axis measurements, is directly taken from table 5.9 for the stylus instrument and the CSI, whereas for ICM the Sq value was calculated using 5 μm S-filter nesting index and a limited portion of the measured area of which side was equal to the value of the L-filter nesting index (0.55 mm).

Amplification and linearity contribution

The contribution of the amplification and linearity to the measurement uncertainty associated with Sq can be calculated in the same manner as in the $u(NF)$ case

$$u(T-z) = \sum_{NM} C_{ij} u_{T-z} = \frac{Sa}{Sq} u_{T-z} . \qquad 8.11$$

It follows that

$$u_B = \frac{Sa}{Sq}\sqrt{u_{NF}^2 + u_{T-z}^2} . \qquad 8.12$$

The contribution of amplification and linearity can be taken from table 6.5.

Type A uncertainty

Type A uncertainty is calculated as the standard deviation of the mean of three repeated measurements (see table 8.3). Similarly to the step height measurement, if the non-uniformity of the standard artefact is not known, the repeated measurement can be performed at slightly different positions, such that the type A uncertainty will account for non-uniformity of the standard artefact.

Note that the difference in *Sq* value obtained using different instruments is due to different filter settings and positions. The CSI and stylus instrument results are similar because the values of the L-filter are close to each other.

Table 8.3 Measurements of type ADT standard

Measurement ID	CCI 20× magnification lens	ICM 20× magnification lens	Stylus 0.5 mm s^{-1} scanning speed- adjusted
	Sq / nm		
1	955.30	1021.7	920
2	955.50	1021.48	941
3	955.07	1020.94	942
Average	955.29	1021.37	934
u_A	0.13	0.23	7

Uncertainty

A summary of the uncertainty associated with the measurement of type ADT standard is presented in table 8.4.

The values obtained in table 8.3 were compared with the NPL Areal Instrument measurement results on the type ADT material measure. The summary of the areal measurement results is presented in table 8.5. The measurement errors do not exceed the combined standard uncertainties (see figure 8.6).

Table 8.4 Uncertainty budget associated with the measurement of type ADT material measure

Contribution /nm	CCI 20× magnification lens	ICM 20× magnification lens	Stylus 0.5 mm s^{-1} scanning speed- adjusted
$C_{NF} \times u_{NF}$	0.78 × 0.7	0.78 × 21	0.78 × 28
$C_{T\text{-}z} \times u_{T\text{-}z}$	0.78 × 7	0.78 × 18	0.78 × 2.3
Type B	5.9	22	28
Type A (typical values)	0.13	0.23	7
u	5.9	22	29
U (k = 2)	12	44	58

Table 8.5 Summary of the NPL Areal Instrument measurement results on ADT type standard

	Field of view of CCI 20× magnification lens	Field of view of ICM 20× magnification lens	Stylus measured area
Sq / nm	961	1027	918
u_{Sq} / nm	9	5	5

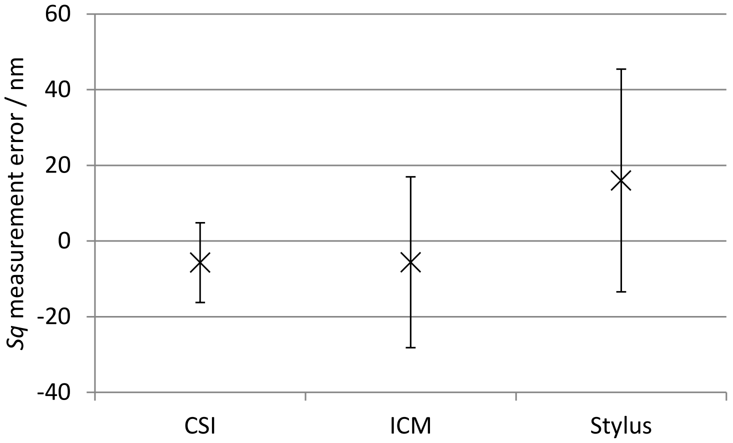

Figure 8.6 *Sq* measurement error plot. Error bars are the combined standard uncertainty of the instruments and of the NPL Areal Instrument

9 Summary and conclusions

The aim of this PhD was to develop a traceability infrastructure for industrial areal surface topography measurements. The traceability route for industrial users had to be proven through to a calibration routine that is composed of a series of simple measurement tests involving calibrated areal physical measurement standards that are traceable to the definition of the metre. The main focus of the PhD was on the development of: a primary areal surface topography measuring instrument; physical measurement standards; methods for calculating uncertainties associated with areal surface texture measuring instruments and surface texture parameters; and, as a side benefit, good practice guides of calibrating areal surface texture measuring instruments.

The research work described in this thesis started with the task of finishing the development of the NPL Areal Instrument. The instrument was designed and put together by a team of researchers at NPL; however the instrument was never used for metrological purposes. Initial tests showed that the signal to noise ratio of the *z* interferometer did not allow for nonmetric measurement uncertainties, which lead to a change of the original design of the instrument. With the *z* interferometer mounted in a horizontal position and the probe in vertical position, the *z* metrology required a complicated optical layout that did not favour the operation of the instrument. In consequence the position of the *z* interferometer was redesigned such that the interferometer was mounted collinear with the probe. Hereafter, a complex measurement model was developed that accounted for all known error sources as shown in chapter 2. Each error source was studied separately and the contribution to the instrument measurement uncertainty was estimated. The error sources were input quantities in the measurement model and based on that the measurement uncertainty associated with the instrument co-ordinate measurement was calculated. The measurement uncertainty model was unique because it was developed for a bespoke instrument.

Chapter 9
Summary and conclusions

Industrial users favour a simple model to calculate measurement uncertainties, which uses a limited number of input quantities. A simpler method of calibrating areal surface topography measuring instruments was very difficult to envisage without changing the way that international draft standards were being developed. Specification standards have been drafted for several types of instruments without any consistency in terminology, this activity mainly being driven by instrument manufacturers. As a result, for each type of instrument a long list of influence quantities was developed despite that all these instruments were designed to measure point co-ordinates. One of the major contributions of the research work presented in this thesis is that the international standardisation community accepted a common ground for all areal surface topography measuring instruments, materialised in the form of the set of metrological characteristics.

The metrological characteristics approach developed in this thesis allows for a simpler way of calibrating the areal surface topography measuring instruments because it is capable of quantifying the combined effect of several influence factors. Metrological characteristics are input quantities in a measurement model that can be measured, generally using a limited number of calibrated material measures (see chapter 3), and make an immediate contribution to the measurement uncertainty associated with the measured coordinates provided by the instrument. A summary of the metrological characteristics is: measurement noise, flatness deviation (chapter 5), amplification coefficient, linearity errors, perpendicularity of the axis (chapter 6), and resolution (chapter 7). The experimental work used three different instruments that were described in more detail in chapter 4.

The aim of the work that followed was to find the optimal measurement procedures. However, new measurement procedures were developed. In the case on the measurement noise and flatness deviation it was found that known measurement methods were not always easily implementable. The presence of non-stationary noise in the system and spurious data led to two new developments. In response to the former issue, a measurement procedure that accounts for both the measurement noise and flatness deviation was developed (see section 5.4). The presence of spurious data led to the development of a new procedure that does not rely on filtering the measured topography (see section 5.2).

Two major challenges were to be addressed in the case of the calibration of the amplification coefficient, linearity and squareness of areal surface topography measuring instruments: development of an areal method of calibrating step heights and development of a calibration procedure of the lateral scales of areal instruments that were not based on pitch measurements. In response to the first of these two challenges, a method based on profile standard of calculating the step height was developed (see section 6.1). For the calibration of the lateral scales a method that relies on the measurement of the relative position of the pits of a cross-grating was proposed (see section 6.2).

Unlike the metrological characteristics discussed above, in the case of the resolution of the axis there was not an international consensus on the definition of the lateral resolution. However, just in the last year it has been finally decided that the best way forward was to estimate the lateral resolution using the definition of the lateral period limit. Once this decision was taken a practical method of measuring the lateral period limit has been developed (see section 7.2).

Finally, measurement uncertainty models that use the metrological characteristics as input quantities have been developed for a step height measurement and calculation of Sq (see chapter 8).

To summarise, the flatness deviation tests could be considered to be the basis of a routine calibration of the instruments and in consequence can be included in the ISO 25178 specification standards as pre-calibration steps in order to quantify the instrument contribution to the measurement uncertainty. The measurement noise test, due to the complex interaction between the probe and the sample, can only be considered as a performance test of the instrument. The measurement noise has to be evaluated for the measured sample in order to be included in a measurement uncertainty analysis that is associated with any particular measurement. In the latter situation, the measurement noise does not strictly estimate the measurement uncertainty associated with the *z* axis scale of the instrument (the calibration of the instrument is only a constituent part of the overall measurement uncertainty associated with areal surface texture measurements).

A combination of linearity errors, repeatability and reproducibility can increase the *z* axis scale calibration uncertainty, but they may not be the main factors affecting the uncertainty associated with the *z* axis measurements, compared to the flatness deviation and measurement noise contributions.

The quality of the lateral scales of the instruments is often better than the lateral resolution of the instruments, with the exception of the *y* axis scale of the contact stylus. The squareness of the *x* and *y* axes contribution to the measurement uncertainty is often small enough to be omitted in the calculation of measurement uncertainties.

In conclusion, a clear traceability route for areal surface topography measurements has been demonstrated, which includes a primary areal surface topography instrument, a set of areal material measures that are used as measurement standards, procedures that allow calibration of the axes of operation of the areal surface topography measuring instruments and examples of methods for calculating measurement uncertainties. As the result of the work, NPL good practice guides for calibrating three types of areal surface topography measuring instruments have been developed (Giusca and Leach 2013a,b,c) and six journal papers have been published (Leach *et al.* 2009, Giusca *et al.* 2011a,b, Giusca *et al.* 2012a,b, Giusca and Leach 2013d). My contribution to the project comprises work on the final design, measurement model and uncertainty budget of the NPL Areal Instrument, development of the set of metrological characteristics and associated measurement procedures including the experimental setups and data analysis.

The traceability of areal surface topography measuring instruments is frequently debated because it is difficult to find a significant improvement in the instrument performance after the instruments have been calibrated, unless the height of step height artefacts and the pitch of a grating are measured. The results presented in chapter 6 show that often the calibration of the amplification and linearity of the scales, which also infer the traceability route, do not affect the surface topography measurements in a manner that will concern the general practitioner. The filtration operations that are employed during surface texture analysis, the more intimate effects of the optical probe interaction with the sample and the industrial samples measurement reproducibility contribution to the measurement uncertainty, often diminish the traceability contribution to the extent that it can be considered negligible, but that is not to say that the calibration of the scales should not be performed. From the outset of the thesis, it was clearly pointed out the calibration is a two-step process in which the calibration of the scales of the instrument is only one step. Traceability of areal surface topography measurements *via* an areal primary instrument held at a national measurement institute is also debated, and for good reasons. As long as the traceability to the standard of the metre is demonstrated any route is acceptable (see for example Evans 2010).

Further research is necessary to determine the spatial frequency response of the instrument, because testing the current metrological characteristics is not enough to qualify an areal surface topography measuring instrument for the measurement of complex, rough surfaces. The way forward is to measure the ITF. The problem with the ITF of the optical instruments is that it is determined from the height data. For example, a CSI instrument captures the envelope (and phase) information from the interference fringes, and from this fringe data, the height is calculated. This calculation is the non-linear step. If the instrument response can be found at the fringe level, what is referred to as the optical transfer function (OTF), then the full range of surface heights and gradients that can be measured. As has been shown in Mandel *et al*. (2012), the OTF can be determined using a sphere. The sphere is larger than the lateral resolution of the instrument but smaller than its field of view, therefore, all the gradients that can be measured are captured.

Future work aims to develop methods of calibrating the optical transfer function for CSI and ICM types of areal surface topography measuring instruments, which requires the development of an uncertainty model based on sphere measurement technique and a primary micrometre sphere interferometer. The uncertainty in the nonlinear response of the optical instruments will also be investigated.

References

Abbott E J, Bousky S and Williamson D E 1938 The profilometer *Mech. Eng.* **60** 205-216

Abbott E J and Firestone F A 1933 Specifying surface quality *Mech. Eng.* **55** 569-773

Ai C, Novak E 1997 Centroid approach for estimating modulation peak in broad-bandwidth interferometry *U.S. Patent* 5633715

Artigas R, Laguarta F and Cadevall C 2004 Dual-technology optical sensor head for 3D surface shape measurements on the micro and nano-scales *Proc. SPIE* **5457** 166-174

Artigas R, Pintó A and Laguarta F 1999 Three-dimensional micromeasurements on smooth and rough surfaces with a new confocal optical profiler *Opt. Meas. Syst. for Ind. Insp***. 3824** 93-103

Balsamo A, Di Ciommo M, Mugno R, Sartori S 1996 Towards instrument-oriented calibration of CMMs *Ann. CIRP* ***45*** 479–472

Bayliss D, Leach R K, Hall M 2006 Development of an electromagnetic spring for use with high accuracy surface texture measuring probe *NPL Report* **DEPC-EM 006**

Bendeli A, Duruz J, Thwaite E G 1974 A surface simulator for precise calibration of surface roughness measuring equipment *Metrologia* **10** 137-143

Bennett J M and Dancy J H 1981 Stylus profiling instrument for measuring statistical properties of smooth optical surfaces *Appl. Opt.* **20** 1785–1802

Bennett J M 1976 Measurement of the RMS roughness, autocovariance function and other statistical properties of optical surfaces using a FECO scanning interferometer *Appl. Opt.* **15** 2705-2721

Bhushan B, Wayant J C and Koliopoulis C L 1985 Measurement of surface topography of magnetic tape by Mirau interferometry *Appl. Opt.* **24** 1498-1497

BIPM, IEC, IFCC, ISO, IUPAC, IUPAP and OIML 2008a Evaluation of measurement data — Guide to the expression of uncertainty in measurement (Bureau International des Poids et Mesures) JCGM 100

BIPM, IEC, IFCC, ISO, IUPAC, IUPAP and OIML 2008b Evaluation of measurement data — Supplement 1 to the "Guide to the expression of uncertainty in measurement" — Propagation of distributions using a Monte Carlo method (Bureau International des Poids et Mesures) JCGM 101

BIPM, IEC, IFCC, ILAC, ISO, IUPAC, IUPAP, and OIML 2008c *International Vocabulary of Metrology – Basic and General Concepts and Associated Terms* (Bureau International des Poids et Mesures) JCGM 200

Binning G, Quate CF, Gerber C 1986 Atomic force microscope *Phys. Rev. Let.* **56** 930-933

Binning G, Rohrer 1983 Scanning tunnelling microscopy *Surf. Sci.* **126** 236-244

Birch K P, Downs M J 1994 Correction to the updated Edlén equation for the refractive index of air *Metrologia* **31** 315-316

References

Blunt L, Jiang X, Leach R K, Harris P M and Scott P 2008 The development of user-friendly software measurement standards for surface topography software assessment *Wear* **264** 389–393

Blunt L and Jiang X 2003 *Advanced technique for assessment surface topography – development of a basis for the 3D suarface texture standards "SUARFSTAND"* (Kogan Page Science)

Boedecker S, Rembe C,Schmid H, Hageney T and Köhnlein T 2011 Calibration of the *z*-axis for large-scale scanning white-light interferometers *J. Phys.: Conf. Ser.* **311** 012027

Born M and Wolf E 1997 *Principles of optics: electromagnetic theory of propagation, interference and diffraction of light 6th edn.* (Cambridge University Press)

Botcherby E, Booth M, Juškaitis R and Wilson T 2009 Real-time slit scanning microscopy in the meridional plane *Opt. Lett.* **34** 1504-1506

Brand U and Fluegge J 1998 Measurement capabilities of optical 3D-sensors for MST applications *Microelectron. Eng.* **41/42** 623–626

Brand U and Hillmann W 1995 Calibration of stepheight standards for nanometrology using interference microscopy and stylus profilometry *Prec. Eng.* **17** 22-33

Bruzzone A A G, Costa H L, Leonardo P M, Lucca D A 2008 Advances in engineering surfaces for functional performance *Ann. CIRP* **57** 750-769

Bui S H and Vorburger T V 2007 Surface metrology algorithm testing system *Precis. Eng.* **31** 218–225

Bui S H, Renegar T B, Vorburger T V, Raja J and Malburg M C 2004 Internet-based surface metrology algorithm testing system *Wear* **257** 1213–1218

Caber P J 1993 Interferometric profiler for rough surfaces *Appl. Opt.* **32** 3438-3441

Chetwynd D G, Siddons D P, Bowen D K 1983 X-ray interferometer calibration of surface roughness measuring equipment *J. Phys. E: Sci. Instrum.* **16** 871-874

Colona de Lega X and de Groot P 2012 Lateral resolution and instrument transfer function as criteria for selecting surface metrology instruments *Proc. SPIE* ***TBC***

Conchello J A and Hansen E W 1990 Enhanced 3-D reconstruction from confocal scanning microscope images. 1: Deterministic and maximum likelihood reconstructions *Appl. Opt.* **29** 3795-3804

Coupland J M and Lobera J 2010 Measurement of steep surfaces using white light interferometry *Strain* **46** 69-78

Coupland J M and Lobera J 2008 Holography, tomography and 3D microsccopyas linear filtering operations *Meas. Sci. Technol.* **19** 074012

Cox M G, Harris P M 2006 Software Support for Metrology. Best Practice Guide No. 6. Uncertainty Evaluation *NPL Report* DEM-ES-011

Cox M G, Forbes A B, Harris P M and Peggs G N 1999 Experimental design in determining the parametric errors of CMM *Proc. 4th Lambdamap Conf., Northumbria, UK,* 13-22

Creath K and Wayant J C 1990 Absolute measurement of surface roughness *Appl. Opt.* **29** 3823-3827

Creath K 1989 Calibration of numerical aperture effects in interferometric microscope objectives *Appl. Opt.* **28** 3333–3338

Dagnall H 1998 *Exploring surface texture* 3rd edition (Taylor Hobson Ltd)

Danzebrink H U, Koenders L, Wilkening G, Yacoot A and Kunzmann 2006 Advances in scanning probe microscopy for dimensional metrology *Ann. CIRP*. **55** 841-897Danzl R, Helmli F, Rubert P, Prantl M 2008 Optical roughness measurements on specialy designed roughness standards *Proc. SPIE* **7102** 71020M

Davidson M, Kaufman K, Mazor I and Cohen F 1978 An application of interference microscopy to integrated circuit inspection and metrology *Proc. Soc. Photo-Opt. Instrum. Eng.* **775** 223–241

De Chiffre L, Nielsen H.S 1987 A digital system surface roughness analysis of plane and cylindrical parts *Prec. Eng.* **9**, 59-64

Deck L and de Grout P 1994 High-speed noncontact profiler based on scanning white light interferometer *Appl. Opt.* **33** 7334-7388

DeVries W R and Li C J 1985 Algorithms to deconvolve stylus geometry from surface profile measurements *J. Eng. Ind.* **107** 167-174

Digital Surf 2011 www.digitalsurf.fr/en/downloads.html (accessed 17 March 2011)

Doi T, Toyoda K, Tanimura Y 1997 Effects of phase changes on reflection and their wavelength dependence in optical profilometry *Appl. Opt.* **36,** 7157-7161

O'Donnell K A 1993 Effects of finite stylus width in surface contact profilometry *Appl. Opt.* **32** 4922-4928

Dong W P, Sullivan P J and Stout K J 1994a Comprehensive study of parameters for characterizing three-dimensional surface topography III: parameters for characterizing amplitude and some functional properties *Wear* **178** 29–43

Dong W P, Sullivan P J and Stout K J 1994b Comprehensive study of parameters for characterizing three-dimensional surface topography IV: parameters for characterizing spatial and hybrid properties *Wear* **178** 45–60

Downs M J, Birch K P, Cox M G, Nunn J W 1995 Verification of a polarization-insensitive optical interferometer system with subnanometric capability *Precision Engineering* **17** 1-6

Evans C J 2010. Calibration, self-calibration and uncertainty in testing optical flats *Proc. SPIE* 76560S.

Evans C J and Bryan J B 1999 "Structured", "Textured" or "Engineered" Surfaces *Ann. CIRP* **48** 541-556

Felder R 2005 Practical realization of the definition of the metre, including recommended radiations of other optical frequency standards (2003) *Metrologia* **42** 323-325

Forbes A B, Leach R K 2005 Self-calibration of a novel surface texture measuring instrument *Proc. 7th Lambdamap Conf., Cranfield, UK, 27–30 June* 276-285

Frühauf J, Krüger-Sehm R, Felger A, Dziomba T 2012 Areal roughness standards *Proc. 12th Int. euspen Conf., Stockholm, Sweden, 4 – 7 Jun* 133-136

Fukatsu H, Oka K and Yanagi K 2006 Analysis of diffraction image caused by micro-geometry for an optical profiling sensor *Proc. JSPE Spring Meeting* **N-62** 1101.

References

Fujii A, Suzuky H and Yanagi K 2011 Development of measurement standards for verifying functional performance of surface texture measuring instruments *J. Phys.: Conf. Ser.* **311** 012009

Fujii A, Suzuky H and Yanagi K 2010 A study on response properties of surface texture measuring instruments in terms of surface wavelengths *Proc. ASPE Summer Topical Meeting on Precision Interferometric Metrology* Ashville USA

Gao F, Leach R K, Petzing J and Coupland J M 2008 Surface measurement errors using commercial scanning white light interferometers *Meas. Sci. Technol.* **19** 015303

Gao F, Coupland J and Petzing J 2006 V-groove measurements using white light interferometry *Photon06 (Manchester, 4–7 Sept.)*

Garratt J D 1979 Survey of displacement transducers below 50 mm *J. Phys. E: Sci. Instrum.* **12** 563-573

Garratt J D and Bottomley S C 1990 Technology transfer in the development of a nanotopographic instrument *Nanotechnology* **1** 38-43

Giusca C L and Leach R K 2013a Calibration of the metrological characteristics of Coherence Scanning Interferometers (CSI) and Phase Shifting Interferometers (PSI) *NPL Measurement Good Practice Guide* **GPG 127**

Giusca C L and Leach R K 2013b Calibration of the metrological characteristics of Imaging Confocal Microscopes (ICMs) *NPL Measurement Good Practice Guide* **GPG 128**

Giusca C L and Leach R K 2013c Calibration of the metrological characteristics of Contact Stylus Instruments *NPL Measurement Good Practice Guide* **GPG 129**

Giusca C L and Leach R K 2013d Calibration of the scales of areal surface topography measuring instruments: Part 3-Resolution *Meas. Sci. Technol.* **24** 105010

Giusca C L, Leach R K, Helery F, Gutauskas T 2012a Calibration of the scales of areal surface topography measuring instruments: Part 2- Amplification, linearity and squareness *Meas. Sci. Technol.* **23** 065005

Giusca C L, Leach R K, Helery F, Gutauskas T, Nimishakavi L 2012b Calibration of the scales of areal surface topography measuring instruments: Part 1-Measurement noise and residual flatness *Meas. Sci. Technol.* **23** 035008

Giusca C L, Leach R K, Helery F, Gutauskas T 2011a Calibration of the geometrical characteristics of areal surface topography measuring instruments *J. Phys.: Conf. Ser.* **311** 012005

Giusca C L, Leach R K, Forbes A B 2011b A virtual machine-based uncertainty evaluation for a traceable areal surface texture measuring instrument *Measurement* **44** 988-993

Griffith J E and Grigg D A 1993 Dimensional metrology with scanning probe microscopes *J. Appl. Phys.* **74** R83-R109

Griffiths B 2001 *Surface integiry & functional performance* (Penton Press, London)

de Groot P and Colonna de Lega X 2006 Interpreting interferometric height measurements using the instrument transfer function *Proc. FRINGE 2005*(Berlin: Springer Verlag) 30-37

de Groot P, Colonna de Lega X, Kramer J and Turzhitsky M 2002 Determination of fringe order in white light interference microscopy *Appl. Opt.* **41** 4571-4578 de Groot P and Deck L 1995 Surface profiling by analysis of white-light interferograms in the spatial frequency domain. *J. Mod. Opt*. **42** 389-401

Guttmann M, Jakobs P J, Kaiser K, Vannahme C, Zimmermann L, Schelb M, Matthis B, Straus C, Mappes T, Saile V 2011 Kombinierte Fertigung und inno-vativer Einsatz von mikro- und nanostrukturierten Shim-Formeinsätzen *Galvanotechnik* **102** 394-402

Guttmann M, Kaiser K, Muth S, Moritz H, Schmidt R, Zwanzig M, Hofmann L and Schubert I 2009 Neues modulares Anlagenkonzept für nasschemische Ätzprozesse und die Wafergalvano¬forming *Galvanotechnik* **100** 2616-2624

Haitjema H and Morel M A A 2005 Noise bias removal in profile measurements *Measurement* **38** 21-29

Harasaki A and Wyant J C 2000 Fringe modulation skewing effect in white-light vertical scanning interferometry *Appl. Opt*. **39** 2101-2106

Harasaki A, Schmit J and Wyant J C 2000 Improved vertical-scanning interferometry *Appl. Opt.* **39** 2107–2115

Harasaki A, Schmit J and Wyant J C 2001 Offset of coherent envelope position due to phase change on reflection *Appl. Opt.* **40** 2102–2106

Harris P M, Smith I M, Leach R K, Giusca C, Jiang X and Scott P 2012a Software measurement standards for areal surface texture parameters: part 1—algorithms *Meas. Sci. Technol.* **23** 105008

Harris P M, Smith I M, Wang C, Giusca C and Leach R K 2012b Software measurement standards for areal surface texture parameters: part 2—comparison of software *Meas. Sci. Technol.* **23** 105009

Harrison R E W 1931 A survey of surface quality standards and tolerances based on 1929-1930 precision-grinding practice *Trans. A. S. M. E.* paper no. MSP-53-12

Haycocks J A, Jackson K, Leach R K, Garratt J, MacDonnell I, Rubert P, Lamb J, Wheeler S 2005a Tackling the challenge of traceable surface texture measurement in three dimensions *Proc. 5th Int. euspen Conf, Turin, Italy, May,* 253-256

Haycocks J, Jackson K and Leach R K 2005b Artefacts for performance verification of contacting and non-contacting measuring instruments at the micro and nano scale *NPL Report DEPC-EM (RES) 002*

Hecht E 2003 *Optics* 4th edn (Pearson Education: London)

Hiemenz P C and Rajagopalan R 1997 *Principles of colloid and surface chemistry* 3rd Ed. (Marcel Dekker Inc.: New York)

Hillmann W 1990 Surface profiles obtained by means of optical methods—are they true representations of the real surface *Ann. CIRP* **39** 581–583

Hillmann W, Brand U and Krystek M 1996 Capabilities and limitations of interference microscopy for two and three dimensional surface-measuring technology *Measurement* **19** 95–102

Hughes E B, Oldfield S 2003 Traceable, high accuracy thrust measurement for electric propulsion, *3rd Int. Electric Propulsion Conf., Toulouse, France*

Ismail M F, Yanagi K and Fujii A 2010 An outlier correction procedure and its application to areal surface data measured by optical instruments *Meas. Sci. Technol.* **21** 105105

References

ISO 25178-2: 2012 Geometrical product specifications (GPS) - Surface texture: Areal - Part 2: Terms, definitions and surface texture parameters (International Organization for Standardization)

ISO 25178-3: 2012 Geometrical product specifications (GPS) - Surface texture: Areal - Part 3: Specification operators (International Organization for Standardization)

ISO 25178-601: 2010 Geometrical product specifications (GPS) - Surface texture: Areal - Part 601: Nominal characteristics of contact (stylus) instruments (International Organization for Standardization)

ISO 3274:1997 Geometrical product specification (GPS) – Surface texture: Profile method – Nominal c haracteristics of contact (stylus) instruments (International Organization for Standardization)

ISO4287: 1997 Geometrical product specification (GPS) – Surface texture: Profile method – Terms, definitions and surface texture parameters (International Organization for Standardization)

ISO5436-1: 2000 Geometrical Product Specifications (GPS) - Surface texture: Profile method; Measurement standards - Part 1: Material measures (International Organization for Standardization)

ISO/CD 25178-600: 2012 Geometrical product specifications (GPS) - Surface texture: Areal - Part 600: Nominal characteristics and calibration of areal surface topography instruments (International Organization for Standardization)

ISO/FDIS 11952: 2012 Surface chemical analysis -- Scanning-probe microscopy. Determination of geometric quantities using SPM: Calibration of measuring systems

ISO/FDIS 25178-70: 2012 Geometrical product specification (GPS) – Surface texture: Areal – Part 70: Material measures (International Organization for Standardization)

ISO/FDIS 25178-603: 2012 Geometrical product specifications (GPS) - Surface texture: Areal - Part 603: Nominal characteristics of non-contact (phase shifting interferometric microscopy) instruments (International Organization for Standardization)

ISO/FDIS 25178-604: 2012 Geometrical product specifications (GPS) - Surface texture: Areal - Part 604: Nominal characteristics of non-contact (coherence scanning interferometry) instruments (International Organization for Standardization)

Jiang X, Scott P J, Whitehouse D J and Blunt L 2007a Paradigm shifts in surface metrology. Part I. Historical philosophy *Proc. of R. Soc. A* **467** 2049-2070

Jiang X, Scott P J, Whitehouse D J and Blunt L 2007b Paradigm shifts in surface metrology. Part II. The current shift *Proc. of R. Soc. A* **467** 2071-2099

Jung L, Spranger B, Krüger-Sehm R and Krystek M 2004 Reference software for roughness analysis—features and results *Proc. 11th Int. Colloq. Surfaces, Chemnitz, Germany* 164–170

Karadaglic D 2008 Image formation in conventional brightfield reflection microscopes with optical sectioning property via structured illumination *Micron* **39** 302–310

Kim K J, Jung C S and Hong T E 2007 A new method for the calibartion of the vertical scale of a stylus profilometer using multiple delta-layer films *Meas. Sci. Technol.* **18** 2750-2754

Kino G S and Chim S S C 1990 Mirau correlation microscope *Appl. Opt.* **29** 3775-3783

Koenders L, Dziomba T, Thomsen-Schmidt P and Wilkening G 2005 Standards for the calibration of instruments for dimensional nanometrology *Nanoscale Calibration Standards and Methods: Dimensional and Related Measurements in the Micro- and Nanometer Range* ed G Wilkening and L Koenders (Weinheim: Wiley-VCH) 245-57

Krüger-Sehm R 2010 Private communication *PTB* 14th December, Braunschweig

Krüger-Sehm R, Bakucz P, Jung L and Wilhelms H 2007 Chirp-Kalibriernormale für Oberflächenmessgeräte (Chirp Calibration Standards for Surface Measuring Instru-ments) *Technisches Messen* **74** 572-576

Krüger-Sehm R, Häßler-Grohne W and Frühouf 2004 Traceable calibration standard for the lateral axis of contact stylus instrument *Wear* **257** 1241-1245

Lahousse L, David J, Leleu S, Vailleau G, Ducourtieux S 2005 Application of a new architecture design to a measuring machine with a nanometric resolution *Revue Française de Métrologie* **4** 35-43

Leach R K 2013 *Characterisation of areal surface texture* (Springer: Berlin)

Leach R K 2011 *Optical measurement of surface topography* (Springer: Berlin)

Leach R and Haitjema H 2010 Bandwidth characteristics and comparisons of surface texture measuring instruments *Meas. Sci. Technol.* **21** 079801

Leach R K, Giusca C L, Naoi K 2009 Development an characterisation of a new instrument for the traceable measurement of areal surface texture *Meas. Sci. Technol.* **20** 125102

Leach R K 2009 *Fundamental principles of engineering nanometrology* (Elsevier: Amsterdam)

Leach R K 2007 A new tactile probe based on differential interferometry for use in areal surface texture measurement *Proc. 7th Int. euspen Conf., Bremen, Germany, May* 317-320

Leach R K, Chetwynd D G, Blunt L, Haycocks J, Harris P, Jackson K, Oldfield S and Reilly S 2006 Recent advances in traceble nanoscale dimension and force metrology in the UK *Meas. Sci. Technol.* **17** 467–476

Leach R K 2001The measurement of surface texture using stylus instruments *NPL Measurement Good Practice Guide* **GPG 37**

Leach R K, Garbutt I, Harris P, Cox M G 2001 Production, measurement and analysis of sinusoidal artefacts for calibration of surface texture measuring instruments *NPL Report*

Leach R K 2000 Traceable measurement of surface texture at the National Physical Laboratory using NanoSurf IV *Meas. Sci. Technol.* **11** 1162-1173

Leach R K 1999 Calibration, traceability and uncertainty issues in surface texture metrology *NPL Report* **CLM 7**

Lee B S and Strand T C 1990 Profilometry with a coherence scanning microscope. *Appl. Opt.* **29** 3784-3788

Lee D H and Cho N G 2012 Assessment of surface profile data acquired by a stylus profilometer *Meas. Sci. Technol.* **23** 105601

Lehmann P 2006 Systematic effects in coherence peak and phase evaluation of signals obtained with a vertical scanning white-light Mirau interferometer *Proc. SPIE* **6188** 618811

References

Lehmann P 2003 Optical versus tactile geometry measurement—alternatives or counterparts *Proc. SPIE* **5144** 183–196

Linnik W 1930 Ein Apparat zur Messung von Verchiebungen in der Sehrichtung Z. *Instrum.* **50** 192-

Lipson A, Lipson S G and Lipson H 2011 *Optical physics 4th edd.* (Cambridge University Press)

Mendeleyev V Y 1997 Dependence of measuring errors of rms roughness on stylus tip size for mechanical profilers *Appl. Opt* **36** 9005–9009

Malacara D 1992 *Optical shop testing* (Wiley, New York)

Mandal R, Palodhi K, Coupland J M, Leach R K and Mansfield D 2012 Application of linear systems theory to characterize coherence scanning interferometry *Proc SPIE* **8430** 84300T-1-84300T-10

Masaih E, Greenwood J A, Chetwind D G 2001 *Metrology and properties of engineered surfaces* (Kluwer academic Publishers)

Mainsah E, Sullivan P J, Stout K J 1994 Calibration of translational tables for use in three-dimensional surface topography measurement systems *Int. J. Mach. Tools Manuf.* **34** 211-224

McCool J I 1984 Assessing the effect of stylus tip radius and flight on surface topography measurements *Trans. ASME* **106** 202-209

Minsky M 1988 Memoir on inventing the confocal scanning microscope *Scanning* **10** 128–138

Minsky M 1961 *Microscopy apparatus* US patent 3.013.467

Miroshnikov M M 2010 Academician Vladimir Pavlov Linnik-The founder of modern optical engineering (on the 120th anniversary of his birth) *J. Opt. Technol.* **77** 401-408

Muralikrishnan B, Raja J 2009 *Computational surface and roundness metrology* (Springer: London)

Murphy D B 2001 Fundamentals of light microscopy and electronic engineering (Wiley-liss Inc.: Chichester)

Nayak P R 1971 Random process model of rough surface *Tran. ASME, J. Lubric. Technol.* **39** 398-407

Nemoto K, Yanagi K, Aketagawa M, Yoshida I, Uchidate M, Miyaguchi T, Maruyama H 2009 Development of a roughness measurement standard with irregular surface topography for improving 3D surface texture measurement *Meas. Sci. Technol.* **20** 084023

Neugebauer M and Neuschafer-Rube U 2005 A new micro artefact for testing of optical and tactile sensors *Proc. 5th Int. euspen Conf. , Montpellier, France, May* 201-204

Nicolau P 1939 Quelque recent progress de la microgeometrie des surfaces usinéeset la l’integration pneumatique des rugosités superficielles *Mecanique* **23** 152

Page S F 1948 *Fine surface finish* (Chapman and Hall London, UK: Chapman and Hall)

Palodi K, Coupland J M and Leach R K 2010 A linear model of fringe generation and analysis in coherence scanning interferometry *Proc. ASPE Summer Topical Meeting on Precision interferometric Metrology, Ashville, USA*

Park M-C and Kim S-W 2001 Compensation of phase change on reflection in white-light interferometry for step height measurement *Opt. Lett.* **26** 420–422

Perthen J 1949 *Prufen und messen der oberflachengeatalt* (Carl Hanser Verlag: Munchen, Germany)

Perthen J 1936 Ein neues Verfahren zum Messen der Oberflachengute durch die Kapazitat eines Kondesators *Maschinenbau Betr.* **15** 669

Petley B W 1983 The new definition of the metre *Nature* **303** 373-376

Postek M T, Vladar A E, Keery W, Bishop M, Bunday B and Allgair J 2010 Reference material (RM) 8820: a versatile new NIST standard for nanometrology *Proc SPIE* **76381B** 1-11

Proertner A and Schwider J 2001 Dispersion error in white-light Linnik interferometers and its implications for evaluation procedures *Appl. Opt.* **40** 6223–6228

Raine K W, Downs M J 1978 Beam-splitter coatings for producing phase quadrature interferometer outputs *Optica Acta* **25** 549-558

Reason R E 1967 ASTME Intern. Conf. On Maufacturing Technology, Ann Arbor, Michigen

Reason R E 1961 Report on reference line for roughness and roundness *Ann. CIRP* **11** 95-104

Reason R E *et al.* 1944 *Report on the measurement of surface finish by stylus methods* In Rank Taylor Hobson Leicester, UK:Rank Taylor Hobson

Rhee H, Vorburger T, Lee J and Fu J 2005 Discrepancies between roughness measurements obtained with phase-shifting and white-light interferometry *Appl. Opt.* **44** 5919–5927

Ritter M, Dziomba T, Kranzmann A and Koenders L 2007 A landmark-based 3D calibration strategy for SPM *Meas. Sci. Technol.* **18** 404-414

Sandoz P 1997 Wavelet transform as a processing tool in white-light interferometry *Opt. Let.* **22** 1065-1067

Sandoz P, Devillers R and Plata A 1997 Unambiguous profilometry by fringe-order identification in white-light phase-shifting interferometry *J. Mod. Opt*. **44** 519-534

Saw H 1936 Recent developments in the measurement and control of surface *roughness J. Inst. Prod. Engnrs.* **15** 369-361

Sayles R S and Thomas T R 1977 Measurement of the statistical microgeometry of Engineering surfaces *In Proc. 1st Joint Polytechnic Symp. manufacturing engineering, Leicester. Leicester Polytechnic*

Schanz G, Bade K 2005 Microelectroforming of metals in: Baltes H, Brand O, Fedder G K, Hierold C, Korvonk J G, Tabata O (Eds.) Microengineering of Metals and Ceramics Vol. 4 Wiley-VCH Verlag GmbH and Co. KGaA Weinheim 395-420

Schlesinger, G. 1942 *Surface finish*, report of Research Department of Institute of Production Engineers, London

Schmaltz G 1929 Über Gläte und Ebenheit als physikalisches und physiologiches problem *Zeitschrift des Vereines deutcher Ingenieure* **73** 1461

Schmidt M A and Compton R D 1992 Friction, lubrication and wear technology. In: *ASM handbook* **18** ASM International

References

Schobinger J P 1956 *Investigation onto the production of roughness standards* (PhD theses: Federal Technical College, Zürich)

Schorsch H 1958 *Gutebestummung an technischen oberfiachen, wissenschagtliche* (Verlagsgesellschaft, Stuttgart)

Schwider J, Burow R, Elssner K E, Grzanna J, Spolaczy R and Merkel K 1983 Digital wavefront measuring interferometry: some systematic error sources *Appl. Opt.* **22** 3421–3432

Sharman H B 1967 Calibartion of surface texture instruments *Proc. Instn. Mech. Engnrs.* **182** 319-326

Sheppard C J R and Mao X Q 1988 Confocal microscopes with slit apertures *J. Mod. Opt.* **35** 1169-1185

Smith G T 2002 *Industrial metrology – Surfaces and Roundness* (Springer: London)

Song J F and Vorburger T V 1991 Stylus profiling at high resolution and low force *App. Opt.* **30** 42–50

Song J F 1988 Random profile precision roughness precision specimen *Surface Topography* **1** 303-304

Squire, W. and Trapp 1998 Using complex variables to estimate derivatives of real functions *SIAM Rev* 110-112

Stout K J and Blunt L 2000 *Three- dimensional surface topography – 2nd edition* (Penton Press)

Stout K J, Sullivan P J, Dong W P, Mainsah E, Luo N, Mathia T and Zahyouani H 1993 *The development of methods for the characterization of roughness in three dimensions* 1st edn. (Commission of the European Communities)

Stedman M 1987a Mapping the performance of surface-measuring instruments *Proc. SPIE* **803** 138–142

Stedman M 1987b Basis for comparing the performance of surface-measuring machines *Prec. Eng.* **9** 149–152

Sun Z and Weckenmann A 2010 Reflective property of typical microstructures under a white light interferometer *Meas. Sci. Technol.* **22** 085103

Tanaami T, Otsuki S, Tomosada N, Kosugi Y, Shimizu M and Ishida H 2002 High-speed 1-frame_ms scanning confocal microscope with a microlens and Nipkow disks *Appl. Opt.* **41** 4704-4708

Teague E.C, Scire F.E, Baker S.M, Jensen S.W 1982 Three-dimensional stylus profilometry *Wear* **83**, 1-12

Teague E C 1978 Uncertainties in a stylus type surface texture measuring instrument with an interferometricaly measured step *Metrologia* **14** 39-44

Thomas T R 1999 *Rough surfaces – second edition* (Imperial College Press)

Thomsen-Schmidt P 2011 Characterization of a traceable profiler instrument for areal roughness measurement *Meas. Sci. Technol.* **22** 094019

Thomsen-Schmidt P and Krüger-Sehm R 2008 Calibration of an electromagnetic force compensation system *Proc. XII Int. Colloq. Surf., Chemnitz, Germany, 28-29 Jan.* 323-32

Tian A, Liu X, Chetwynd D G and Cai Zhijian 2007 Stylus contact on short wavelength random surfaces; a simulation study *Meas. Sci. Technol.* **18** 1694-1702

Timms C 1946 Measurement of surface roughness *Metal Treatment* **13** 111-118

Tiziani H, Wegner M and Steudle D 2000 Confocal principle for macro- and microscopic surface and defect analysis *Opt. Eng* **39** 32-39

Tolansky S 1970 Multiple beam interference microscopy of metals (Academic Press Inc., London)

Trumpold H and Frenzel C 2000 Calibration standards for surface topography measuring systems down to nanometric range *EU project SMT4-CT97-2176 Calisurf* **Final Report**

Underwood A 1953 Two recent developments for accuarate measurement of surface texture *Proc. Symp. on Eng. Dim. Metrol. NPL* ***II*** **621**

Van Hasselt R and De Bruin W 1963 Comparative investigation of industrial surface roughness measuring instruments *Ann. CIRP* **11** 193-197

Verveer P J, Hanley Q S, Verbeek P W, Van Vliet L J and Joven T M 1998 Theory of confocal fluorescence imaging in the Programmable Array Microscope (PAM) *J. Microscopy* **189** 192-198

VDI/VDE 2617 Part 6.2 2005 Accuracy of CMMs - Characteristics and their testing - Guideline for the application of DIN EN ISO 10360 to CMMs with optical distance sensors *VDI* Düsseldorf

VDI/VDE 2655 Part 1.1 2008 Optical measurement and microtopographies; calibation of interference microscopes and depth setting standards for roughness measurement, *Beuth-Verlag*

von Weingraber H 1956 Zur definition der Oberflachen raugheit Werk Strattstechnik *Masch, Bass* **46**

von Weingraber H 1942 Pneumatische Mess und Prufgerate *Maschinenbau* **21** 505-510

Walton J 1961 Gramophone record deformation *Wireless World* **7** 353-357

Whitehouse D J 1994 *Handbook of surface metrology* (Institute of Physics, Bristol)

Whitehouse D J 1990 Dynamic aspects of scanning surface instruments and microscopes *Nanotechnology* **1** 93-102

Whitehouse D J 1988 Nano-calibration of stylus-based surface measurement *J. Phys. E: Sci. Instrum.* **21** 46-51

Whitehouse d J 1982 The parameter rush is there a cure *Wear* **83** 75-78

Whitehouse D J and Phillips M J 1982 Two dimensional discrete properties of random surfaces *Phil. Trans. R. Soc. A* **305** 441–468

Whitehouse D J 1979 A theoretical investigation of stylus integration *Ann. CIRP* **23** 181-182

Whitehouse D J 1976 Some theoretical aspects of error separation techniques in surface metrology *J. Phys. E: Sci. Instrum.* **9** 531-536

Wilkening G and Koenders L 2005 *Nanoscale calibration standards and methods* (Wiley-VCH, Chichester)

References

Wilson T and Masters B 1994 Confocal microscopy *App. Opt.* **33** 565-566

Wilson T 1990 *Confocal microscopy* (Academic Press, London)

Wu J J 1999 Spectral analysis for the effect of stylus tip curvature on measuring rough profiles *Wear* **230** 194-200

Wu J J 2000 Spectral analysis for the effect of stylus tip curvature on measuring fractal profiles *Meas. Sci. Technol* **11** 1369-1376

Xiao G Q, Corle T R and Kino G S 1988 Real time confocal scanning optical microscope *Appl. Phys. Lett.* **53** 716-718

Yacoot A and Downs M J 2000 The use of x-ray interferometry to investigate the linearity of the NPL Differential Plane Mirror Optical Interferometer *Meas. Sci. Technol*. **11** 1126-1130

Yacoot A and Koenders L 2008 Aspects of scanning force microscope probes and their effect on dimensional measurement *J. Phys. D: Appl. Phys.* **41** 103001

Yanagi K, Kanda D, Nemoto K, Sakurai T, Yoshida I and Aketagawa M 2007 Development of measurement standard with random surface topography for areal surface texture measuring instruments *Proc. 7th Int. euspen Conf., Bremen, Germany, May* 389-392

Yashchuk V V, McKinney W R and Takacs P Z 2008 Binary pseudorandom grating standard for calibration of surface profilometers *Opt. Eng.* **47** 073602

Yoshida I and Tsukada T 2006 Uncertainty of wavelength limitation due to stylus tip radius or engineering surface texture based on wavelength and amplitude by FFT *Wear* **261** 1225-1231

Zeng W, Jiang X, Scott P J 2010 Fast algorithm of the robust Gaussian regression filter for areal surface analysis *Meas. Sci. Technol.* **21** 055108

Zygo 1993 Integrated interferometer system. Reference manual **OMP-0229B**

Appendix – Aerotech stage angular errors

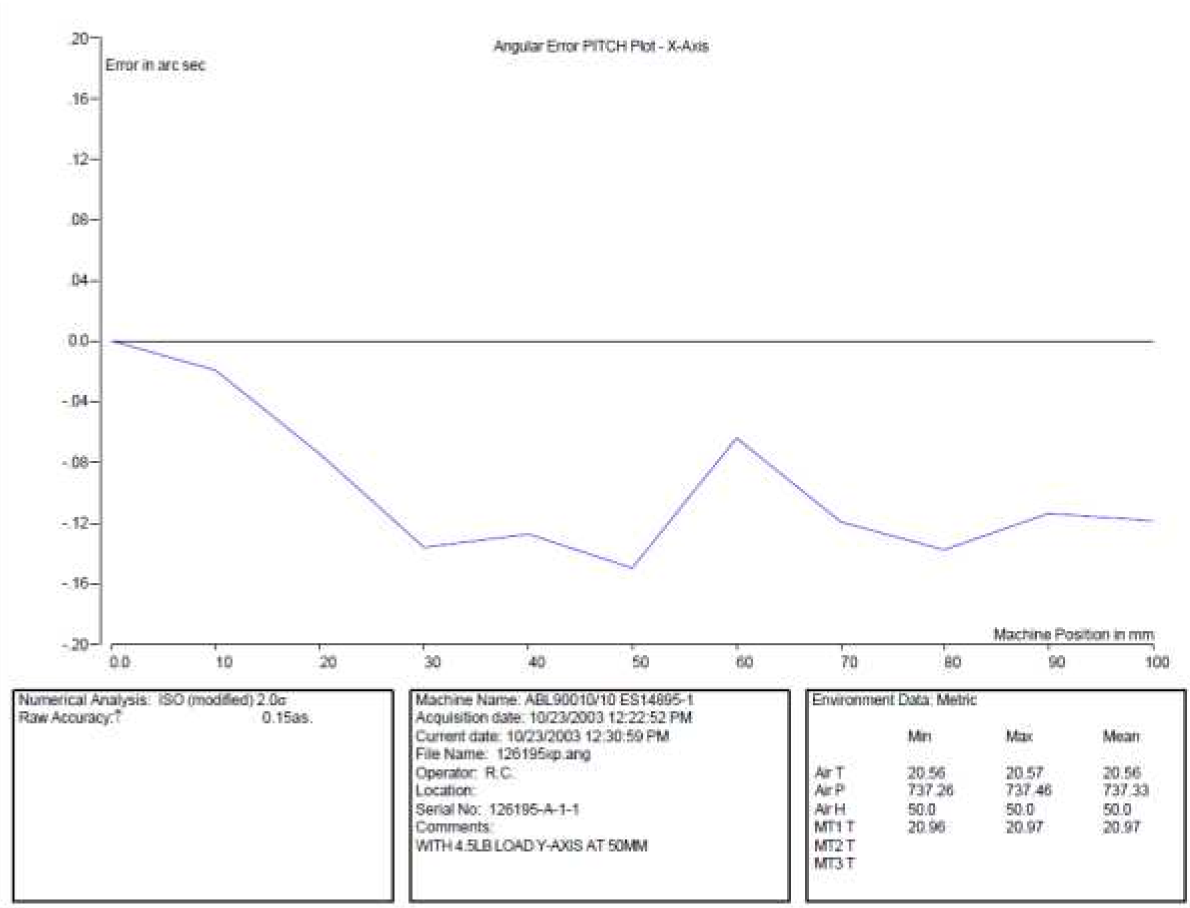

Numerical Analysis: ISO (modified) 2.0σ
Raw Accuracy:† 0.15as.

Machine Name: ABL90010/10 ES14895-1
Acquisition date: 10/23/2003 12:22:52 PM
Current date: 10/23/2003 12:30:59 PM
File Name: 126195xp.ang
Operator: R.C.
Location:
Serial No: 126195-A-1-1
Comments:
WITH 4.5LB LOAD Y-AXIS AT 50MM

Environment Data: Metric

	Min	Max	Mean
Air T	20.56	20.57	20.56
Air P	737.26	737.46	737.33
Air H	50.0	50.0	50.0
MT1 T	20.96	20.97	20.97
MT2 T			
MT3 T			

Figure A.1 *x* axis – pitch

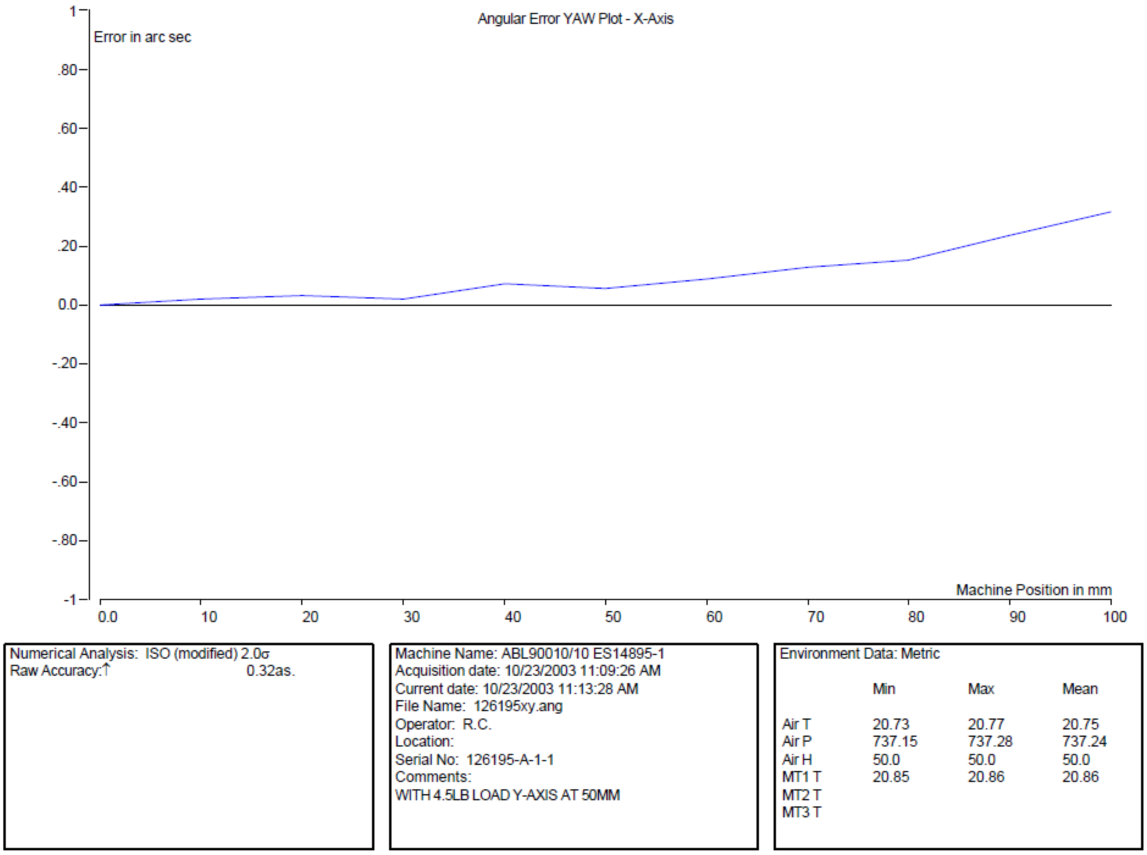

Numerical Analysis: ISO (modified) 2.0σ
Raw Accuracy:↑ 0.32as.

Machine Name: ABL90010/10 ES14895-1
Acquisition date: 10/23/2003 11:09:26 AM
Current date: 10/23/2003 11:13:28 AM
File Name: 126195xy.ang
Operator: R.C.
Location:
Serial No: 126195-A-1-1
Comments:
WITH 4.5LB LOAD Y-AXIS AT 50MM

Environment Data: Metric

	Min	Max	Mean
Air T	20.73	20.77	20.75
Air P	737.15	737.28	737.24
Air H	50.0	50.0	50.0
MT1 T	20.85	20.86	20.86
MT2 T			
MT3 T			

Figure A.2 *x* axis – yaw

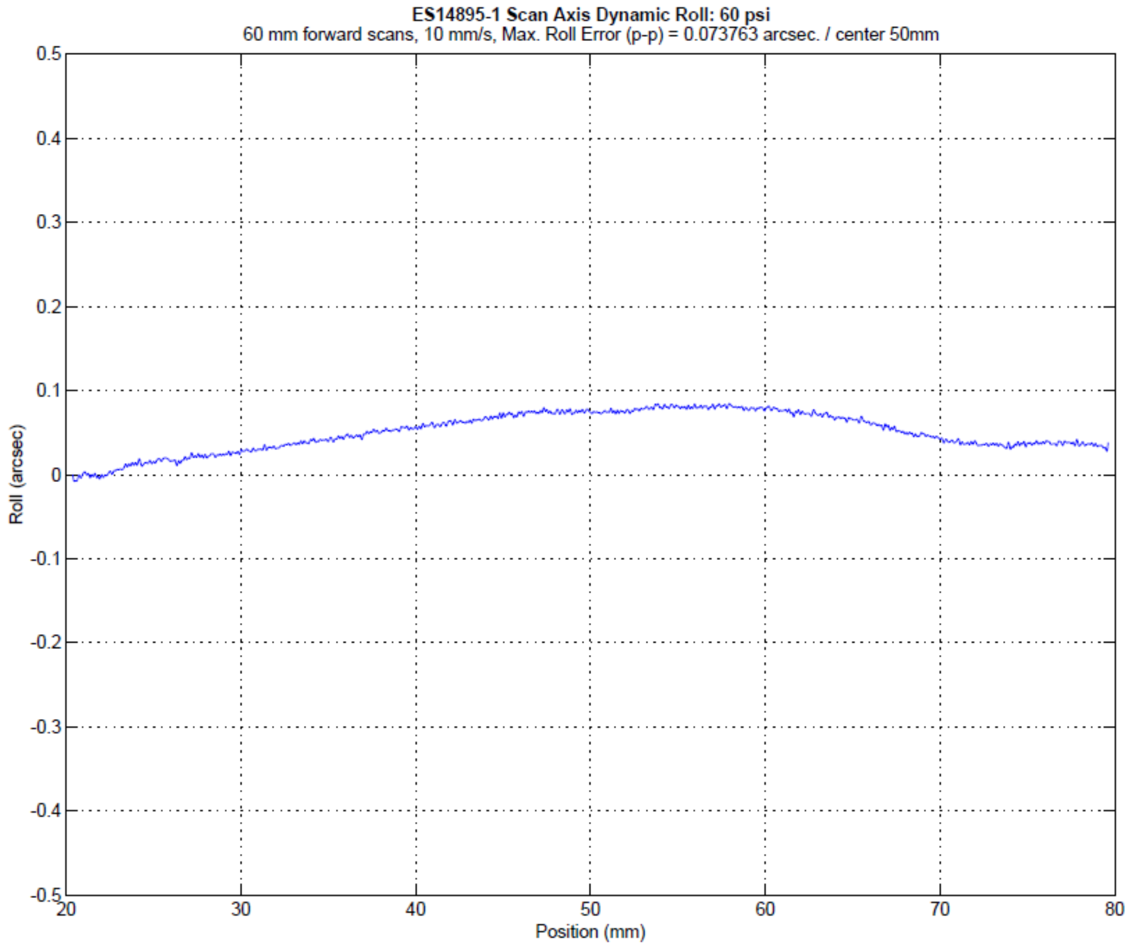

Figure A.3 *x* axis – roll

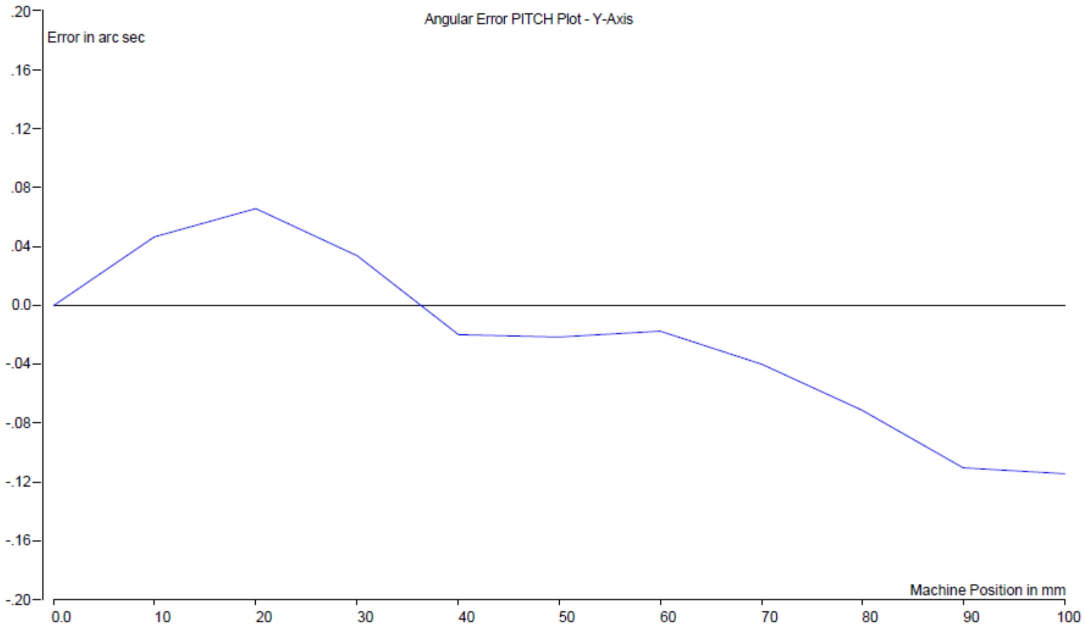

Numerical Analysis: ISO (modified) 2.0σ
Raw Accuracy:↑ 0.18as.

Machine Name: ABL90010/10 ES14895-1
Acquisition date: 10/22/2003 9:41:37 AM
Current date: 10/24/2003 2:51:28 AM
File Name: 126195yp.ang
Operator: R.C.
Location:
Serial No: 126195-A-1-1-X
Comments:
WITH 4.5LB LOAD X-AXIS AT 50MM

Environment Data: Metric

	Min	Max	Mean
Air T	20.39	20.41	20.4
Air P	734.75	734.9	734.8
Air H	50.0	50.0	50.0
MT1 T	21.24	21.26	21.25
MT2 T			
MT3 T			

Figure A.4 *y* axis – pitch

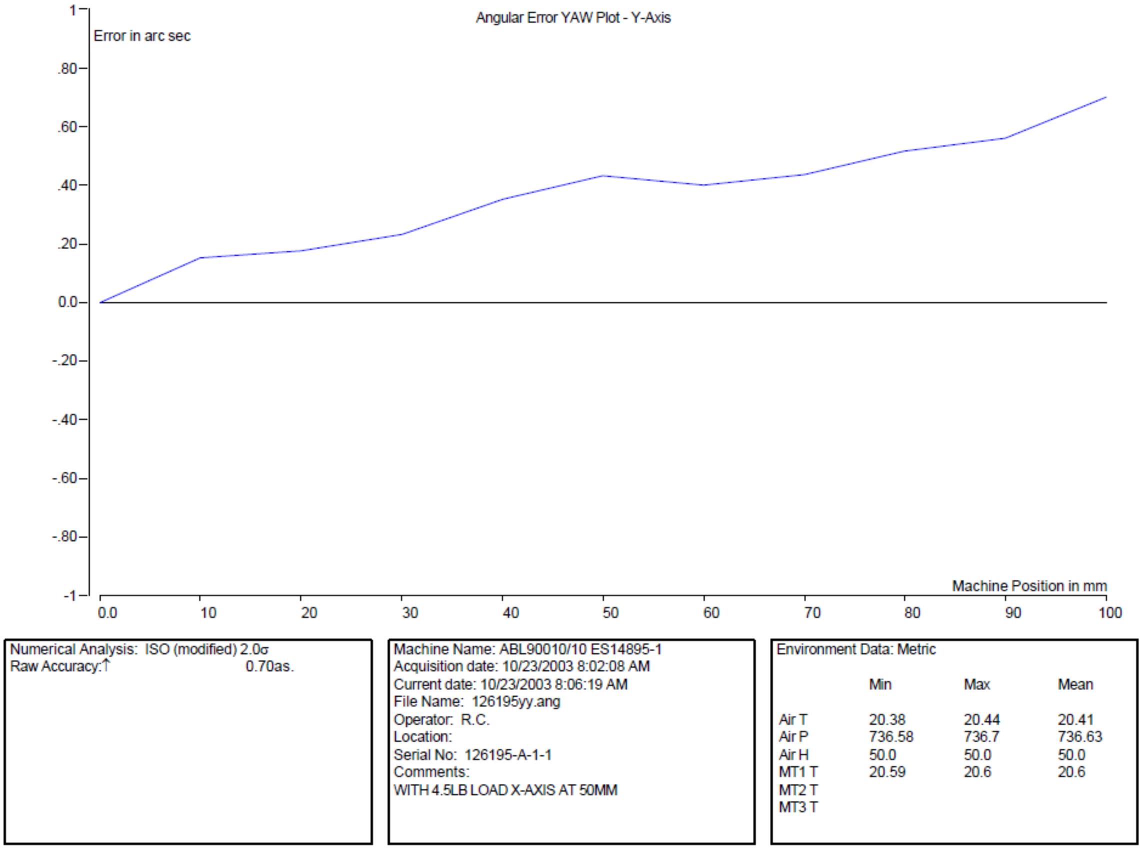

Numerical Analysis: ISO (modified) 2.0σ
Raw Accuracy:↑ 0.70as.

Machine Name: ABL90010/10 ES14895-1
Acquisition date: 10/23/2003 8:02:08 AM
Current date: 10/23/2003 8:06:19 AM
File Name: 126195yy.ang
Operator: R.C.
Location:
Serial No: 126195-A-1-1
Comments:
WITH 4.5LB LOAD X-AXIS AT 50MM

Environment Data: Metric

	Min	Max	Mean
Air T	20.38	20.44	20.41
Air P	736.58	736.7	736.63
Air H	50.0	50.0	50.0
MT1 T	20.59	20.6	20.6
MT2 T			
MT3 T			

Figure A.5 *y* axis – yaw

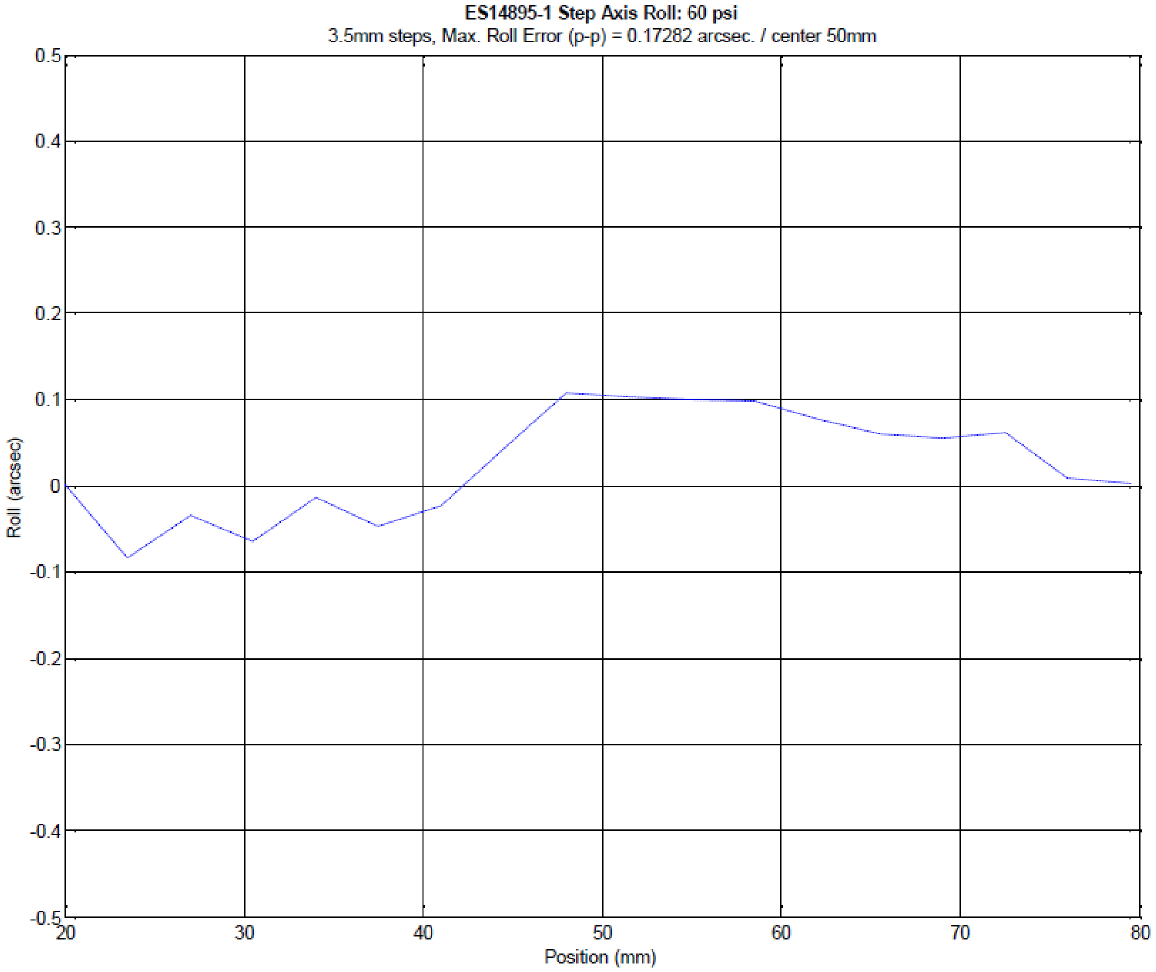

Figure A.6 *y* axis – roll